Z Bosons in LHCb

Dissertation
zur
Erlangung der naturwissenschaftlichen Doktorwürde
(Dr. sc. nat.)
vorgelegt der
Mathematisch – naturwissenschaftlichen Fakultät
der
Universität Zürich

von
Albert Frithjof Bursche
aus
Deutschland

Promotionskomitee
Prof. Dr. Ulrich Straumann (Vorsitz)
Dr. Katharina Müller
Dr. Jonathan Anderson

Zürich, 2014

Preface

This thesis describes the various ways Z bosons are looked at in LHCb. The purpose of this document is twofold. Once it is a documentation of scientific results of which some are unpublished so far and a summary of the LHCb results in this field. On the other hand it is part of the examination procedure in my doctorate studies and thus should document my personal scientific achievements. If you are defining this as results that are entirely my work you may as well stop reading here. There are none! Everything I did in the framework of this thesis relies on data taken by the LHCb experiment and the reconstruction software where countless people have contributed. I made contributions to both by serving first as so called "Data Quality Manager" who has to monitor the data as the come from the detector; as "Shift Leader" running the Data Acquisition System and as "Silicon Tracker Piquet" who has to respond to the shift leaders calls and regularly checks the system. The software contributions were to the jet reconstruction software and to the tools truth matching simulated jets to reconstructed jets.

To structure this schizophrenic document I added apart from the usual in text citations opening sections to each chapter to cover the first aspect while the same time avoiding to quote results that have been super seeded already where possible and state the official LHCb results instead.

If your definition is that the analysis was made entirely by me starting from the files written to the grid by the production team then the results presented in Chapter 5 come close to that. To this analysis Steven Farry contributed the efficiency numbers for muon reconstruction [1]. As well as to the other analyses presented, Katharina Müller provided the theory predictions using MCFM [2] and FEWZ [3].

I made a large contribution to the analysis presented in Chapter 4 but this analysis would not have been possible without the help from Vanya Belyaev and Katharina Müller.

For me it is impossible to tell what I contributed in terms of ideas, code and numbers to the results presented in Chapter 3. This was done in a truly collaborative spirit by many people. The foundations were laid by Victor Coco in a simulation based study in his thesis [4] before LHCb even took data. These studies left a few pieces of jet reconstruction code in the LHCb software for me to pick up and use. I first presented a clear signal of Z plus jet production using jets from tracks and photons and calculated a MC based correction to these jets. Victor Coco developed this further to an approach based on the "Particle Flow" algorithm used in CMS. That uses all information the detector has in the jet i.e. it extends the tracks plus photon jets to jets clustered from charged pions and kaons based on the

best hypothesis from the RICHes; neutral clusters in the HCAL without a pointing track; two prong resonances and photons. On this Murilo Rangel and Oskar Augusto calculated the energy correction. The actual analysis was then performed by William Barter who did the unfolding of the jets and most of the systematic checks. I contributed the track reconstruction efficiencies using a method developed by Michel De Cian [5].

Summary

In this thesis several measurements of the Z boson production cross section in the LHCb detector are presented. After an introduction with the description of the underlying theory; the detector and the properties of the collisions the machine provided to us in LHC run I in Chapter 1, in Chapter 2 the details of the Z reconstruction in the $Z \to \mu^+\mu^-$ final state is discussed. In Chapter 3 jets are added to the Z bosons. Several aspects of jet reconstruction are presented and a cross section measurement for the associated production of Z bosons with jets at $\sqrt{s} = 7\,\text{TeV}$ is presented for two transverse momentum thresholds of the jets. In Chapter 4 the capability of the LHCb detector to reconstruct charmed mesons is used to establish a ZD^0 and a ZD^+ signal and to measure the total cross section. In Chapter 5 the cross section of inclusive Z boson production is measured at a low statistics sample of $3.3\,\text{pb}^{-1}$ at $\sqrt{s} = 2.76\,\text{TeV}$.

Zusammenfassung

In der vorliegenden Dissertation werden mehrere Messungen von Z Boson Produktion im LHCb Detektor beschrieben. Nach einer Einführung über die zugrundeliegende Theorie, den experimentellen Aufbau, und die Eigenschaften der kollidierten Strahlen in Kapitel 1 wird in Kapitel 2 die Rekonstruktion von Z Bosonen im Z $\rightarrow \mu^+\mu^-$ Endzustand erläutert. In Kapitel 3 werden Jets zu einem Z Boson hinzugefügt. Es werden mehrere Aspekte der Jet Rekonstrution besprochen und eine Messung des Wirkungsquerschnittes der assoziierten Produktion von Z Bosonen mit Jets bei $\sqrt{s} = 7\,\text{TeV}$ wird für zwei verschiedene Schwellenwerte im Transversalimpuls angegeben. In Kapitel 4 wird die Fähigkeit des LHCb Detektors Charm Mesonen zu rekonstruieren verwendet um ein Signal von ZD^0 und ZD^+ Produktion zu etablieren und den Wirkungsquerschnitt zu messen. In Kapitel 5 ist eine Messung des inklusiven Wirkungsquerschnittes von Z Boson Produktion in einen kleinen Datensatz von $3.3\,\text{pb}^{-1}$ bei $\sqrt{s} = 2.76\,\text{TeV}$ beschrieben.

Contents

Chapter 1

Introduction

This chapter contains a introduction to the theory, a short description of the detector and a overview over the LHC run I running conditions and datasets available to LHCb.

1.1 The Standard Model of Particle Physics

> The following section follows standard textbooks mainly [6–8]. I don't want to give a complete description but briefly mention what I think are the main foundations of the modern understanding of fundamental physics. I will also introduce a few more exotic models that could potentially contribute to the processes studied in the experimental part of this work.

1.1.1 Particles in the Standard Model

The Standard Model of particle physics has the following particle content: electrically neutral fundamental bosons Z, γ, g and H; charged fundamental bosons $W^{\pm}$ and charged leptons $e^{\pm}$, $\mu^{\pm}$, $\tau^{\pm}$; neutrinos ν_e, ν_μ, ν_τ and quarks u, d, s, c, b and t.

Some of these particles can form asymptotic states that means that they could exist as free particles far away from an interaction if the lifetime was sufficient. These particles are all particles that do not carry a charge from the strong force which are the quarks and the gluon (g). Quarks form hadrons.

The Standard Model completely determines the interactions between these particles. In the following the interactions will be described and I'll try to

also include a motivation why certain choices were made. In the history when the experiments demanded a change in the theory many times not the minimal possible extension was chosen which then lead to predictions left to the experiment to test. The most known nowerdays is the prediction of the Higgs boson in the 1960ties that seems to be observed in 2013.

Fundamental particles in the Standard Model are pointlike. This was tested at LEP where no evidence for a deviation from pointlike electrons was found. The electron radius was found to be smaller than $2.8 \cdot 10^{-19}$m at 95% confidence level [9].

In the following the fundamental particles will be described. Additionally there are bound states that will be described later. Conserved charges in the Standard Model are the electric charge , the weak hypercharge and the colour charge.

Fermions

All fermions in the Standard Model are described in terms of right and left handed Weyl spinors ψ_R and ψ_L that transform under Lorentz Tranformations as the $(1/2, 0)$ and $(0, 1/2)$ representations of the Lorentz group and obey the Weyl equations [7]:

$$i(\partial_0 - \boldsymbol{\sigma} \cdot \boldsymbol{\nabla})\psi_L \tag{1.1}$$

$$i(\partial_0 + \boldsymbol{\sigma} \cdot \boldsymbol{\nabla})\psi_R \tag{1.2}$$

where the four dimensional space time derivative is divided as $\partial_\mu = (\partial_0, \boldsymbol{\nabla})$ and $\boldsymbol{\sigma}$ the three vector of the Pauli matrices.

In the Standard Model most particles occur in both spinor representations while neutrinos exist only in the left handed ψ_L representation.[1]

The leptons in the Standard Model are usually arranged in left handed doublets and right handed singlets that are again ordered in three generations [6].

$$\begin{pmatrix} \nu_{eL} \\ e_L \end{pmatrix}, e_R \qquad \begin{pmatrix} \nu_{\mu L} \\ \mu_L \end{pmatrix}, \mu_R \qquad \begin{pmatrix} \nu_{\tau L} \\ \tau_L \end{pmatrix}, \tau_R \tag{1.3}$$

The left handed doublets carry a weak hypercharge $Y_L^{(\ell)} = -1/2$ while the right handed singlets carry $Y_R^{(\ell)} = 1$ [6]. The other quantum numbers are the

[1] Experimental results suggest that neutrinos have finite mass and thus there must exist inertial frames where the neutrinos are right handed. Neutrinos are massless particles in the Standard Model. I'll stick to that convention for simplicity since this aspect of beyond Standard Model physics is not part of the experimental work presented. Needless to say that a description of the available data needs some sort of extension of the Standard Model to allow for massive neutrinos.

lepton flavour and the lepton number. Both lepton flavour and lepton number are unity for leptons and negative for anti leptons. There is no experimental evidence that the total lepton number might be not conserved despite many searches [10]. The same holds for the individual lepton flavour for e, μ and τ. However for neutrinos the lepton flavour is not conserved in neutrino oscillations. The electric charge of the leptons is zero for neutrino and is -1 times the absolute electron charge for the other leptons. In the following units are used where the charge of the positron is unity. In standard units the positron charge is $q_{\mathrm{e}^+} = 1.602176565 \cdot 10^{-19}\mathrm{C} \pm 3.5 \cdot 10^{-27}\mathrm{C}$ [11].

Like the leptons the quarks are arranged in three families but in left handed doublets and right handed singlets [6].

$$\mathrm{U}_L = \begin{pmatrix} \mathrm{u}_L \\ \mathrm{d}_L \end{pmatrix}, \mathrm{u}_R, \mathrm{d}_R \qquad \mathrm{C}_L = \begin{pmatrix} \mathrm{c}_L \\ \mathrm{s}_L \end{pmatrix}, \mathrm{c}_R, \mathrm{s}_R \qquad \mathrm{T}_L = \begin{pmatrix} \mathrm{t}_L \\ \mathrm{b}_L \end{pmatrix}, \mathrm{t}_R, \mathrm{b}_R \tag{1.4}$$

where the weak hypercharges are:

$$Y_{\mathrm{U}_L} = Y_{\mathrm{C}_L} = Y_{\mathrm{T}_L} = \quad 1/6 \tag{1.5}$$

$$Y_{\mathrm{u}_R} = Y_{\mathrm{c}_R} = Y_{\mathrm{t}_R} = \quad 2/3 \tag{1.6}$$

$$Y_{\mathrm{d}_R} = Y_{\mathrm{s}_R} = Y_{\mathrm{b}_R} = -1/3 \tag{1.7}$$

The u, c and the t quarks are called up type quarks while d, s and the b are down type quarks. Up type quarks carry a electric charge of $Q_q = 2/3$ and down type $Q_q = -1/3$. All quarks carry their flavour (u, d, s, c, b or t) quantum numbers as well as a baryon number of $1/3$. Despite many searches there is no experimental evidence that baryon number is not conserved [10]. The quark flavour is changed in charged current (CC) interactions and in oscillations. All quarks also carry a unit of charge of the strong force. This so called *colour* corresponds to the fundamental representation or **3** representation of $SU(3)$ [7, 8]. Antiquarks carry a unit of charge in the $\bar{\mathbf{3}}$ representation. For both quarks and leptons the weak isospin T_3 is defined as $1/2$ for the upper and $-1/2$ for the lower component of the previously introduced left handed doublets and vanishes for the right handed singlets.

Vector Bosons

Vector bosons occur in the Standard Model always as messenger particle of interactions. The vector bosons of the Standard Model are: g, γ, Z and $\mathrm{W}^{\pm}$. As the name suggests all vector bosons transform as vectors under the Lorentz group. The g carries no electric or weak charge but a charge of the strong force that is related to the adjoined representation **8** of $SU(3)$. This can be illustrated as the gluon carries a colour and an anti-colour that

may not match. It couples to quarks. The γ couples to electrically charged particles and the Z boson couples to fermions that carry a weak isospin (T_3).

The only flavour changing vertex is the vertex involving the $W^{\pm}$ boson. Those couple to pairs of fermions that have a total electric charge of ± 1 with the coupling strength governed by the Cabibbo-Kobayashi-Maskawa matrix V_{CKM}. The $W^{\pm}$ bosons carry electric charge of ± 1 and and have an weak isospin of 1. Additionally to the interactions mentioned so far there are the following trilinear and quadrilinear vertices [6]: $W^+W^-\ \gamma$, W^+W^-Z, $W^+W^-W^+W^-$, W^+W^-ZZ, $W^+W^-Z\ \gamma$, $W^+W^-\ \gamma\ \gamma$. The Standard Model does not contain the vertices $Z\ \gamma\ \gamma$, ZZZ or ZZZZ. The relation between weak isospin, weak hypercharge and electric charge is given by:

$$Q = T_3 + Y \tag{1.8}$$

1.1.2 Interactions

The interactions in the Standard Model are the electromagnetic interaction; the weak interaction that become unified at high energies as electroweak interaction and the strong interaction. It does not describe gravity. It is described as a spontaneously broken Yang Mills theory with the gauge group:

$$U(1)_Y \times SU(2)_L \times SU(3)_{\text{colour}}.$$

To simplify the discussion I start with a slightly different description as gauge theory with massive intermediate vector bosons (IVB). This leads to

The naïve Lagrangian

The Lagrangian can be written in the unitary gauge using the ingredients defined before as [6][2]

$$\begin{aligned}\mathcal{L}_{\text{int}} = &\sum_f Q_f \bar{f}\gamma^\mu f A^\mu + \mathcal{L}_{\text{CC}} + \mathcal{L}_{\text{NC}} + \mathcal{L}_{\text{mass}} + \mathcal{L}_{\text{ferm}} + \mathcal{L}_{\text{QCD}} \\ &- ig(\mathrm{W}^0_\mu \mathrm{W}^-_\nu \overleftrightarrow{\partial^\mu} \mathrm{W}^{+\nu} + \mathrm{W}^-_\mu \mathrm{W}^+_\nu \overleftrightarrow{\partial^\mu} \mathrm{W}^{0\nu} + \mathrm{W}^+_\mu \mathrm{W}^0_\nu \overleftrightarrow{\partial^\mu} \mathrm{W}^{0\nu}) \\ &- ig^2(\frac{1}{2}(\mathrm{W}^- \cdot \mathrm{W}^+)^2) - \frac{1}{2}(\mathrm{W}^-)^2(\mathrm{W}^+)^2 \\ &\quad + (\mathrm{W}^0)^2(\mathrm{W}^- \cdot \mathrm{W}^+) - (\mathrm{W}^-\mathrm{W}^0)(\mathrm{W}^+\mathrm{W}^0))\end{aligned} \tag{1.9}$$

[2] with respect to Eqn. 7.242 in [6] the Higgs related terms are written as explicit mass terms or omitted. The electroweak symmetry breaking is explained later in this section.

with $f \overleftrightarrow{\partial} g = f(\partial g) - (\partial f)g$ and $\mathrm{W}^0_\mu = \cos(\theta_W)\mathrm{Z}_\mu + \sin(\theta_W)\mathrm{A}_\mu$. Here A_μ denotes the photon field. The Lagrangian for the neutral current(NC) is given by [6]:

$$\mathcal{L}_{\mathrm{NC}} = \frac{g}{\cos(\theta_W)} \sum (\varepsilon_L^{(f)} \bar{f}_L \gamma^\lambda f_L + \varepsilon_R^{(f)} \bar{f}_R \gamma^\lambda f_R) \mathrm{Z}_\lambda \tag{1.10}$$

with

$$\varepsilon_L^{(f)} = T_{3L}^{(f)} - Q_f \sin^2(\theta_W) \tag{1.11}$$

$$\varepsilon_R^{(f)} = T_{3R}^{(f)} - Q_f \sin^2(\theta_W). \tag{1.12}$$

The charged current (CC) Lagrangian is given by:

$$\begin{aligned} \mathcal{L}_{\mathrm{CC}} = {} & \frac{g}{2\sqrt{2}} \sum_{\ell \in \mathrm{e},\mu,\tau} \overline{\nu}_\ell \gamma^\lambda (1-\gamma_5) \ell \mathrm{W}^+_\lambda \\ & + \frac{g}{2\sqrt{2}} \begin{pmatrix} \bar{\mathrm{u}} & \bar{\mathrm{c}} & \bar{\mathrm{t}} \end{pmatrix} \gamma^\lambda (1-\gamma_5) V_{\mathrm{CKM}} \begin{pmatrix} \mathrm{d} \\ \mathrm{s} \\ \mathrm{b} \end{pmatrix} \mathrm{W}^+_\lambda + \mathrm{h.c.} \end{aligned} \tag{1.13}$$

For the beginning of the discussion the vector boson mass term is just accounted for by an explicit mass term:

$$\mathcal{L}_{\mathrm{mass}} = m_{\mathrm{W}^\pm} \mathrm{W}^-_\mu \mathrm{W}^{+\mu} + \frac{1}{2} m_{\mathrm{Z}} \mathrm{Z}_\mu \mathrm{Z}^\mu \tag{1.14}$$

for the massive bosons and

$$\mathcal{L}_{\mathrm{ferm}} = \bar{\psi}(\partial_\mu \gamma^\mu - m)\psi \tag{1.15}$$

for the fermions. The strong interaction is described by:

$$\mathcal{L}_{\mathrm{QCD}} = -\frac{1}{4} F^a_{\mu\nu} F^{a\mu\nu} \tag{1.16}$$

with the field strength defined as

$$F^a_{\mu\nu} = \partial_\mu A^a_\nu - \partial_\nu A^a_\mu + g f^{abc} A^b_\mu A^c_\nu \tag{1.17}$$

This formulation of the standard model allows to describe all observed interactions until 2013. Nevertheless it has fundamental flaws that lead to electroweak unification. One obstacle that has to be overcome in order to actually do the unification are explicit mass terms like Equation 1.14 which break the electroweak symmetry. This is explained in the next section.

The Glashow-Weinberg-Salam Theory

The electroweak sector of the Standard Model is obtained when an $U(1) \times SU(2)$ local gauge symmetry is required from the Lagrangian. For now this is done with massless gauge bosons since terms like Equation 1.14 would break the symmetry. These terms have to be recovered later in order to describe the available observables.

Requiring invariance under $U(1) \times SU(2)$ means any observable must be invariant under the transformation [6]:

$$\psi'(x) = e^{-i\omega(x)}\psi \tag{1.18}$$

for $U(1)$ and

$$\psi'(x) = e^{-i\omega^a(x)}T^a\psi \tag{1.19}$$

for $SU(2)$ with $\omega^{(a)}(x)$ being an arbitrary function of spacetime and T^a the generators of the $SU(2)$ group. This leads to the following transformation properties of the gauge fields [6]:

$$A'^a_\mu = A^a_\mu - f^{abc}\epsilon^b A^c_\mu + \frac{1}{g}\partial_\mu \epsilon^a \tag{1.20}$$

The structure constants f^{abc} vanish in case of $U(1)$ since $U(1)$ is abelian. In order to make the kinetic term of the gauge field

$$-\frac{1}{4}F^a_{\mu\nu}F^{\mu\nu a} \tag{1.21}$$

gauge invariant the gauge field strength tensor acquires an additional term and reads as [6]:

$$F^a_{\mu\nu} = \partial_\mu A^a_\nu - \partial_\nu A^a_\mu - + g f^{abc} A^b_\mu A^c_\nu \tag{1.22}$$

The structure of the covariant derivative in Equation is also governed by the gauge symmetry. The Lagrangian of the gauge field then becomes [6]:

$$\begin{aligned}\mathcal{L}_{\text{gauge}} = -\frac{1}{4}F^a_{\mu\nu}F^{\mu\nu a} = &-\frac{1}{4}A^a_{\mu\nu}A^{\mu\nu a} - \frac{1}{2}g f^{abc}(\partial_\mu A^a_\nu - \partial_\nu A^a_\mu)A^{b\mu}A^{c\nu} \\ &- \frac{1}{4}g^2 f^{abc} f^{ajk} A^a_\mu A^c_\nu A^{j\mu} A^{k\nu}\end{aligned} \tag{1.23}$$

where $A^a_{\mu\nu}$ denotes the field strength of the free field

$$A^a_{\mu\nu} = \partial_\mu A^a_\nu - \partial_\nu A^a_\mu \tag{1.24}$$

It can be seen from Equation 1.23 that the derivation of the interaction from the gauge condition strongly constrains the allowed couplings in the theory. These couplings have been measured in good agreement with the predictions [12] at LEP. There are no mass terms, as these will break the symmetry of the Lagrangian. Since this does not correspond to what is seen in nature, an additional particle needs to be introduced. This is explained in the following sections.

Symmetries and the Goldstone Boson

The degrees of freedom differ for massless and massive gauge bosons. Only massive gauge bosons can be longitudinally polarised. This degree of freedom has to be added to the lagrangian in order to describe massive gauge bosons. It is taken from the so called Goldstone boson. In order to understand what a Goldstone boson is and where this degree of freedom can be taken from, a Lagrangian of this type is considered [6]:

$$\mathcal{L} = \partial_\mu \varphi \partial^\mu \varphi^* + \mu^2 \varphi \varphi^* - \lambda(\varphi \varphi^*)^2. \tag{1.25}$$

Here ϕ is complex scalar field; μ is a parameter with the dimension of mass and λ a dimensionless parameter. With the following substitutions

$$\rho^2 = \varphi \varphi^* \tag{1.26}$$

$$v = \frac{\mu}{\sqrt{\lambda}} = \sqrt{\frac{-\mu^2}{\lambda}} \tag{1.27}$$

$$\rho = \frac{1}{\sqrt{2}}(\sigma + v) \tag{1.28}$$

$$\varphi = \rho e^{i\frac{\pi}{v}} \tag{1.29}$$

this Lagrangian is equivalent to [6]:

$$\mathcal{L} = \frac{1}{2}\partial_\mu \sigma \partial^\mu \sigma + \frac{1}{2}\partial_\mu \pi \partial^\mu \pi - \frac{1}{4}(\sigma^2 + 2v\sigma)^2 + \frac{1}{2v^2}\sigma^2 \partial_\mu \pi \partial^\mu \pi + \frac{1}{v}\sigma \partial_\mu \pi \partial^\mu \pi \tag{1.30}$$

This expression has important implications. Instead of a complex scalar field in a potential it now describes two real fields. A massless field π and a field σ that has a term $-\lambda v^2 \sigma^2$ that can be interpreted as a mass term. If one allows a new field to interact with ρ that field will also acquire mass terms proportional to the coupling strength. The field π is called the Goldstone Boson. Together with the massless Goldstone boson another massive particle σ appears in the theory. This is called the Higgs boson.

The Englert-Brout-Higgs Formalism

In order to generate mass terms for three gauge bosons three longitudinal degrees of freedom have to be added to the theory. This is done by using a doublet instead of a singlet [6] of complex scalars φ^+ and φ^0:

$$\Phi = \begin{pmatrix} \varphi^+ \\ \varphi^0 \end{pmatrix} = \begin{pmatrix} \varphi_1 + i\varphi_2 \\ \varphi_3 + i\varphi_4 \end{pmatrix} \tag{1.31}$$

Analogically the following is added to the Lagrangian [6]:

$$\mathcal{L}_{\text{Goldstone}} = (\partial_\mu \Phi^\dagger)(\partial^\mu \Phi) - V(\Phi) \tag{1.32}$$

This term is symmetric under $O(4)$ which includes $SU(2) \times U(1)$ [6] which means it does not break the gauge symmetry. Then the covariant derivative is applied instead of the normal partial derivative:

$$D_\mu = \partial_\mu - igA^a_\mu \frac{\tau^a}{2} - ig'YB_\mu \tag{1.33}$$

where τ^a represent the Pauli matrices. Using the gauge symmetry and a series of substitutions the $SU(2) \times U(1)$ Yang-Mills Lagrangian with this extra term can be rewritten as [6]:

$$\begin{aligned} \mathcal{L}_{\text{Higgs}} =& \Phi^\dagger \left(\overleftarrow{\partial}_\mu + ig\mathrm{A}_\mu{}^a \frac{\tau^a}{2} + ig'Y\mathrm{B}_\mu \right) \\ & \left(\overrightarrow{\partial}^\mu - ig\mathrm{A}^{\mu a} \frac{\tau^a}{2} - ig'Y\mathrm{B}^\mu \right) \Phi \\ & - \lambda \left(\Phi^\dagger \Phi - \frac{v^2}{2} \right)^2 \end{aligned} \tag{1.34}$$

This is current written in terms of pure gauge fields A^a_μ and B_μ. From these fields the fields corresponding to the observed particles are obtained with another substitution: the weak mixing. All physical states have to be eigenstates of the electric charge. The $\mathrm{W}^\pm$ are as the name suggests eigenstates to the eigenvalue ± 1. Z and γ are a combination of the eigenstates to the eigenvalue zero and therefore can be combined from A and B fields by a rotation around the weak mixing angle θ_W:

$$\mathrm{W}^\pm{}_\mu = (\mathrm{A}^1_\mu \pm \mathrm{A}^2_\mu) \tag{1.35}$$

$$\mathrm{Z}_\mu = \cos\theta_W \mathrm{A}^3_\mu - \sin\theta_W \mathrm{B}_\mu \tag{1.36}$$

$$\mathrm{A}_\mu = \sin\theta_W \mathrm{A}^3_\mu + \cos\theta_W \mathrm{B}_\mu \tag{1.37}$$

The weak mixing angle was measured as [13]:

$$\sin^2(\theta_W)(m_{\mathrm{Z}})(\overline{\mathrm{MS}}) = 0.23126(5) \tag{1.38}$$

If the doublet is expressed in the so called U–gauge parts of the Lagrangian reads [6]:

$$\begin{aligned}\mathcal{L}^{(U)}_{\mathrm{Higgs}} &= \frac{1}{2}\partial_\mu H \partial^\mu H - \lambda v^2 H^2 - \lambda v H^3 - \frac{1}{4}\lambda H^4 \\ &+ \frac{1}{8}(v+H)^2(2g^2 \mathrm{W}^-_\mu \mathrm{W}^{+\mu} + (g^2+g'^2) Z_\mu \mathrm{Z}^\mu)\end{aligned} \tag{1.39}$$

This way the A^a_μ is a $SU(2)$ gauge field acquires mass from the Higgs mechanism and B_μ the field corresponding to the $U(1)$ symmetry remains massless. Consequently also with mass terms for the $\mathrm{W}^\pm$ and Z bosons. However there is also a mass term for the boson H, called the Higgs boson.

So far these construction seems ad-hoc but the model predicted the following properties of the particles and coupling constants [6] which where found in agreement with the measurements [10]:

$$\frac{m_{\mathrm{W}^\pm}}{m_{\mathrm{Z}}} = \cos\theta_W = \sqrt{1 - \frac{e^2}{g^2}} \tag{1.40}$$

$$v = \left(G_F\sqrt{2}\right)^{-1} \tag{1.41}$$

v is called the Higgs vacuum expectation value and θ_W the weak mixing angle. Equation 1.40 was found to hold when $\mathrm{W}^\pm$ [14,15] and Z [16,17] were discovered in UA1 [14,16] and UA2 [15,17] in 1983.

The boson with mass around 125 GeV discovered in 2013 by Atlas [18] and CMS [19] is currently expected to be the field H in Equation 1.39. The model predicted the coupling constants to all known Standard Model particles. The effort to test these predictions has just started at the large experiments at LHC and is foreseen at future colliders. It already strongly influences the energy and technology choices for these projects.

Quantum Chromodynamics

QCD is an additional set of interactions that affects quarks and gluons. It is a massless $SU(3)$ gauge theory that occurs in two representations. This is called $SU(3)_{\mathrm{Colour}}$. The fundamental representation **3** for quarks, $\bar{\mathbf{3}}$ for antiquarks and the adjoined representation **8** for gluons. All other particles are singlets with respect to $SU(3)_{\mathrm{Colour}}$. Mathematical complications in the calculations give rise to the need of another concept called renormalisation.

This leads to a scale dependence of the coupling constants. In the case of QCD the renormalised coupling constant at a scale Q assumes the following form [7]: [3]

$$\alpha_s(Q) = \frac{2\pi}{b_0 \log(Q/\Lambda_{\mathrm{QCD}})} \tag{1.42}$$

With $\Lambda_{\mathrm{QCD}} \approx 200\,\mathrm{MeV}$ and $b_0 = 11 - \frac{2}{3}n_f$. The number of quark flavours n_f is six. This makes b_0 positive and leads to a pole on the coupling constant around Λ_{QCD}. That pole is the reason why this interaction is called the strong force. This low energy regime is usually referred to as the non-pertubative regime. At high scales the coupling constant becomes small and thus matrix elements can be calculated using the usual formalism. This is referred to as pertubative QCD (pQCD).

Confinement

Being mediated by a massless field the strong force is in principle a long range force. As outlined before the coupling becomes strong a low energies. If there is a pair produced $\mathrm{q\bar{q}}$ flying apart at the length scale of about a femtometer the energy in the gluon field becomes sufficient to generate another $\mathrm{q'\bar{q}'}$ pair. Then the lowest energy state is when $\mathrm{q\bar{q}'}$ and $\mathrm{q'\bar{q}}$ form two colour neutral states that keep flying apart. Colour neutral states consisting of quarks and gluons are called hadrons. This process occurs in the non-pertubative regime where α_s is strong and is called hadronisation. It is not as simple as described before and leads to more hadrons produced from a $\mathrm{q\bar{q}}$ pair due the large amounts of soft emissions. This behaviour is approximated in the so called parton shower models as implemented in e.g. PYTHIA [22] and leads to the confinement of QCD. That means, even though the gluon is massless a classical colour field can not exist because no isolated colour charge can exist largely separated from other colour charges. Neither quark nor gluons can be directly observed in a detector i.e. they do not form asymptotic states. Asymptotic states are always colour neutral. The production of a quarks or a gluon in a hard scatter can manifest itself in a hadronic jet which is measurable. This jet carries information of the initial quark flavour.

Baryonic Matter

There are many possible configurations which are a singlet under $SU(3)_{\mathrm{Colour}}$. The simplest possibilities are bound states of a quark and an antiquark ($\mathrm{q\bar{q}'}$)

[3] This is given in the so called $\overline{\mathrm{MS}}$ renormalisation scheme. For the original work see [20, 21].

which are called mesons. The name *colour* for the charge originates from another property. A state of three quarks is colour neutral if all the colours are different just as a red, a green and a blue light beam together, are perceived by the human eye as white light. That state is called a baryon. A great multitude of mesons and baryons has been observed. Since each quark carries a baryon number of 1/3 each baryon has a baryon number of unity. This is a conserved quantum number and renders the lightest baryon – the proton – stable. The lightest two baryons the proton and the neutron form bound states called nuclei. Well established forms of hadrons are mesons and baryons of light, c and b quarks. There are a multitude of well established mesons and baryons [10] as well as states whose existence is expected but not confirmed so far. New states are still being discovered like recently the exited Λ_b^0 states $\Lambda_b^{0*}(5912)$ and $\Lambda_b^{0*}(5920)$ [23] by LHCb.

Exotic Hadrons

Other states that can be colour neutral are tetraquarks ($qq\bar{q}\bar{q}$) pentaquarks ($qqqq\bar{q}$) and mesonic atoms ($q\bar{q}$)($q\bar{q}$) analogously to nuclei formed from baryons. These state where not observed in nature even though there are hadrons that have properties as they would be expected from such states. The LHCb physics programme also includes measurements of exotic hadrons like X(3872) [24–26] and $Z(4430)^-$ [27] and a search for X(4140) and X(4274) [28] claimed by CDF [29] in decays of B mesons and direct inclusive and exclusive production.

In this work the results of a measurement are qualitatively confronted with the hypothesis that the proton contains a part of a pentaquark wavefunction $|uudc\bar{c}>$ [30] without finding any evidence supporting that hypothesis.

A state of several gluons a so called glueball may be colour neutral as well. Among others the hadron $f_0(600)$ (or σ) is analysed in order to test the hypothesis of it being a glueball [10].

The top quark

The top quark has special properties in the Standard Model. It is the heaviest fundamental particle in the Standard Model. It is also heavier that $W^{\pm}$ and beauty quark and thus the decay $t \rightarrow W^+b$ is not suppressed. This leads to a very low lifetime of the top and thus it is currently unknown whether t quarks bind into hadrons. If a $t\bar{t}$ bound state usually referred to as toponium exists it is expected to be undetectable at the LHC [31]. A measurement of the $t\bar{t}$ close to the the production threshold at a lepton collider may shed

light on this matter. This is outside of the reach of present and past lepton colliders.

Flavour Changing Neutral Current

In the Standard Model all transitions between different quark flavours are mediated by $W^{\pm}$ bosons that carry electric charge. This forbids decays of quarks into quarks of the same charge at tree level. Such flavour changing neutral current (FCNC) decays are nevertheless possible in the so called box diagrams and also in electroweak penguin diagrams. In numerous LHCb publications the FCNC decays of b-hadrons via off shell intermediate states are studied and compared to the Standard Model predictions [32].

The decay t $\rightarrow$cZ is strongly suppressed in the Standard Model with a predicted branching fraction in the $10^{-14} - 10^{-13}$ regime [33] but can be strongly enhanced by several new physics models. As discussed in Chapter 4 no evidence for a t decay was found in the ZD^0 or the ZD^+ invariant mass. Due to the selection criteria also no sensitivity is expected.

1.1.3 Interactions of Hadrons

QCD Factorisation

Theory calculations within the Standard Model are done in terms of fundamental particles. LHC is colliding protons which are baryons and thus not fundamental particles. It can be shown that the cross sections for the production of a state S are calculated initially as cross sections of quarks and gluons ($\hat{\sigma}$) can be converted to cross sections in terms of colliding protons (σ) in the following way [34].

$$\frac{\mathrm{d}\,\sigma}{\mathrm{d}\,Q^2\,\mathrm{d}\,y} = \sum_{ab} \int_{x_A} \mathrm{d}\,\xi_A \int_{x_B} \mathrm{d}\,\xi_B f_{a/A}(\xi_A,\mu)\hat{\sigma}_{ab} f_{b/B}(\xi_B,\mu) \tag{1.43}$$

Here the indices a, b denote the particle species that is considered i.e. a certain quark or a gluon; A, B denote the hadron species that is collided and $f_{a/A}(\xi_A, \mu)$ is the parton distribution function (PDF) that is the distribution of the parton a in the hadron A carrying the momentum fraction ξ_a that is evaluated at the factorisation scale μ. The factorisation theorem holds up to power law corrections in the energy Q [34]. This yields a sound description of processes where the main production is of the form:

$$\sum_{ab} ab \rightarrow S + X \tag{1.44}$$

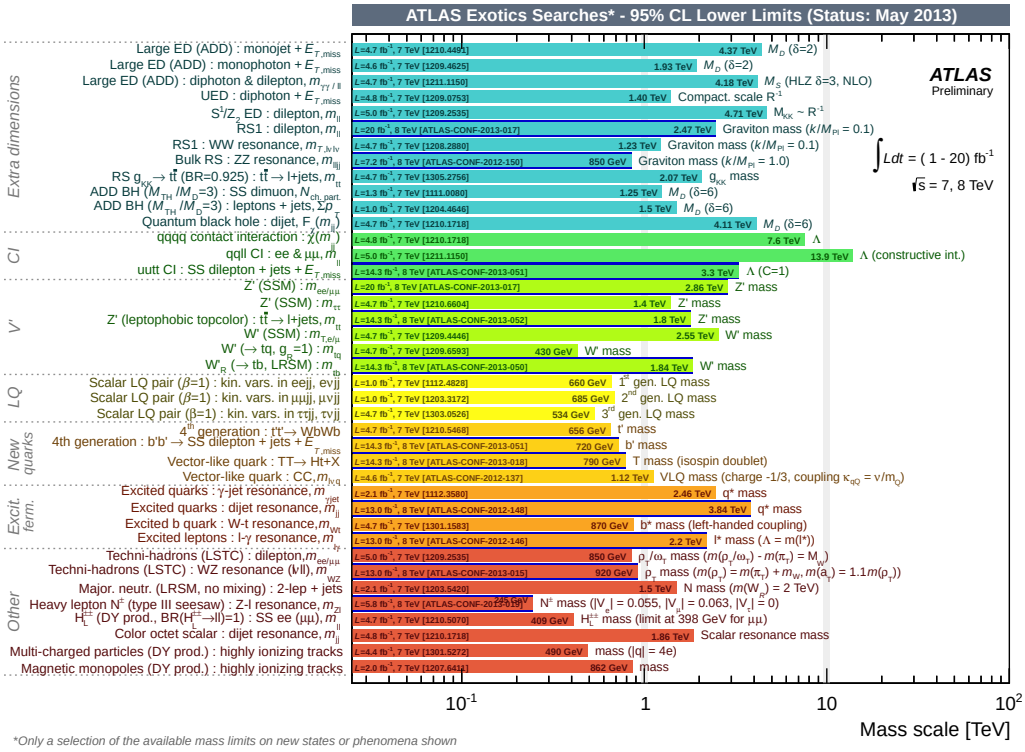

Figure 1.1: Limits from the new physics searches from Atlas. The plot is from their public website. The actual references are on the plot.

The additional final state particles from the remainder of the hadrons are summarised in X which is not expected to be equal in each event. Most of the predictions for Standard Model processes at the LHC that lead to the impressive lists of exclusion limits for many kinds of new physics are based on that. A collection of results is shown in Figure 1.1.

Double Parton Scattering

In processes where more than one parton from each interacting hadron is involved a generalised ansatz was proposed [35, 36]. In the following the meaning of A, B is changed to $S = A + B$. Additionally instead of computing the n-point function with four partons in the initial state factorisation between the hard processes A and B is assumed. This leads to the following

description [35, 36] in the notation of [37] [4] :

$$\begin{aligned}\sigma_{A,B}^{\mathrm{DPS}} =& \frac{m}{2}\sum_{i,j,k,l}\int \mathrm{d}\,\xi_1\,\mathrm{d}\,\xi_2\,\mathrm{d}\,\xi_1'\,\mathrm{d}\,\xi_2'\,\mathrm{d}^2\,b \\ &\times\Gamma_{i,j}(\xi_1,\xi_2,b,t_1,t_2)\Gamma_{k,l}(\xi_1',\xi_2',b,t_1,t_2) \\ &\times\hat{\sigma}_{ik}^{A}(\xi_1,\xi_1')\hat{\sigma}_{jl}^{B}(\xi_2,\xi_2') \end{aligned} \tag{1.45}$$

where

$$m = \begin{cases} 2 & A = B \\ 1 & A \neq B \end{cases} \tag{1.46}$$

is a combinatorial factor. Under the assumption that the generalised double parton distribution function $\Gamma_{i,j}(\xi_1,\xi_2,b,t_1,t_2)$ can be decomposed in

$$\Gamma_{i,j}(\xi_1,\xi_2,b,t_1,t_2) = D_h^{ij}(\xi_1,\xi_2,t_1,t_2)F_j^i(b) \tag{1.47}$$

Equation 1.45 can be simplified to [37]:

$$\begin{aligned}\sigma_{A,B}^{\mathrm{DPS}} =& \frac{m}{2\sigma_{\mathrm{eff}}}\sum_{i,j,k,l}\int \mathrm{d}\,\xi_1\,\mathrm{d}\,\xi_2\,\mathrm{d}\,\xi_1'\,\mathrm{d}\,\xi_2' \\ &\times D_p^{i,j}(\xi_1,\xi_2,t_1,t_2)D_p^{k,l}(\xi_1',\xi_2',t_1,t_2) \\ &\times\hat{\sigma}_{ik}^{A}(\xi_1,\xi_1')\hat{\sigma}_{jl}^{B}(\xi_2,\xi_2') \end{aligned} \tag{1.48}$$

with the effective cross section

$$\sigma_{\mathrm{eff}} = \left(\int \mathrm{d}^2\,bF(b)\right)^{-1} \tag{1.49}$$

This formula is further simplified by the additional approximation that the double parton distribution functions factorise as

$$D_h^{ij}(\xi_1,\xi_2,t_1,t_2) = D_h^i(\xi_1,t_1)D_h^j(\xi_2,t_2). \tag{1.50}$$

This approximation has been criticised in [38]. It was shown that even if 1.50 holds at a given scale the evolution using the renormalisation group equations will break it at a different scale.[5] This leads to the following simple formula:

$$\sigma_{AB} = \frac{m}{2}\frac{\sigma_A\sigma_B}{\sigma_{\mathrm{eff}}}. \tag{1.51}$$

[4] The notation for the momentum fraction of the parton remains ξ as in [34] unlike [37].

[5] [38] contains this statement for a slightly different variant of 1.50 that has a factor to cut off the energy nonconserving phase space from 1.50.

This formula implies that the scatters are independent from each other and is not justified if the flavour of the partons or the momentum fraction make a difference in the processes studied. This approximation violates energy conservation.

Nevertheless this description is phenomenologically successful [39] and leads to an energy independent result for σ_{eff}. The LHCb measurements of double charm production [40] yields higher values [41] compared to the value observed at Tevatron.

Since there is no explicit dependence on the PDFs the naïve double parton scattering (DPS) formula 1.51 does not rely on theoretical predictions for the cross sections σ_A and σ_B. Therefore this model can be used in regimes where the theoretical uncertainty on the production cross section is high by using measurements of σ_A and σ_B.

Measurements and PDFs

The calculation of a cross section using formula 1.43 requires the knowledge of the PDFs. The PDFs that are calculated from first principles differ largely from those obtained from fits to measurements [42]. Therefore measurements are needed to constrain the PDFs of the proton further and finally to understand whether the measurements done at LHC are the results expected from the Standard Model. The analyses presented in this work were performed mainly in order to constrain the PDFs of the proton further.

The for the Drell-Yan process the momentum fraction ξ can be approximated by [43]:

$$x_{1,2} = \frac{Qe^{\pm y}}{\sqrt{s}} \leq \frac{me^{\pm y}}{\sqrt{s}} \tag{1.52}$$

Where Q is the transferred momentum and y the rapidity and m the mass of the produced boson.

With the requirement that x_1 cannot exceed unity this leads to the kinematic limit on y:

$$1 < \frac{me^{\pm y}}{\sqrt{s}} \tag{1.53}$$

$$e^{\mp y} < \frac{m}{\sqrt{s}} \tag{1.54}$$

$$y < \ln\left(\frac{m}{\sqrt{s}}\right) \tag{1.55}$$

This requirement indeed limits the acceptance of LHCb to Z bosons.

1.1.4 Jets

Colour charged particles hadronise as described before. This happens in the non pertubative regime where the QCD coupling constant α_s is of order unity and so is the probability of additional soft emissions. The Q^2 in these emissions is small so it is expected that those soft emissions lead to collimated groups of hadrons that carry the momentum of the initial parton what is usually called a jet in particle physics.

The cross section $e^+e^- \rightarrow$ two jets in QCD is a well defined quantity if the emission of a a soft particle is not measured but diverges if the presence or absence of such an emission is taken into account. [44]. This property is what is called infrared and collinear safety.

That means that a jet definition may not depend on the soft emissions either. Otherwise the measurements can not be compared to predictions within QCD.

A family of jet algorithms based pair wise successive recombination was studied in the literature. There the idea is to go back to the original parton and undo the soft and collinear emissions subsequently in the jet algorithm by pairwise adding up the four-vectors. An example of these algorithms is the anti k_t-algorithm [45] which is used at the LHC experiments including LHCb.

k_t Jet Algorithm

This algorithm starts from a set of proto jets which initially correspond to particles, or particle candidates such as tracks and calorimeter clusters that are combined using the following quantities.

$$d_{i,j} = \min(E_{Ti}^2, E_{Tj}^2)\frac{\Delta_{R_{ij}}}{R} \tag{1.56}$$

defined for a pair of proto jets i, j and

$$d_i = E_{Ti}^2 \tag{1.57}$$

for a given proto jet i. Here $\Delta_{R_{ij}}$ denotes the distance in η, ϕ space. For each step in the calculation it is determined whether one of the $d_{i,j}$s or one of the d_is is the minimal element. If it is a $d_{i,j}$ then the proto jets are merged by adding the 4-momenta[6] otherwise the proto jet i is defined to be a jet and removed from the list of proto jets. This is done until no proto jets are left.

It was shown that this algorithm leads to well defined cross section calculations [45] i.e. it is soft and collinear save.

[6] Other combination schemes are possible.

Computational Aspects

If implemented as described above the algorithm has a cubic computational complexity in the number of proto jets (N). This is impracticable for large number of proto jets as they occur at LHC. Fortunately d_{ij} does not need to be evaluated for all pairs to find the minimum. [46] This is due to the following property of d_{ij} [46]:

$$d_{ij} \text{ minimal} \Rightarrow \Delta_{R_{ij}} \text{ minimal} \tag{1.58}$$

This means only the d_{ij} have to be compared that have the minimal $\Delta_{R_{ij}}$.

Since $\Delta_{R_{ij}}$ is the distance in η, ϕ space this has a geometric interpretation and implies that only the *nearest neighbour* of each proto jet has to be compared. Finding the *nearest neighbour* is a well studied subject in computer science [46]. The idea is to divide the space subsequently into Voronoi[7]-regions. These can be expressed as a Delaunay triangulation and arranged in a binary search tree. Inserting, deleting and finding an element can then be done in $\mathcal{O}(\ln N)$. The *nearest neighbour* of a given node can be read of in approximately constant time. For a comprehensive and clear, albeit slightly dated review the reader is referred to [47].

Anti k_t Jet Algorithm

The distance measure in Equations 1.56 and 1.57 can be generalised in the following way [48].

$$d_{i,j} = \min(E_{Ti}^{2p}, E_{Tj}^{2p}) \frac{\Delta_{R_{ij}}}{R} \tag{1.59}$$

$$d_i = E_{Ti}^{2p} \tag{1.60}$$

with a new parameter p. For $p = 1$ the k_t-algorithm is recovered. In principle all values for p yield a distance measure but $p \in \{-1, 0, 1\}$ is most common. With $p = -1$ the anti-k_t-algorithm is obtained. The anti-k_t-algorithm tends to cluster soft particles to hard particles and tends to produce cone shaped jets in the cases where the jets are separated enough to for separate cones [48]. A graphical comparison of several jets clustered in the same simulated event is shown in Figure 1.2. It can be seen that the anti-k_t-algorithm tends to select cone shaped jets around the high momentum particles while Cambridge/Aachen and k_t cluster jets with a fuzzy boundary. SIScone is a cone based algorithm designed for IR safety [49] and is included for completeness in the overview given in figure 1.2.

[7] Other used transcriptions of Георгий Феодосьевич Вороной include Voronoy, Voronoj and Woronoi.

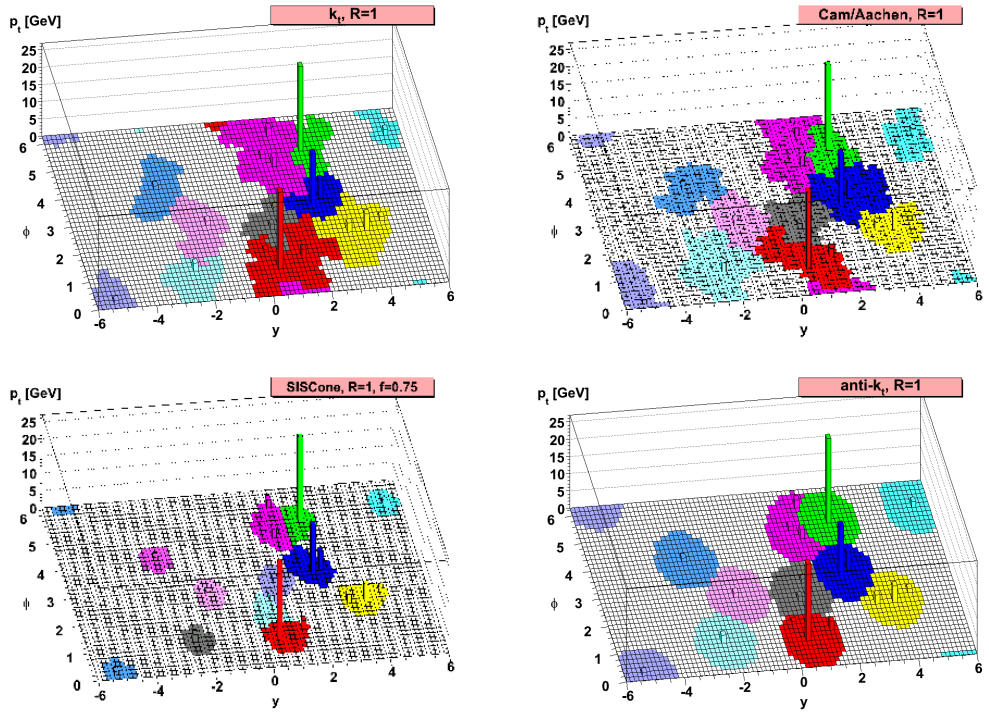

Figure 1.2: The same simulated event (using HERWIG) clustered with different jet algorithms (from [48]. The R parameter was set to unity in all cases. SIScone has another parameter. The overlap parameter set to $f = 0.75$ in this example.

The measurements presented in this thesis use a anti-k_t-algorithm with a R-parameter of $R = 0.5$.

1.2 Detector Description

A sketch of the LHCb detector is shown in Figure 1.3. The apparatus is described in [50]. Unless stated otherwise all information in this section is from that document.

The main focus of the experiment is the study of beauty hadron decays. Several aspects of those decays shaped the design of the experiment. The production of beauty quarks and thus of beauty hadrons is strongly pronounced in the forward and the backward region. Therefore the experiment is a forward detector with an acceptance of $2 < \eta < 4.5$. The lifetime of the hadrons in the $c\tau \approx 500$ µm regime and the small decay width suggests that the identification of beauty decays in the busy events at LHC is possible provided the decay vertices can be discriminated from the primary vertex and the mass resolution is good. Therefore the focus of the experiment is on tracks which can be more precisely measured than calorimeter clusters and do point to the production vertex. The tracking system consists of the vertex locator (VeLo) which is a silicon strip detector very close to the interaction point measuring the radial and azimuthal coordinates; another silicon strip detector with two stereo layers at 5°(TT) in front of a dipole magnet with a peak field strength of 1 T; and another tracking station (T) after the magnet consisting of silicon strip detectors in the forward region (IT) and drift tubes at more central rapidity (OT).

The extensive flavour physics programme of LHCb additionally requires a discrimination between the stable charged hadrons. This is achieved using two ring imaging Cherenkov (RICH) detectors upstream (RICH1) and downstream (RICH2) of a dipole magnet. Electron identification is provided from the shower profile in the electromagnetic (ECAL) and the hadronic (HCAL) calorimeter together with a scintillating pad detector (SPD) and a preshower (PS) detector upfront the ECAL. The ECAL is also capable of the reconstruction of π^0 and γ candidates. Muons are identified using iron filters that can not be penetrated by hadrons interleaved by five coarse tracking stations (M1-M5). Another requirement from flavour physics regards the event rate and the design of the trigger. Since some of the decays to be analysed are very rare, the number of recorded beauty decays should as high as possible. An effective selection of these events requires that the properties of these events are available to the trigger.

1.2.1 Tracking System

The tracking system is the main component of the experiment and is sketched in Figure 1.5. It consists of three tracking stations together with the dipole

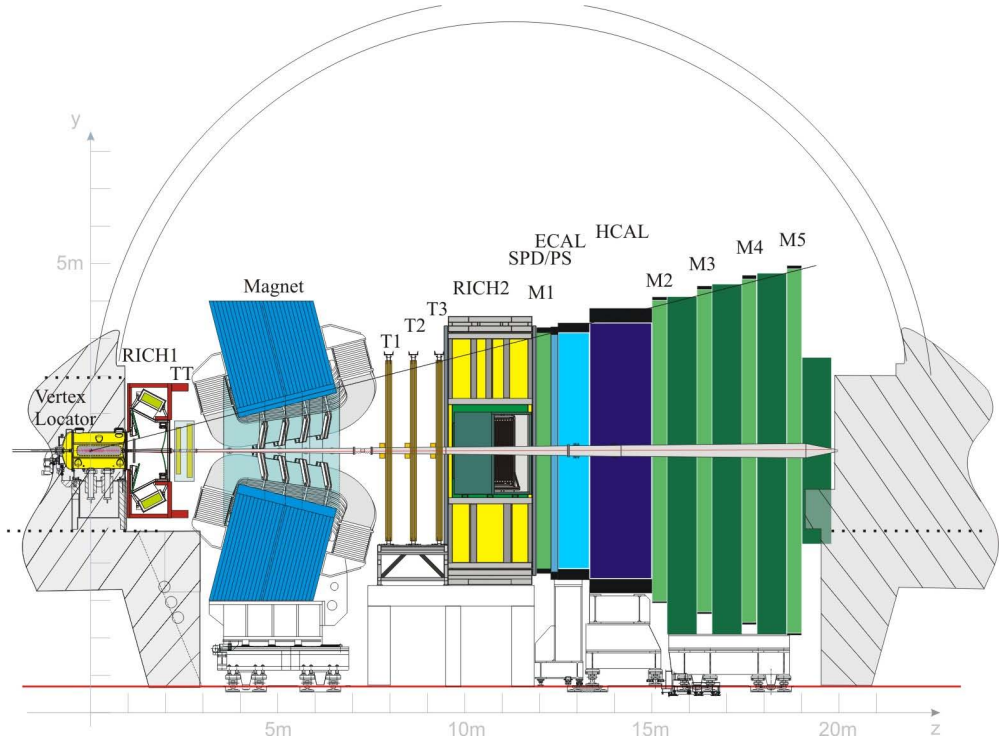

Figure 1.3: Sketch of the LHCb detector. From [50].

magnet. Closest to the interaction region there is the Vertex Locator (VeLo). The VeLo measures the radial (R) and the azimuthal coordinate (ϕ) of the hits. The acceptance of the VeLo is larger than the acceptance of the other subdetectors. The VeLo can be used to reconstruct tracks that originate from a z position around 10.6 cm from the nominal IP that have full fill $1.6 < \eta < 4.9$. Tracks in backward direction can also be reconstructed in the region $-3.5 < \eta < -1.5$ [51]. This aids the reconstruction of primary vertices which is crucial for the secondary vertex reconstruction and lifetime measurements. A sketch of the used sensors is given in Figure 1.4.

The second tracking station is the Tracker Turicensis. Particles arriving at this station did traverse a small fraction of the magnetic field and thus a momentum measurement for low momentum particles is possible. In the original design of the experiment it was foreseen to use this in the high level trigger [52] but this was not implemented. Studies are ongoing in order to change this for LHC run II.

After a dipole magnet with a bending power of 4Tm the so called T station is located. This station consists of the inner tracker (IT) which is a silicon strip detector and the outer tracker which consists out of drift tubes.

There are several track types in LHCb.

VeLo tracks are tracks that are measured only by the VeLo. Those tracks are mainly used to find the primary vertex and the decay vertices. The magnetic field integral seen by these tracks is small and thus there is no momentum estimate available.

backward tracks are like VeLo tracks but those tracks are pointing in the backward direction.

upstream tracks are VeLo tracks extrapolated to the TT station and matched to hits in the TT station. These tracks do see the fringe field of the magnet and thus have a momentum estimate. These tracks can in principle be reconstructed at very low momentum but practically the momentum acceptance is limited by the search windows in the algorithm to $p_T \gtrapprox 200\,\mathrm{MeV}$.

T tracks are tracks reconstructed in T stations only. These tracks don't see a large magnetic field inside the measured segment but together with the assumption that they originate from the PV they can get a momentum estimate assigned. These tracks play a role as intermediate objects in the reconstruction of other tracks and also for the understanding of the contribution of secondary particles to the photons seen in RICH2.

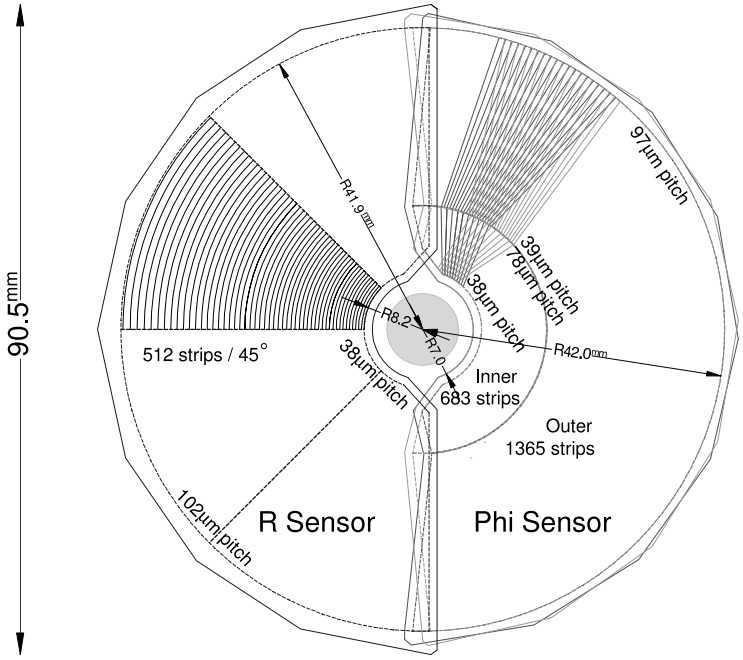

Figure 1.4: Sketch of the r and ϕ sensors used in VeLo [50]. To cope with the higher occupancy in the r sensors the strip pitch is reduced towards the centre. In the ϕ sensors the strip pitch reduces for purely geometrical reasons. Additionally the ϕ sensors have a kink in the central region. The direction of the kink is alternated which leads to a stereo view in the ϕ sensors. Both sensor types are subdivided. The ϕ sensors are read out in an inner region and an outer region while the r sensors are read out for each quadrant individually leading to two readout regions per sensor.

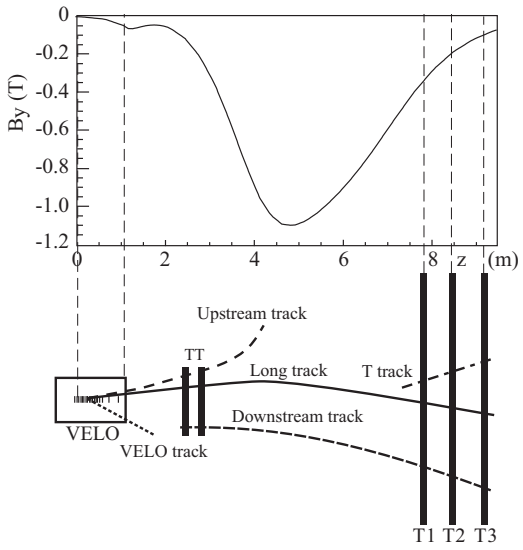

Figure 1.5: Track types used in LHCb. For reference the main component of the magnetic $B_y(z)$ is given. [50].

They are also used to veto charged particles in the neutral hadron reconstruction for jets as described in Section 3.1.1.

downstream tracks are T tracks matched to hits in the TT station. Those tracks have measurements on both sides of the dipole magnet and thus a well measured momentum. For physics analyses they are of special importance for the reconstruction or K^0_S and Λ which often decay after the VeLo.

long tracks are tracks that do have measurements both in the VeLo and the T stations. Hits in the TT station are not required for a long track and added when found compatible. If found these hits improve momentum resolution and reduce the probability that the long track is a random combination of hits that does not correspond to a real particle i.e. a ghost. Long tracks are the major workhorse of the physics analyses.

μ stubs are tracks reconstructed in the muon system only. Their major use is in the earliest trigger stage. With the assumption that muons tracks originate from the luminous region a momentum estimate is possible. This allows to trigger on high momentum muons and dimuons.

μ TT tracks are muon stubs reconstructed offline that are matched to hits in the TT station. Those track are mainly used for the estimation of the efficiency for the reconstruction of long tracks.

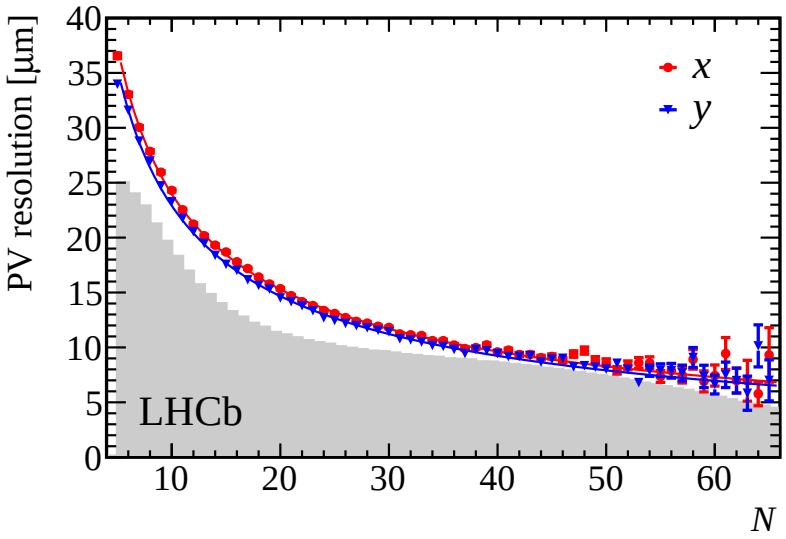

Figure 1.6: Primary vertex resolution in both transverse coordinates as a function of the number of tracks.

TT tracks are not reconstructed since the TT station has four layers with a stereo angle. Thus a particle leaving hits in all layers would have two points measured that can be reconstructed as a straight line. There is no redundancy in such a measurement and thus no χ^2 and no handle to discriminate ghost tracks.

The performance of the tracking system is illustrated in Figure 1.8 using the decay $\Upsilon(1S)\to\mu^+\mu^-$ as benchmark. The measured invariant mass is dominated by the track momentum measurement and has a resolution of 43 MeV [53]. The PV and impact parameter resolution are shown in Figures 1.6 and 1.7.

1.2.2 Cherenkov Detectors

Several radiators are used in order to reach a good sensitivity in a large momentum region. There are two radiators (Aerogel and C_4F_{10}) in RICH1 and one radiator (CF_4) in RICH2. Nevertheless the detection principle of measuring the velocity and comparing that to the measured momentum is limited by special relativity. With a finite resolution the velocity inevitably becomes compatible with the speed of light at high momentum. The limit for LHCb is $p \lessapprox 100$ GeV.

The reconstruction algorithm calculates for each reconstructed track the electron, muon, pion, kaon and proton hypothesis and fits this to the observed

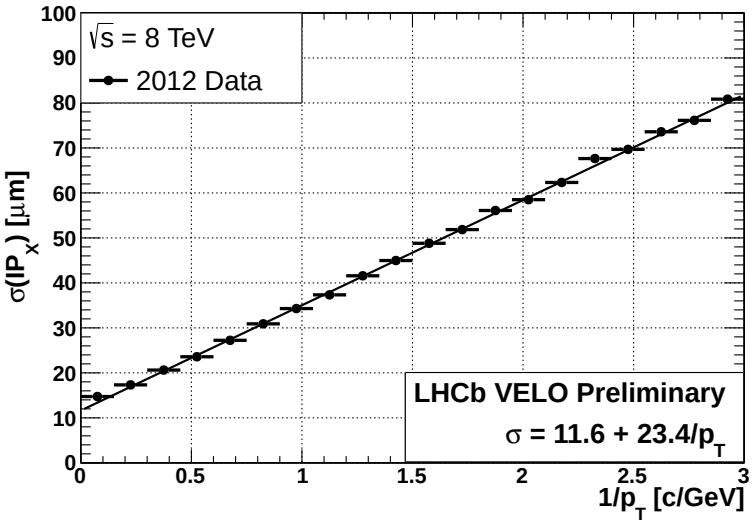

Figure 1.7: Impact parameter resolution in x direction.

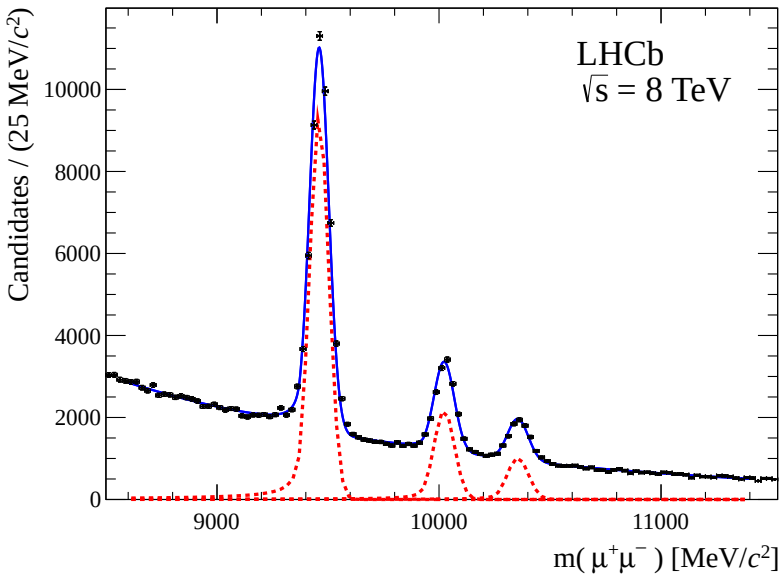

Figure 1.8: Invariant mass distribution of dimuon events with the $\Upsilon(1S)$; $\Upsilon(2S)$ and $\Upsilon(3S)$ resonances [53].

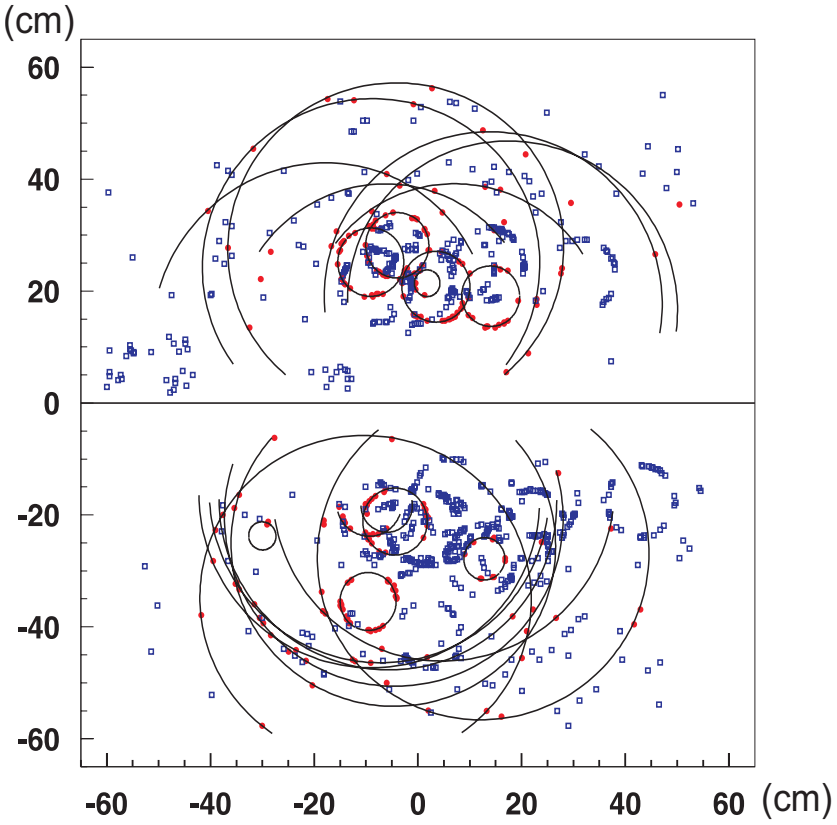

Figure 1.9: Simulated event as seen from RICH1 [50].

photons in the RICH detectors. This leads to a delta log likelihood estimation with respect to the pion hypothesis. The result of such a fit on simulated data is shown Figure 1.9. The measured Cherenkov angles for the C_4F_{10} in RICH1 are shown in Figure 1.10. Standalone ring finding algorithms are available but are not used in the standard reconstruction.

1.2.3 Calorimetry

The calorimeter system is mainly designed for the use in the trigger and for particle identification. It consists of the scintillating pad detector (SPD); the preshower (PS); the electromagnetic calorimeter (ECAL); and the hadronic calorimeter (HCAL). It consists of the following components.

SPD is the first layer. It consists of scintillating pads of different size made from doped polystyrene which are read for each bunch crossing using wavelength shifting fibres. It serves two purposes. In the earliest trigger stage the number of pads that see a signal is used as a measure of the

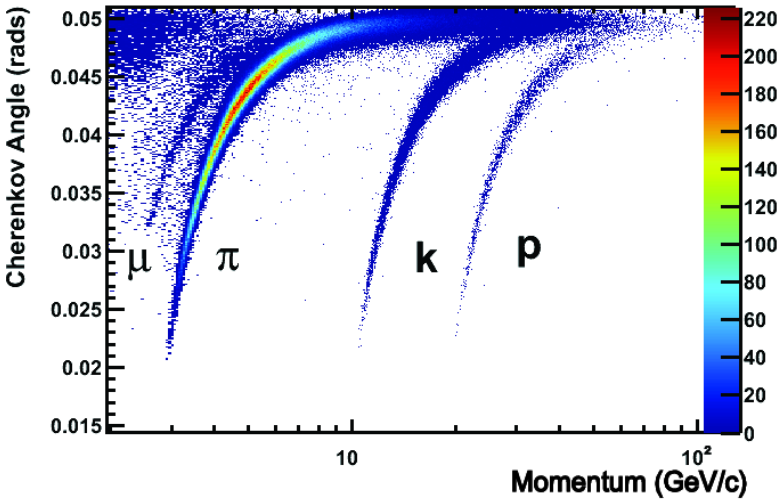

Figure 1.10: Distribution of Cherenkov angle and momentum in the C_4F_{10} radiator gas of RICH1 [54].

total occupancy. Events with less than 10 cells fired are selected by the triggers for exclusive processes. The total multiplicity is also used to reject events at the trigger level that require a lot of CPU time in the later software triggers. The single muon trigger that was used for most of the available data requires the multiplicity to be less than 600 hits and the dimuon trigger asks for less than 900 hits. The second use of the SPD is the discrimination of electron and photon candidates both at trigger level and offline. Electrons are more likely to leave a signal in the SPD since that detector doesn't contain absorbers.

PS is the preshower detector. It is build in a similar way as the SPD but separated from the SPD by a 15 mm lead plate which corresponds to 2.5 electromagnetic radiation lengths. This is used to discriminate electrons and photons from hadrons.

ECAL is a calorimeter build in the shashlik technology. That is a structure of lead tiles interleaved by scintillator tiles which are read out by wavelength shifting fibers. It covers 25 electromagnetic radiation lengths. The design energy resolution is given by:

$$\frac{\sigma_E}{E} = \frac{10\%}{\sqrt{E}} \oplus 1\% \tag{1.61}$$

with the energy E measured in GeV. The ECAL is designed for the energies occurring in flavour physics. At very high momentum it saturates

which limits the bremsstrahlung corrections on electrons and significantly worsens the mass resolution in the Z $\rightarrow e^+e^-$ measurements [55].

HCAL The HCAL is not meant to reconstruct particle candidates to be used in any offline analysis. Its main purpose is to provide a trigger for full hadronic final states of the beauty hadrons. Therefore compromises have been made – especially in terms of the limited space in the cavern – leading to a calorimeter that uses 5.6 hadronic interaction lengths in only 1.6 meters and has a resolution of:

$$\frac{\sigma_E}{E} = \frac{69 \pm 5\%}{\sqrt{E}} \oplus 9 \pm 2\% \tag{1.62}$$

with the energy again measured in GeV. Most analyses use the HCAL only for triggering and PID purposes but using neutral HCAL clusters improves the jet energy resolution.

1.2.4 Trigger

The trigger is organised in three stages. The first level (L0) is implemented in hardware and reduces the rate from the 20 MHz collision rate[8] to about 1 MHz. At this stage muon candidates from the muon stations, hadron candidates from the HCAL, electron candidates from the ECAL and exclusive events with a low number of hits in the SPD are selected and global event cuts - again on the SPD multiplicity are applied. This trigger step is performed using limited information in FPGAs within the strict time limit of 4 µs. When a trigger arrives too late the data are already replaced at the front end derandomiser buffer. L0 accounts for the bulk of inefficiencies in the whole trigger chain.

After a L0 trigger the whole detector is read out and the Hlt1 trigger is executed on standard CPUs. At this stage the candidates from L0 are verified. Since the analyses described in this thesis only use muon triggers I restrict the description to those. For the muon candidates seen in L0 a track is searched and a track fit is performed. Single muons are selected if they have high momentum $p_T \gtrapprox 5\,\text{GeV}$ or intermediate momentum together with a significant impact parameter. The actual selection varying with the trigger configuration. The configurations changed with the running conditions and are identified by Trigger Configuration Keys (TCK) which are summarised in Table 1.2.

[8]This is the approximate frequency of the bunch crossings for most of the data corresponding to the runs at 50 ns bunch spacing. The trigger is designed to run the the nominal bunch spacing of the LHC of 25 ns corresponding to 40 MHz.

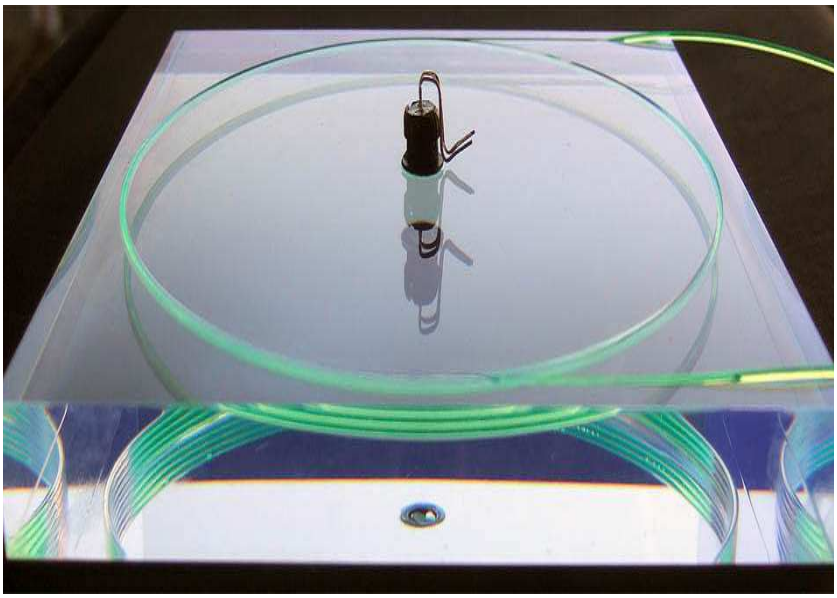

Figure 1.11: Tile in the scintillating pad detector [50].

The last trigger stage (Hlt2) is only logically separated from Hlt1 but technically it is executed in the same process as Hlt1 just only on events selected by Hlt1. In this stage also combinations of reconstructed particles are build. This is done for specific decays like $\Omega^- \rightarrow \Lambda K^-$ with $\Lambda \rightarrow p\pi^-$ as well as generic objects like detached J/ψ; high mass secondary vertices; and high momentum leptons.

The amount to CPU time available to the software trigger is increased by the use of deferred triggering [56]. For this the data are buffered on a disk directly on the trigger node and once the LHC beams are dumped the trigger processes the events from the disk instead of the events from the detector. Depending on the length of the fill this leads to about 30% additional CPU time available to the software trigger. The output of the software trigger is about 5kHz and is limited by the amount of data that can be stored and analysed offline.

1.3 Datataking Conditions

The choices and achievements of both LHC and LHCb affect the measurements possible with the given datasets. In this section the properties of the available datasets is outlined. The focus is on the $Z \rightarrow \mu^+\mu^-$final state and properties that affect the measurement of Z production.

1.3.1 LHC Beam Configurations

2010

The year 2010 saw the turn on of LHC after the accident of 19$^{\text{th}}$ September 2008 that destroyed a seizable fraction of sector 3–4 [57]. In order to diminish the risk of another accident the beam energy was reduced to 3.5 TeV with respect to the design energy of 7 TeV and the commissioning of LHC was done very precautiously in small steps. The nominal LHC beam carries a large amount of energy which can cause a substantial damage to the detectors and also to the accelerator itself if it is deposited anywhere else than on the beam dump. Therefore the concept of the *save beam* was implemented. Several operations on the beam are only allowed as long as the stored energy does not exceed certain thresholds. The same was used in beginning of the run to commission the safety systems and to verify that the full beam can always be disposed properly on the beam dumps in case of any perturbation. In the first phase there were many fills with single bunch injections leading to fills with up to 13 bunches per beam. The beam conditions monitor (BCM) thresholds and other safety interlocks were set to very low dump thresholds leading to a large number of protective beam dumps mainly at the injection. In the beginning the single bunches charge was set to low values of maximum $2 \cdot 10^{10}$ protons. This was done at a squeeze (β^*) from $\beta^* = 10 - 11$m up to $\beta^* = 2$m for all IPs. In a second phase the bunch charge was increased to the nominal value of about $1.15 \cdot 10^{11}$ protons and with 50 bunches in the machine. The squeeze was reduced to $\beta^* = 3.5$m. The 2010 proton run concluded with the commissioning of bunch train injections at a bunch spacing of 150 ns and a period of luminosity production with these conditions and finally a test of 50 ns bunch spacing at the end of the run [58]. In this fill electron cloud build up as observed at several segments of the machine. It was found that beam scrubbing is an option to reduce electron cloud effects. In scrubbing runs the beams are configured to generate large electron cloud effects in order to treat the inner surfaces of the beam pipe. After such treatment the walls of the vacuum enclosure are less likely to emit electrons in the vacuum [59]. Afterwards the LHC was filled with lead ions in both beams with collisions in IP1, IP2 and IP5.

The polarity of the LHCb dipole magnet was reversed twelve times resulting into small changes of the crossing angle in IP8. The ALICE solenoid and dipole magnets were reversed five times. The latter requires changes in the accelerator optics since the ALICE solenoid doesn't have dedicated corrector magnets. The energy for the physics runs was 3.5 TeV with a few fills at injection energy of 450 GeV in the proton programme. In order to

benefit from the experience from the proton runs the accelerator optics for the ion runs were set very similar to those in the proton runs. That lead to a beam rigidity of 3.5 TeV *per proton in the lead nucleus* and beam squeeze $\beta^* = 3.5$m.

2011

LHC was operated at 3.5 TeV with bunch trains most of 2011. The bunch spacing was reduced from 75 ns in the beginning of the year to 50 ns. The number of bunches in the machine peaked at 1380 bunches which is close to the theoretical limit for 50 ns bunch spacing. The limit on the number of bunches arises from the circumference of the rings, which defines the number of available RF buckets, together with the rise and fall times of both the injection and the extraction kickers. The squeeze was set to $\beta^* = 3$m at IP8 which is to be compared to an $\beta^* = 1$m at IP1 and IP5.

With that many bunches in the machine the luminosity for LHCb was reduced with respect to IP 1 and IP5. To achieve that a luminosity-levelling system was implemented at IP8. When luminosity production starts the beams are brought into peripheral collisions until an measurement of the instantaneous luminosity is possible. Then the beams are brought closer until the target luminosity of $(2 - 3.5) \cdot 10^{32}/c\text{m}^2\text{s}$ is reached. At the end of exceptionally long fills the beams were collided head on without reaching the target luminosity any more. This is due to the large β^* and occurred only when the injectors were unavailable. Similar to 2010 there were also lead ion runs mostly with the injection on batches of 24 bunches at a 200 ns spacing [60]. In 2011 the accelerator delivered $1.22\,\text{fb}^{-1}$ of integrated luminosity to IP8. On the request of the ALICE collaboration the accelerator was tuned to 1.38 TeV for four fills (1650, 1651, 1653 and 1658).

2012

After many studies on the risk from the faulty joints in the superconducting interconnects of the machine [61] it was decided to increase the energy to 4 TeV per beam. The bunch spacing was kept at 50 ns. A further reduction down to the LHC design value of 25 ns was not successful due to insufficient intensity from the injectors and electron cloud build up. The discovery of a particle like the Higgs boson by ATLAS and CMS fell into the 2012 data taking period. Therefore the whole year was devoted to luminosity production at 4 TeV and the special runs were shifted to 2013 also delaying the long shut down (LS1). The luminosity levelling system at IP8 was used for most of the data taking. In preparation for the ion run in 2013 protons and lead

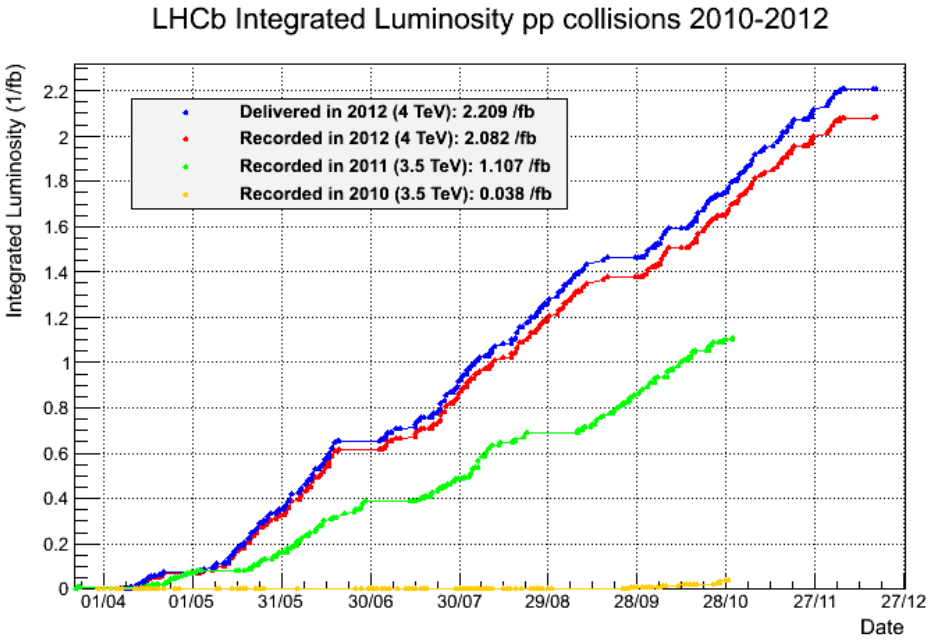

Figure 1.12: Integrated luminosity taken by the LHCb experiment in the years 2010, 2011 and 2012.

ions were collided at all IPs for a short period. Neon was injected into the interaction region at IP8 in order to measure the beam profile. This also allows to observe fixed target pNe collisions in LHCb [62].

2013

The accelerator operation was dominated by the pPb and Pbp runs. Those require both beams to be filled with different particles. At injection energy the velocity is about 97%c for ions and 98%c for protons and the difference does not diminish at maximum energy. At injection and ramp the difference is accounted for be different revolution frequencies while keeping the beams on the central orbits. Since having different revolution frequencies is equivalent to a spacial shift of the beam beam encounters the revolution frequencies are equalised at flat top and afterwards the acquired phase shift of several microseconds is shifted back to zero. This means the beam encounters are moved by several kilometers back to their nominal positions. When the revolution frequencies are locked at 4 TeV the beams deviate up to 1.5 RMS of the beam size in the horizontal plane from there central orbit. Finally the LHC run I was concluded with another run at 1.38 TeV at low intensity.

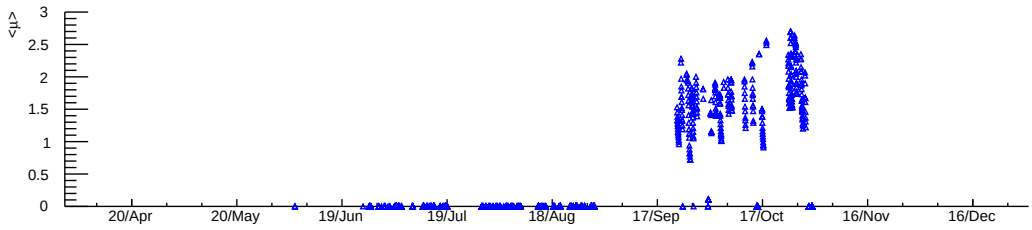

(a) Proton proton collisions in 2010

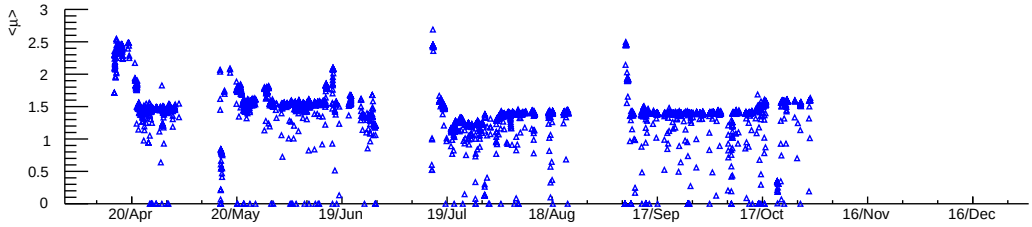

(b) Proton proton collisions in 2011

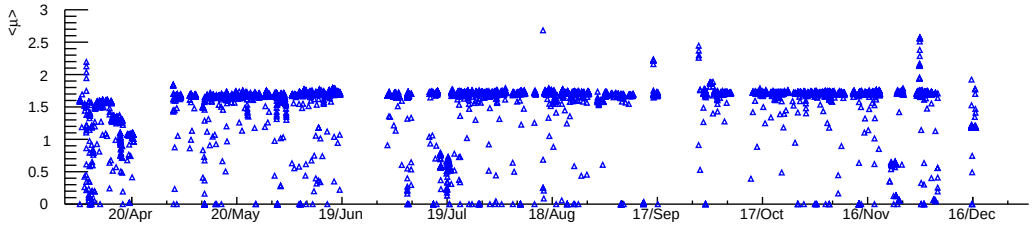

(c) Proton proton collisions in 2012

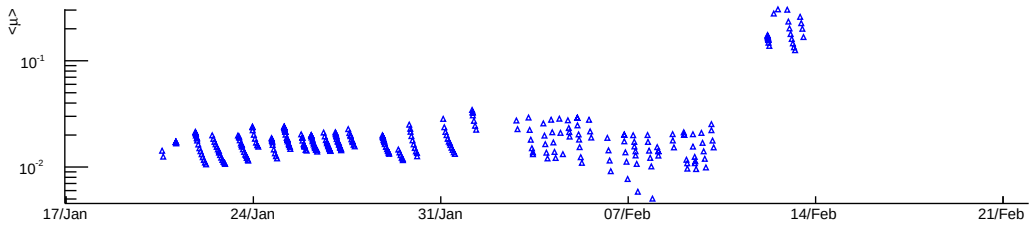

(d) 2013. Before February 12$^{\text{th}}$ this are pPb and Pbp collisions at 4 TeV and afterwards pp collisions at 2.76 TeV. Please note that this plot has a log scale unlike the other plots.

Figure 1.13: Comparison of the number of visible iterations in the different proton proton data taking periods.

	$\sqrt{s_{NN}}$			
2010	900 GeV	0.2 nb^{-1}	pp	[63]
2010	7 TeV	36 pb^{-1}	pp	
2010	5.02 TeV		PbPb	LHCb off
2011	7 TeV	1 fb^{-1}	pp	
2011	5.02 TeV		PbPb	LHCb off
2012	8 TeV	2 fb^{-1}	pp	
2012	2.76 TeV		pp	VeLo at 10 cm
2012	5.02 TeV	0.93 μb^{-1}	pPb	[62]
2012	87 GeV		pNe	fixed target [62]
2013	2.76 TeV	3.3 pb^{-1}	pp	magnet down only. See chapter 5.
2013	5.02 TeV	1.4 nb^{-1}	pPb	[64]
2013	5.02 TeV	0.6 nb^{-1}	Pbp	[64]
2013	87 GeV		pNe	fixed target

Table 1.1: LHC physics runs and LHCb configurations over time. Unless cited other the luminosity numbers are taken from the online system and carry a large uncertainty. If a value is zero there was no information available in the run database.

1.3.2 Data Taking Periods

2010

LHCb operation was interrupted by the LHC accident [57] in 2008. The additional time was well spend to integrate the detector and tune the readout chain. When LHC beam operations resumed in 2010 LHCb kept up with the large experiments in instantaneous and thus integrated luminosity and exceeded the design number of visible interactions per bunch crossing from a design value of 0.4 to 2.5 without the detector performance degrading [65]. The incremental startup of the machine lead to physics runs at very low luminosity with a low number of interactions per bunch crossing and a very open trigger configuration.

Also collisions at the injection energy are available. Both of these datasets are used for analyses mainly on general event properties [63, 66–68]. The results benefited a lot from these unique conditions of low number of interactions. There was no participation of the LHCb experiment in the lead ion runs. Therefore several interesting processes like central exclusive particle production in ion collision could not be studied. From todays perspective the high luminosity runs at $\sqrt{s} = 7\,\text{TeV}$ are superseded by the data taken in

2011 at the same energy but some of the very early runs with very low pile up and open trigger remain to be of interest. The current published measurements of Z production are based on the full data [69] taken but an update using the 2011 data is being prepared [70]. The integrated luminosity taken by LHCb in 2010 is $36\,\mathrm{pb}^{-1}$. This is very similar to the integrated luminosity at ATLAS and CMS in the same period.

2011

The increased number of bunches; the high bunch intensity together with the luminosity levelling system allowed for stable data taking conditions at a instantaneous luminosity in the range $(2-3.5)\cdot 10^{32}/\,\mathrm{cm}^2\mathrm{s}$. The majority of results presented in this thesis is based on these data. In 2011 the LHCb experiment took 1 fb of integrated luminosity at $\sqrt{s} = 7\,\mathrm{TeV}$. In order to leave space for a larger LHC aperture for the fills at $\sqrt{s} = 2.76\,\mathrm{TeV}$ the VeLo was not fully closed [71]. The VeLo was moved in leaving 10 mm more distance between the halves with respect to the nominal data taking position. This corresponds to a distance of 13 mm to the interaction point. This reduced the vertex quality, the track resolution and thus the RICH PID. There is a J/ψ production measurement from this data taking period [71]. There was no participation of the LHCb experiment in the lead ion runs.

2012

In 2012 LHCb took the first data in proton-lead collisions of about $0.93\,\mu\mathrm{b}^{-1}$ at 5.02 TeV in a so called pilot run [62]. Neon gas was injected into the interaction region in order to measure fixed target collisions at $\sqrt{s} = 87\,\mathrm{GeV}$ [62]. In 2012 LHCb tripled the amount of available integrated luminosity available for the study of beauty hadrons to $3\,\mathrm{fb}^{-1}$. Since the energy was increased to $\sqrt{s} = 4\,\mathrm{TeV}$, the 2011 and the 2012 dataset has to be treated separately for production measurements.

2013

In 2013 LHC made several pPb, Pbp runs at 5.02 TeV and proton runs at 2.76 TeV. The neon injections were used as well. In all of these runs LHCb participated. There are two Z analyses based on these data so far. One is described in [64](pPb, Pbp) and the other is presented in chapter 5.

1.3.3 High Momentum Muon Triggers

The rates for high p_T physics like Z production are much lower than the rates for b hadron production. Since LHCb is designed for studies of b hadrons it is also designed to cope with the high production rates of these hadrons. This implies that the rate increase due to the triggers for electroweak bosons is small even for loose selections at trigger level. What limits the trigger for high momentum physics is the execution time in the trigger and even offline. If there are many hits in the detector the number of candidate tracks increases about exponentially and so does the execution time. In the HLT system execution times exceeding 45 minutes for a single event were observed. Offline the execution time exceeded a day per event for exceptional events taken in the heavy ion runs. For the study of B mesons it is more efficient to remove a few very busy events and reconstruct more events in total.

The software trigger farm was upgraded continuously but still has limited computing capacity [72, 73]. Therefore global event cuts(GEC) were introduced in 2010. Those rely on quantities whose reconstruction time is fast. linear and does not require looping over hits. The most important requirement is the number of hits in the SPD detector n_{SPD} to be smaller than $n_{\mathrm{SPD,max}}$. Loose GEC are required for stable operations to prevent the Hlt farm to be clogged by a few events. The GEC in place for most of the running were much harsher than what is absolutely needed. Since quieter events are better for flavour physics the GEC were chosen harder and the event rate was increased with respect to what would have been possible with minimal GEC. There is no separation between the high momentum and the flavour trigger lines. Every event that is accepted by a Hlt1 physics line is completely processed in Hlt2.

That means for example that anything passing on the single muon line in L0 and Hlt1 will be checked for charm and beauty hadrons by means that rely on the full reconstruction of complex decays and therefore suffer from large combinatorial complexity in busy events. The GEC needed to have all charm and beauty triggers being executed in a suitable time is much harsher that the GEC up to which muon reconstruction works efficiently. But since in the past configurations the beauty triggers always ran in all accepted events also the GEC needed for those were applied. The execution is also not interrupted once the decision has been made to take the event leading to additional CPU time used without effects on the global trigger decision. However this can only help with accepted events since for rejected events all trigger lines have to run. Nevertheless these events tend to be busier than the events without any signal process.

1.3.4 Trigger Strategy for Z Bosons

The trigger strategy for all analyses presented in this work is always the same. The offline selection requires two muons and this is what these events are triggered on. Even though there are dimuon triggers the choice was made to use the single muon triggers only. This has the advantage that a local inefficiency in the trigger has less impact since there is always the other muon. Due to the large invariant mass of the Z boson the second muon is always in a different detector region. Therefore the trigger decisions on both muons are assumed to be statistically independent which largely aids in the efficiency determination.

The major downside of this strategy is the harsher GEC applied on the single mount trigger lines with respect to. the dimuon triggers. But still the overall efficiency for inclusive Z production is higher in the single muon trigger channel. The inefficiency is mainly due to the muon reconstruction in L0. Nevertheless it in principle possible to recover the events at high occupancy by using the dimuon trigger in the region $n_{\mathrm{SPD,max}(1\mu)} \leq n_{\mathrm{SPD}} \leq n_{\mathrm{SPD,max}(2\mu)}$. That would reduce the inefficiency and thus the uncertainty on the efficiency of the GEC to the sub percent level. That procedure is not applied in the available measurements involving Z bosons. During the LHCb running period the trigger configuration was changed several times which has to be taken into account when the efficiency is determined. The changes were due to increased luminosity; more nodes added to the Hlt farm; physics requests and other reasons. The different trigger configuration keys are summarised in Table 1.2 and categorised in equivalence classes. An class is considered equivalent if there was no change on the configuration of the loosest single muon lines without impact parameter requirement or prescale.

1.3.5 Lessons learned and Options for the Future

Trigger in special Conditions

The trigger needs more attention in "special conditions". The available total luminosity will usually be small. Therefore many measurements will be limited by the available statistics. That means that many of the prescales have to be removed and that some of the selections have to be adjusted. There has been significant impact on the charm cross section measurement in the 2013 pp run due to such an mistake.

TCKs hexadecimal	Line Name	p_T GeV	p GeV	χ^2_{Track}	prescale	int. luminosity pb^{-1}
	2010					
0e001f	Hlt1SingleMuonNoIPL0	1.35		100/50	1.	0.0085
	Hlt2PassThrough			1.		
12001f, 13001f, 190024	Hlt1SingleMuonNoIPL0	1.35		100/50	1.	0.3
	Hlt2PassThrough				1.	
	Hlt2SingleHighPTMuon	10.			1.	
14001f, 17001f, 19001f, 190024	Hlt1SingleMuonNoIPL0	1.35		100/50	1.	5.0
	Hlt2PassThrough				.01	
	Hlt2SingleHighPTMuon	10.			1.	
1d0030, 1e0030, 24002a, 24002c, 2a002a, 2a002c, 2e002a, 2e002c	Hlt1SingleMuonNoIPL0	1.8		100/50	1.	26.2
	Hlt1SingleMuonNoIPL0High	5.		16/10	1.	
	Hlt2SingleHighPTMuon	10.			1.	
1f0029, 1f0031, 25002a, 25002c, 2b002a	Hlt1SingleMuonNoIPL0	1.8		16/10	.2	5.8
	Hlt1SingleMuonNoIPL0High	5.		16/10	1.	
	Hlt2SingleHighPTMuon	10.			1.	
	2011					
360032	Hlt1SingleMuonHighPT	4.8	8.		1.	3.4
	Hlt2SingleMuonHighPT	10.			1.	
480032, 4a0033, 5a0032, 5b0032, 5d0033	Hlt1SingleMuonHighPT	4.8	8.	3	1.	75.6
	Hlt2SingleMuonHighPT	10.			1.	
6d0032, 700034, 710035, 730035, 760037, 790037, 790038	Hlt1SingleMuonHighPT	4.8	8.	3	1.	10^3
	Hlt2SingleMuonHighPT	10.			1.	
	2012					
7e0039, 7e003a, 7f0040, 860040	Hlt1SingleMuonHighPT	4.8	8.	5	1.	6.3
	Hlt2SingleMuonHighPT	10.			1.	
8c0040, 8e0040, 94003d, 95003d, 97003d	Hlt1SingleMuonHighPT	4.8	8.	3	1.	605
	Hlt2SingleMuonHighPT	10.			1.	
990042, 990043, 990044, 9a0042, 9f0045, a10044, a10045, a20044, a30044, a30046, a90046, ab0046, ac0046, ac0047, ad0046, ae0046	Hlt1SingleMuonHighPT	4.8	3.	5	1.	$1.4 \cdot 10^3$
	Hlt2SingleMuonHighPT	10.			1.	
	2013					
a90046	Hlt1SingleMuonHighPT	4.8	3.	5	1.	3.3
	Hlt2SingleMuonHighPT	10.			1.	

Table 1.2: Overview over the high momentum muon triggers. Most of the numbers in this table are online luminosity and have a large uncertainty.

Trigger for high Momentum Physics

There are proposals to measure $t\bar{t}$ production asymmetries in LHCb [74, 75]. The GEC need special attention for these very busy signal events. If one wants to be able to trigger on these events a loose GEC would be advisable. An option for a loose GEC single high p_T muon trigger that is fast would be a strategy based on an L0 similar to L0MuonHigh as it was used in 2010 (L0TCK 0x2a). On this a dedicated Hlt1 single muon line could run. If this needs to be speeded up instead of GEC the tracking search windows could be tightened with respect to the low momentum triggers. In case the rate is still to high that can be accompanied a minimal requirement on the sum of the calorimeter energy as it it used in the jet triggers. This could already be applied in L0.

This strategy might allow to trigger even on $t\bar{t}$ with one W decaying hadronically. This channel would increase the sensitivity with respect to the current proposals.

A similar trigger strategy was in place in 2010 when the harsh GEC where applied in

- `Hlt1SingleMuonNoIPL0HighPT`,
- `Hlt1SingleMuonNoIPL0` and
- `Hlt1SingleMuonIPCL0`

but not in

- `Hlt1SingleMuon4BsMuMu`.

All Hlt2 lines I checked did not run on events triggered by the Hlt1 line `Hlt1SingleMuon4BsMuMu`. This was in place for TCK 0x25002a in 2010.

Lead Ions

The lead lead collisions are of interest even if high centrality events may be difficult or impossible to reconstruct. Exclusive production certainly is reconstructible.

Low Pileup Data using Satellite Bunches

In some fills (e.g. 2261) in 2011 the spill over in the RF buckets shifted by 25 ns was enhanced to a few percent of the main bunch intensity. Those collided with full size bunches injected with an offset of 25 ns in IP2 to provide low pileup conditions to ALICE while providing high luminosity to ATLAS

and CMS. That procedure was proposed for Atlas and CMS in in order to take both low an high pileup data in the same runs [76]. This should be possible for LHCb as well. The lost luminosity should be marginal but the exclusive production measurements could potentially benefit a lot. The downside of such an approach would be that nominal beam optics would have to be used for ALFA and TOTEM which also need low pileup data but at high β^*.

Chapter 2

Z Boson Reconstruction in LHCb

Z boson reconstruction is a common effort in the Electroweak Group of the LHCb collaboration. Z bosons are reconstructed using all decays to charged leptons. The the best mass resolution is achieved in the dimuon final state. If the electron positron or the ditau final state is used a sizable fraction of energy is lost due to bremsstrahlung and neutrinos. Nevertheless also in the electron positron final state precision measurements are possible. In this chapter the main focus will be on the the Z reconstruction in the dimuon final state. My contribution was to the efficiencies used in [69, 77] but this refers to an outdated reconstruction version (Reco 12). Therefore a similar analysis as described in [1] will be described here.

2.1 Overview over the Measurements of Z Boson Production in LHCb

- $Z \to e^+e^-$ was measured at 7 TeV [55] using $1\,fb^{-1}$. This measurement includes several differential distributions.
- $Z \to \mu^+\mu^-$ was subject to many studies in LHCb.
  - Inclusive measurement using $36\,pb^{-1}$ [69] and a preliminary result using $1\,fb^{-1}$ [70] both at 7 TeV.
  - Associated production with jets [77] and D mesons [78]. Those measurements are described in the Chapters 3 and 4 respectively.
  - Measurement of the production cross section in proton lead collisions [64].
  - Differential cross section in proton proton collisions at 2.76 TeV. This will be described in Chapter 5 This measurement is not an official LHCb result yet.
- $Z \to \tau^+\tau^-$ was measured in several τ final states [79] and extended to a $h \to \tau^+\tau^-$ search [80].

As illustration the invariant mass distributions for the different measurements are summarised in Figures 2.1 to 2.3, 4.12 and 5.3 The best mass resolution is achieved in the muon final state. For the electron final state a large fraction of the energy is lost in bremsstrahlung which can only partially be recovered in the ECAL due to saturation. Nevertheless the electron measurement adds the overall result since some of the systematic uncertainties are not correlated. The reconstruction of the $Z \to \tau^+\tau^-$ final state suffers from the energy carried away by the neutrinos and thus larger background as well as the reduced statistics from the τ branching fractions. In the high statistics channels $Z \to e^+e^-$ and $Z \to \mu^+\mu^-$ (plus jets) also differential measurements were performed. Figures 2.5 to 2.7 and 3.23 to 3.28 are shown as examples.

In Figure 2.5 the LHCb measurement is extrapolated to the fiducial volume of a measurement by Atlas. It can be seen that the Z production cross section is larger at low absolute rapidity. This can be seen from Equation 1.52 keeping in mind that the valence quark PDFs peak around $1/3$. When the acceptance of the LHCb detector is taken into account the rapidity distribution peaks around 2.8. This is shown in Figure 2.6. The loss at low rapidities originates from the requirement to have both muons at a pseudorapidity $\eta > 2$.

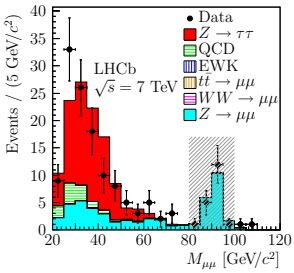

(a) $Z \to \tau^+\tau^-$ candidates with both τs decaying as $\tau \to \mu\bar{\nu}_\mu\nu_\tau$. The shaded area is vetoed in the analysis due to the background from $Z \to \mu^+\mu^-$.

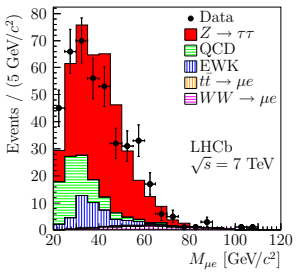

(b) $Z \to \tau^+\tau^-$ candidates with one τ decaying as $\tau \to e\bar{\nu}_e\nu_\tau$ and the other as $\tau \to \mu\bar{\nu}_\mu\nu_\tau$. This channel required $p_{T,\mu} > 20\,\text{GeV}$ and uses the μ to trigger.

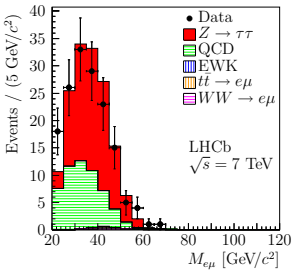

(c) $Z \to \tau^+\tau^-$ candidates with one τ decaying as $\tau \to e\bar{\nu}_e\nu_\tau$ and the other as $\tau \to \mu\bar{\nu}_\mu\nu_\tau$. This channel required $p_{T,\mu} < 20\,\text{GeV}$ and uses any of the leptons to trigger.

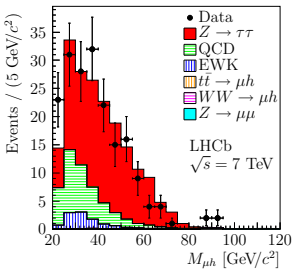

(d) $Z \to \tau^+\tau^-$ candidates with one τ decaying as $\tau \to \mu\bar{\nu}_\mu\nu_\tau$ and the other as $\tau \to h\nu_\tau$

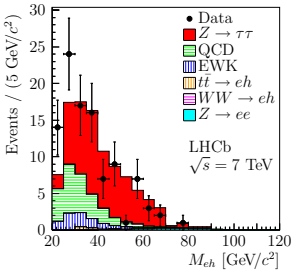

(e) $Z \to \tau^+\tau^-$ candidates with one τ decaying as $\tau \to e\bar{\nu}_e\nu_\tau$ and the other as $\tau \to h\nu_\tau$

Figure 2.1: Invariant mass distributions for $Z \to \tau^+\tau^-$ candidates [79].

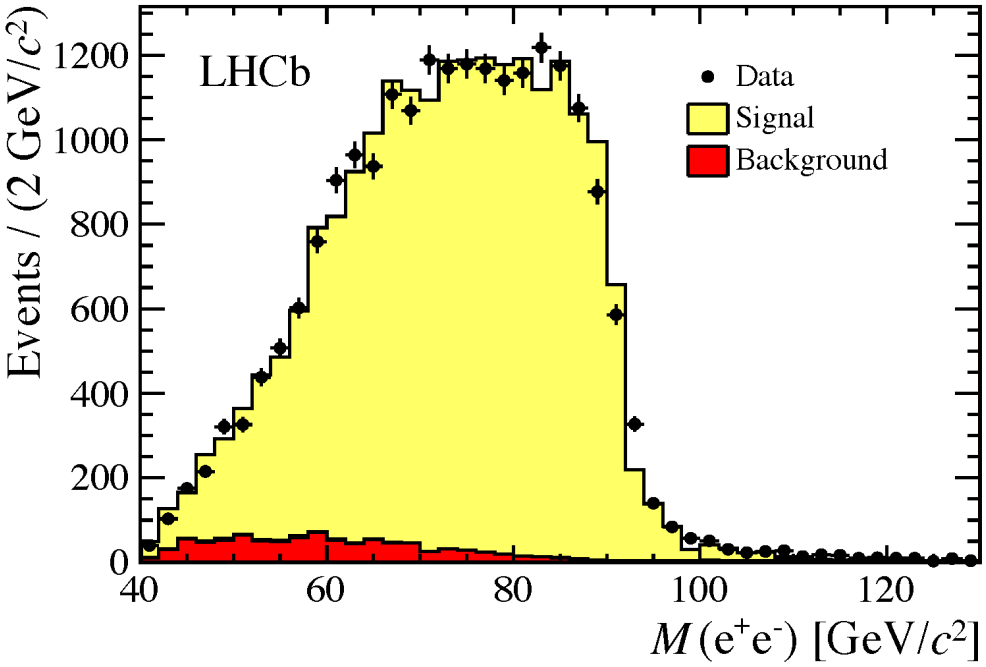

Figure 2.2: Invariant mass distribution for Z $\rightarrow e^+e^-$ [55].

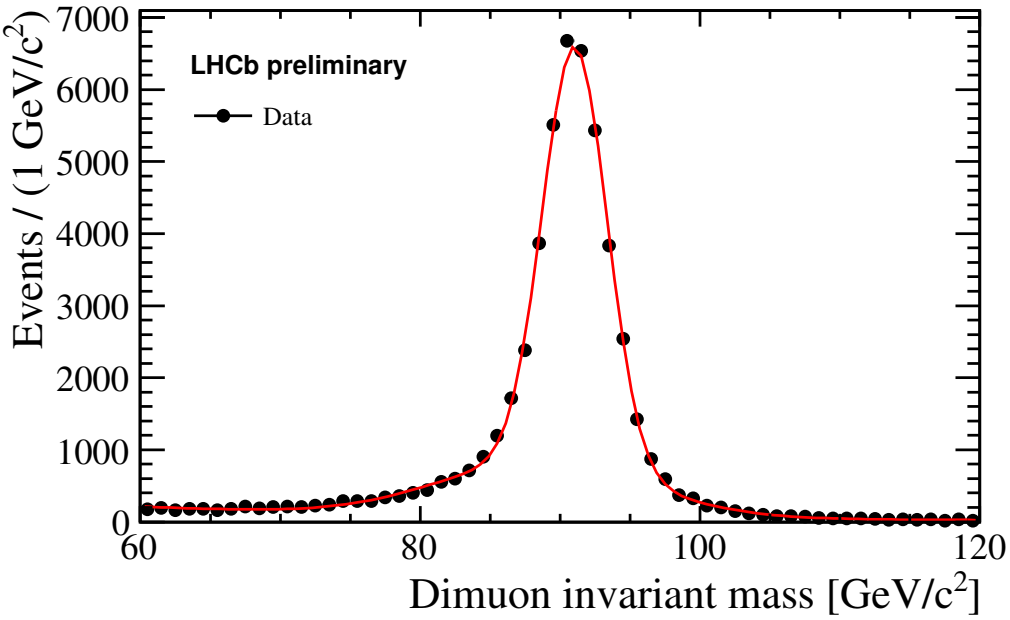

Figure 2.3: Invariant mass distribution for Z $\rightarrow \mu^+\mu^-$ [69, 70].

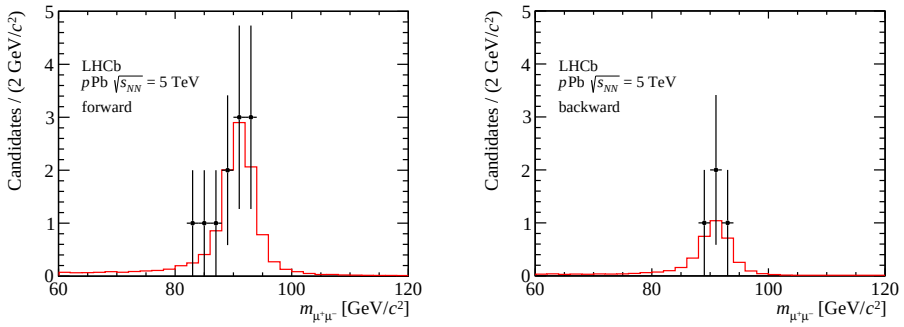

Figure 2.4: Invariant mass distribution for Z $\to\mu^+\mu^-$ [64] in proton lead collisions.

The transverse momentum (p_T) distribution of the Z bosons is shown in Figure 2.7 where it is compared to several theoretical precisions. This quantity is sensitive to higher order corrections in pertubative QCD. The lowest bin is of special interest. At leading order the Z can only carry negligible p_T. Every additional transversal QCD radiation must recoil against the Z boson leading to a nonzero transverse momentum of the Z itself. This explains the large difference in the predictions. The NNLO prediction from FEWZ does not include these soft effects and thus doesn't describe the data. The NLO prediction from PowHEG is corrected for some of these effects from the parton shower implemented in PYTHIA and leads to a better description. The prediction from RESBOS is the only one that yields a satisfactory description of this challenging variable.

2.2 Cross Section Measurement of Z $\to \mu^+\mu^-$

The cross section is determined from the formula [81]:

$$\sigma = \frac{\rho f_{\mathrm{FSR}} f_{\mathrm{MGR}}}{\mathcal{A}\int \mathcal{L}} \sum_{\mathrm{Events}} \frac{1}{\varepsilon(\eta_{\mu^+}, \eta_{\mu^-}, n_{\mathrm{PV}})} \tag{2.1}$$

This equation is the one used for [70] which is similar to the formulas used in this work. The variables are the acceptance $\mathcal{A}$ which accounts for not instrumented regions within the fiducial volume; the integrated luminosity $\int \mathcal{L}$; the efficiencies for each event for trigger, reconstruction and identification $\varepsilon(\eta_{\mu^+}, \eta_{\mu^-}, n_{\mathrm{PV}})$; the purity ρ and correction factors for bin to bin migration f_{MGR} and final state radiation f_{FSR}.

I the following I will explain how some of these numbers are calculated.

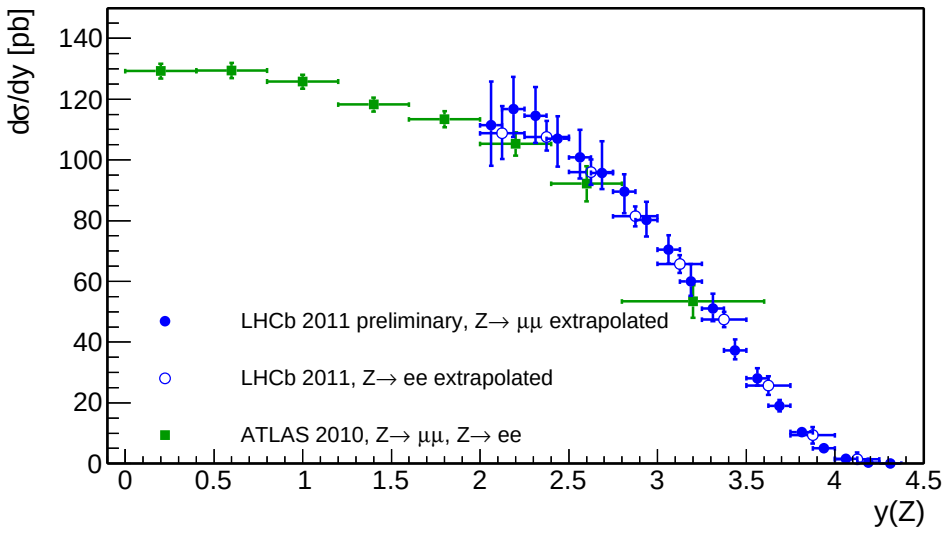

Figure 2.5: Comparison of the extrapolated LHCb measurement to Atlas [70].

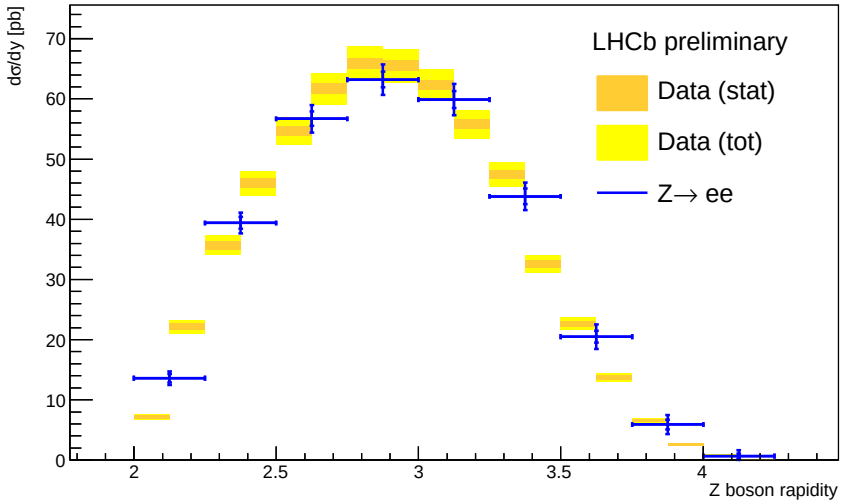

Figure 2.6: Z production cross section as a function of Z rapidity in Z $\to e^+e^-$ and Z $\to \mu^+\mu^-$ at 7 TeV.

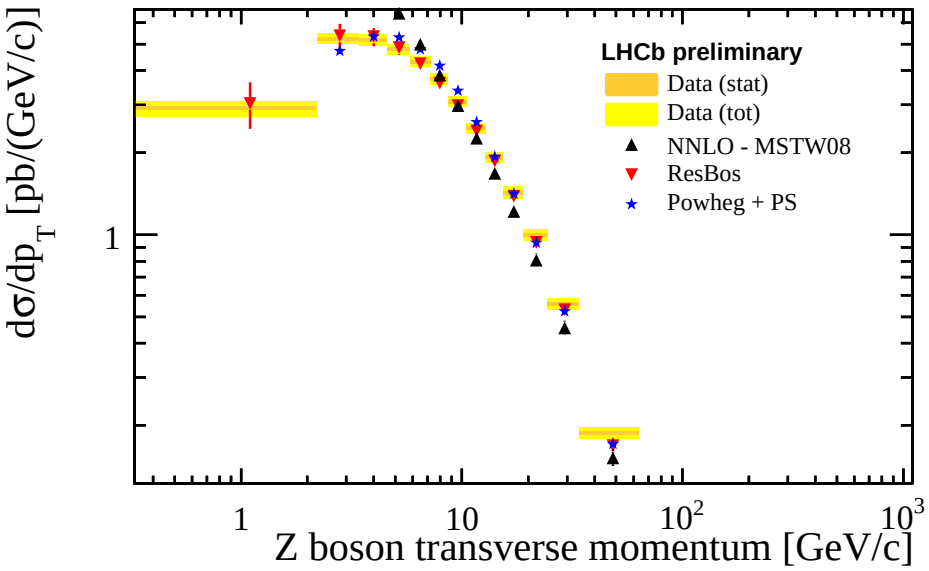

Figure 2.7: Z production cross section as a function of Z transverse momentum.

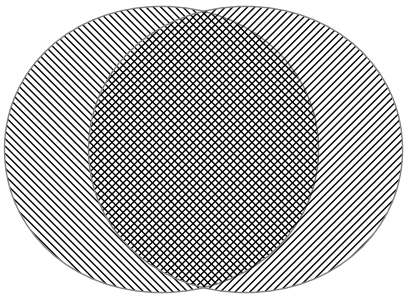

Figure 2.8: Illustration of the concept behind the Tag and Probe method.

2.3 Tag and Probe Method

The Tag and Probe method is a data driven technique to study the reconstruction of objects in the detector. The objects considered in this thesis are tracks, and muon ID objects and the combination of those in the trigger stage caused by high momentum muons from Z decays. One well reconstructed and identified muon is combined with a partially reconstructed respectively identified object to a $Z \rightarrow \mu^+\mu^-$ candidate. For the method to work a good background rejection is needed. It must be a valid to conclude from the presence of the probe to the presence of an object in the detector. In the applications presented in this work the background rejection relies heavily on the resolution of the tracking system. This is done using as little information as possible in the partially reconstructed objects from the systems to be probed. Therefore the well reconstructed and identified muon is required to have fired the trigger and to satisfy the stripping conditions. The analysis described in the following is documented in [1] superseeds earlier measurements of the efficiencies e.g. [5, 82].

The concept becomes clearer in a less abstract context when it is applied to the trigger efficiency.

2.4 Trigger Efficiency

The LHCb trigger system records the candidates that were used in a given trigger decision. Thus it is possible to understand what has caused a given

trigger decision and especially it's possible to say whether a given offline muon candidate was sufficient for the trigger system to accept this event. If this is the case the muon is called "triggered on signal" (TOS)

In order to measure the efficiency for positive muons one can now select $Z \rightarrow \mu^+\mu^-$ candidates. In the graphical representation this corresponds to the total hatched area in Figure 2.8. Now it is additionally required that the negative muon is TOS. This corresponds then to the the fallingly hatched area. In the lingo of the method the offline Z candidate that is TOS on the negative muon is the tag, and the property of being TOS for the positive muon is the probe. It is assumed that triggers for positive and negative muons are independent. Graphically that means the fallingly hatched area is an unbiased sample of the total area. With this assumption the TOS efficiency for positive muons can be measured as the doubly hatched area over the fallingly hatched area:

$$\varepsilon_{\mu^+,\mathrm{TOS}} = \frac{n_{\mu^+,TOS \wedge \mu^-,TOS}}{n_{\mu^-,TOS}} \tag{2.2}$$

analogously the efficiencies for negative muons can be obtained.

A consistent way to calculate the efficiency for both species can be obtained in the following way from the (inclusive) single to double TOS ratio γ:

$$\gamma = \frac{n_{\mathrm{double}}}{n_{\mathrm{single}}} = \frac{\varepsilon^2}{2\varepsilon - \varepsilon^2} \tag{2.3}$$

$$\varepsilon = \frac{2\gamma}{1+\gamma} \tag{2.4}$$

2.5 Global Event Cuts

For the global event cuts the Tag and Probe method can not be applied. Only if the μ^+ passes the GEC the μ^- does as well and vice versa so the the requirements of that method are not fulfilled.

The global event cut efficiency can be calculated from a fit to the SPD multiplicity distribution n_{SPD}. The used fit model is a gamma distribution which has the following PDF.

$$f(x,k,\theta) = \frac{x^{k-1}e^{-\frac{x}{\theta}}}{\theta^k \Gamma(k)} \tag{2.5}$$

The normalisation factor θ^k in the nominator is absorbed in the overall normalisation in the the actual fit leading to a normalisation factor that doesn't represent the number of events. The numbers used in the efficiency calculation are determined from the integral which does have this interpretation.

The efficiency is then given by:

$$\varepsilon = \frac{\int_0^{n_{\text{Cutoff}}} f(n,k,\theta)}{\int_0^{\infty} f(n,k,\theta)} \tag{2.6}$$

$$= 1 - \frac{\int_{n_{\text{Cutoff}}}^{\infty} f(n,k,\theta)}{\int_0^{\infty} f(n,k,\theta)} \tag{2.7}$$

The value for n_{Cutoff} was set in the hardware trigger (L0DU) and corresponds to 600 hits for the configuration number (L0TCK) 0x0046 used for the data proton proton data at $\sqrt{s} = 2.56\,\text{TeV}$ taken in 2013. Those are the data the numbers in this section correspond to. The uncertainty is then propagated the following way:

$$\sigma_\varepsilon = \frac{\sigma_{\text{tail}}}{n_{\text{total}}} \oplus \frac{n_{\text{tail}}\sigma_{\text{total}}}{n_{\text{total}}^2} \tag{2.8}$$

The fit results are shown in Table 2.1 and Figure 2.9 on data taken at $\sqrt{s} = 2.76\,\text{TeV}$ in 2013 with loosened selection criteria[1]. The calculated inefficiency is $1 - \varepsilon = 3 \times 10^{-7} \pm 2.6 \times 10^{-6}$.

This dataset is not representative for the large proton proton datasets taken in 2011 and 2012 where the pileup was higher and thus the GEC efficiency is lower. For those datasets it in the 90% regime.

[1] No requirement on the pseudorapidity of the muons and triggered by the dimuon triggers that use a looser GEC of $n_{\text{SPD}} < 900$

Parameter	value		
normalisation	519.872	±	117.801
k	5.135 27	±	2.485 24
θ	0.041 787 5	±	0.024 375
n_{total}	25.9936	±	5.890 04
n_{tail}	$8.262\,47 \times 10^{-06}$	±	$6.796\,93 \times 10^{-05}$

Table 2.1: Fit result for the fit shown in Figure 2.9.

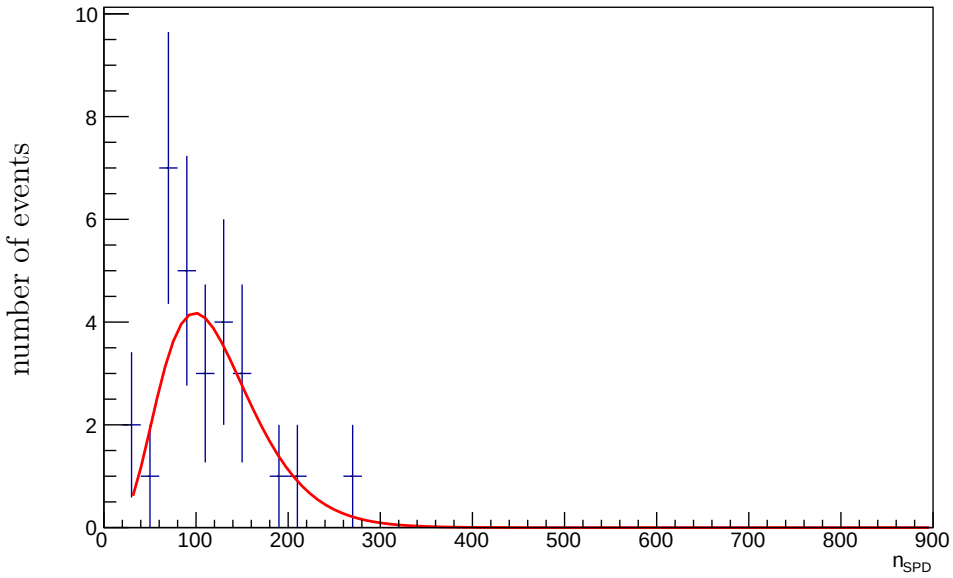

Figure 2.9: Fit of the n_{SPD} distribution of Z $\to\mu^+\mu^-$ events in the proton proton data taken in 2013 at $\sqrt{s} = 2.56$ TeV.

2.6 Tracking Efficiency

The tracking efficiency is the most evolved quantity to calculate. Again the Tag and Probe method is used. The main complication in the method is that a tag has to be found. Since most of the information we have about the Z candidate originates for the tracks this is difficult to do without a bias. The approach chosen was first used in [5] and relies on tracks fit solely from hits in the muons system. For these tracks it's assumed they originate from the primary vertex. Then a search window is opened to search for compatible hits in the TT station. If such hits are found, the whole object is fit as a μ TT track. This is not very efficient and also leads to a low resolution. Nevertheless it allows to select muon candidates without relying on the long track with small bias [5] which is what is needed for Tag and Probe.

The major problem when it comes to the estimate of the efficiency is the background. This is due to the underlying assumption that if there is a probe there has been a true muon in the detector which may or may not be reconstructed. If the μ TT track does not correspond to an true muon (i.e. it is what is called a ghost track) then there should not be a long track either. Still the Tag and Probe method will look for that track and assume that there was a true muon and the detector together with the tracking algorithm failed to find it. Since the momentum resolution of the μ TT track is much worse than on the ordinary long tracks the mass window on the Z resonance loses discriminative power against the background. The μ TT tracks are reconstructed using the muon systems with all its iron hadron filters which gives some discrimination against hadrons but it does not help against decay-in-flight background. $K \rightarrow \mu^{\pm}$ X and $\pi \rightarrow \mu^{\pm}\overline{\nu}_{\mu}$ decays produce true muons that can be reconstructed and both the initial K or π as well as the muon can cause hits in the TT stations. Since this does not correspond to the hypothesis of the track fit that there is one particle flying through the detector it may also be reconstructed far away from the momentum of that particle and pass the high momentum requirements on the probe. The problem is amplified at high η since the signal cross section drops at high y as it can e.g. seen from Figure 2.6.

A way to check this is to look at the matched track, combine that with the good muon and see whether it peaks at the Z mass. This is biased since it can only be done if there is a matching track and thus can only find background but can not rule out its presence. In other words it can identify bad selection criteria but can't prove good criteria.

In October 2012 there were numerous criteria used mainly by groups in Dublin and in Zurich. The criteria are summarised in Table 2.2. In Figure 2.10 the matched track method is applied. The blue band is a measure

of the ratio of matched tracks and thus the measured tracking inefficieny. In Figure 2.11 the measured efficiency is shown as a function of the Z invariant mass. The true tracking efficiency is not expected to depend on this quantity but the larger background fraction away from the Z mass peak causes a bias towards low efficiency values. If the measured efficiency falls off dramatically away from the Z pole the criteria other than the mass are not sufficient to suppress the background.

Track Matching

In the previous section it was mentioned that a μ TT track is matched to a long track. What does that mean and imply?

A long track is considered to matched to an μ TT track if it shares a certain number of hits. Based on this there were two criteria used. One criterion (D) asks for 40% of the muon hits to be shared the, other (Z) asks for 70% overlap in the muon system and if the long track has TT hits assigned it also asks for half of these hits to be shared.

The matching comes with an inefficieny where a long track from the Z decay may be not matched to the μ TT track. In order to get a precision measurement of the tracking efficiency the matching efficiency has to be taken into account.

The matching efficiency is measured the "the other way around". In Z events selected with the standard selection μ TT tracks are reconstructed. Those tracks are assigned to reconstructed muons by a criterion based on Δ_R. Then the matching efficiency is calculated by another Tag and Probe with the long - μ TT track pair in a Z event being the probe and the matching criterion the tag. The efficiencies are measured to be $98.82^{+0.11}_{-0.12}\%$ for criterion Z and $99.45^{+0.08}_{-0.09}\%$ for criterion D. The uncertainties are the 68% confidence intervals (Clopper-Pearson) [83]. The distributions for the overlap variable in the muon system and in the TT station are shown in Figure 2.12.

Low Momentum Matches

There are also events where the μ TT track is matched to a low energy track. In Figure 2.13 the (η, p_T) distributions are shown. Even though the selection criteria required the μ TT track to have $p_T > 20\,\text{GeV}$ there are numerous matched long tracks with low momentum. Also the selection cuts in (η, p_T) are not preserved in the matched tracks. This reflects the low resolution of the μ TT tracks. Still the sample is dominated by Z decays and the Jacobean peak at $m_Z/2$ is clearly visible. Nevertheless the matched tracks must be required to carry a minimal p_T of 10 GeV.

A	J	S	P
$\|\Delta\phi_{\mu,\mu\mathrm{TT}}\| > .1$	$\|\Delta\phi_{\mu,\mu\mathrm{TT}}\| > .64$	$\|\Delta\phi_{\mu,\mu\mathrm{TT}}\| > 1$	–
$70 < m_{\mathrm{Z}} < 110\,\mathrm{GeV}$		$60 < m_{\mathrm{Z}} < 120\,\mathrm{GeV}$	
$\chi^2_{\mathrm{Vertex}} < 100$	$\chi^2_{\mathrm{Vertex}} < 5$		
–	$2 < \eta_{\mu\ \mathrm{TT}} < 4.5$		
$p_{T,\mu\ TT} > 20\,\mathrm{GeV}$			

Table 2.2: Overview over the selection criteria in use in the EW group of LHCb in 2012.

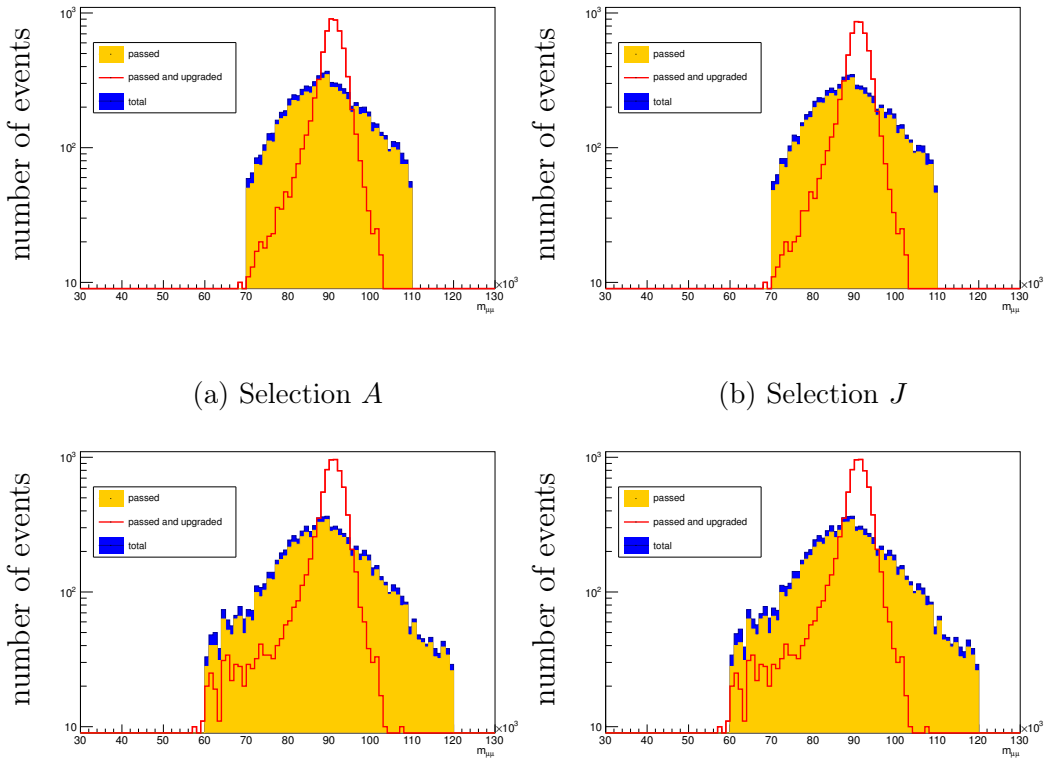

(a) Selection A

(b) Selection J

(c) Selection S

(d) Selection P

Figure 2.10: Invariant mass distribution of the tag long track and the μ TT track pair overlayed with the matched long track if there is a matched track.

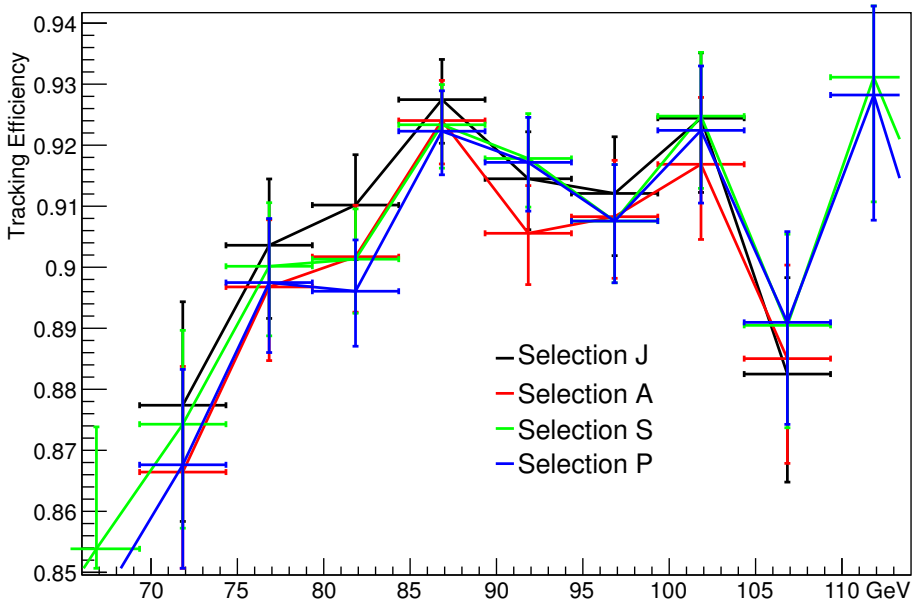

Figure 2.11: Measured efficiencies as function of invariant mass. Any dependence on this variable suggests background contamination.

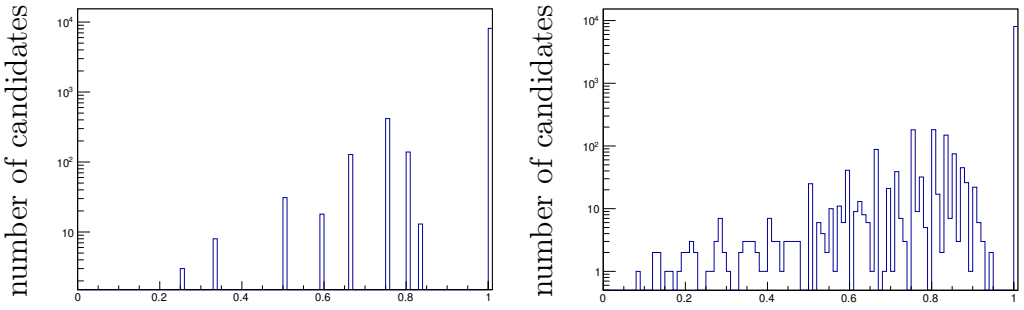

(a) Overlap in TT station.

(b) Overlap in muon system.

Figure 2.12: Distribution of overlap variables. The spikes arise from the limited number of measurements per track. Both are ratios of small integer numbers. Please note the log scale and the spike at unity.

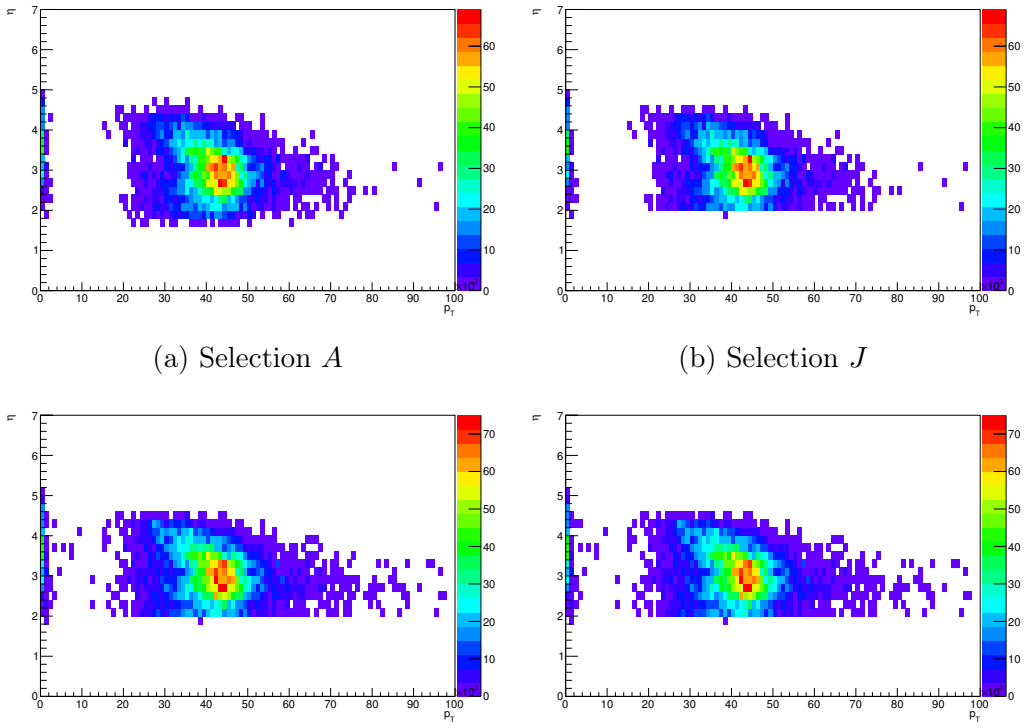

(a) Selection A

(b) Selection J

(c) Selection S

(d) Selection P

Figure 2.13: Distribution of the matched long tracks. The upper row uses criterion Z while the lower uses D.

2.7 Muon Identification Efficiency

The muon identification efficiency can be calculated using the Tag and Probe method. The Z candidate is then built from a well reconstructed and identified muon together with a long track. Additional criteria usually include vertex $\chi^2 < 5$ and PIDμ >0 on the tag muon. This usually leads to a very pure sample. The efficiency for ISMUON is in the 98% regime for muons with $p_T > 10\,\text{GeV}$ and $2 < \eta < 4.5$. The criterion was loosened between Reco 12 and Reco 14 which leads to higher efficiency and lower purity.

2.8 Efficiency Correction

Each event gets an efficiency assigned that is calculated according to the following formula:

$$\begin{aligned} \varepsilon = & \quad (\quad \varepsilon_{\text{trigger}}(\eta_{\mu^+}) \quad \vee \quad \varepsilon_{\text{trigger}}(\eta_{\mu^-}) \quad) \\ \wedge & \quad (\quad \varepsilon_{\text{tracking}}(\eta_{\mu^+}) \quad \wedge \quad \varepsilon_{\text{tracking}}(\eta_{\mu^-}) \quad) \\ \wedge & \quad (\quad \varepsilon_{\text{ID}}(\eta_{\mu^+}) \quad \wedge \quad \varepsilon_{\text{ID}}(\eta_{\mu^-}) \quad) \end{aligned} \tag{2.9}$$

with the logical operators defined as:

$$\varepsilon_1 \wedge \varepsilon_2 = \varepsilon_1 \varepsilon_2 \tag{2.10}$$

$$\varepsilon_1 \vee \varepsilon_2 = \varepsilon_1 + \varepsilon_2 - \varepsilon_1 \varepsilon_2 \tag{2.11}$$

This corresponds to the propagation of probabilities for the or and the and operation in the statistically independent case. The stepwise functions $\varepsilon(\eta_\mu)$ are stored in `TGraph` objects. To propagate the uncertainties the `TGraph` objects are varied within their uncertainties. The probability density function (PDF) is discussed in the following section. From the resulting PDF pseudo experiments can be generated that allow to determine the spread of the results due to the imperfect knowledge of the efficiencies. That is done in a way to ensure that each efficiency is only sampled once per pseudo experiment and therefore affects the result of the pseudo experiment in a way that naturally takes into account the correlations induced by the calculations.

2.8.1 Probability Distribution for the Tag and Probe Estimator of the Efficiency

Let $\hat{\epsilon}$ be the estimator for the true efficiency ε for a process. If the efficiency is determined in a Tag and Probe method using n tags, the estimator is given by:

$$\hat{\varepsilon} = k/n \tag{2.12}$$

where k is the number of tags where the probe was found. The probability mass function (PMF) is given by the binomial distribution:

$$P(\hat{\varepsilon}) = P_{\text{Binomial}}(\varepsilon, k, n) \tag{2.13}$$

$$= \binom{n}{k} \varepsilon^k (1-\varepsilon)^{n-k} \tag{2.14}$$

where k has to satisfy the condition

$$k = \hat{\varepsilon} n. \tag{2.15}$$

The estimated efficiencies are not entirely based on Tag and Probe but are corrected for other effects. For example there is a correction the tracking efficiency accounting for tracks being reconstructed but not matched to the μ-TT track. In those cases the beta distribution is used. The beta distribution is defined as:

$$P_{\text{Beta}}(\varepsilon, \alpha, \beta) = \frac{\varepsilon^{\alpha-1}(1-\varepsilon)^{\beta-1}}{B(\alpha, \beta)} \tag{2.16}$$

with the Beta function B defined in terms of the Γ function as:

$$B(x, y) = \frac{\Gamma(x)\Gamma(y)}{\Gamma(x+y)} \qquad \text{8.384(1) in [84]} \tag{2.17}$$

$$\Gamma(z) = \int_0^\infty t^{z-1} e^{-t}\, \mathrm{d}t \qquad \text{8.310(1) in [84]} \tag{2.18}$$

The beta distribution can be seen as the continuous generalisation of the binomial distribution. If the parameters (α, β) are chosen to be

$$\alpha = k + 1 \tag{2.19}$$

$$\beta = n - k + 1 \tag{2.20}$$

then the probability P is given by:

$$\begin{aligned}
P_{\text{Beta}}(\varepsilon, \alpha, \beta) &= P_{\text{Beta}}(\varepsilon, k+1, n-k+1) \\
&= \frac{\varepsilon^k (1-\varepsilon)^{n-k}}{B(k+1, n-k+1)} \\
&= \frac{\varepsilon^k (1-\varepsilon)^{n-k} \Gamma(n+2)}{\Gamma(k+1)\Gamma(n-k+1)} && \text{using 8.384(1) in [84]} \\
&= \frac{\varepsilon^k (1-\varepsilon)^{n-k} (n+1)!}{k!(n-k)!} && \text{using 8.339(1) in [84]} \\
&= \binom{n}{k} \varepsilon^k (1-\varepsilon)^{n-k} (n+1) \\
&= (n+1) P_{\text{Binomial}}(\varepsilon, k, n)
\end{aligned} \tag{2.21}$$

In case corrections are applied to n or k Equations 2.19 and 2.20 can be used to obtain a continuation of the binomial distribution for real n or k.

At this point it needs to be stressed, that the binomial distribution is a discrete distribution while the beta distribution is continuous. It was just evaluated at discrete points. Therefore a factor of $\mathcal{O}(n)$ is expected when a

PDF is interpreted as a PMF. This can be understood from the MC integration technique:

$$1 = \int_0^1 P_{\text{Beta}}(\varepsilon, \alpha, \beta)\,\mathrm{d}\,\varepsilon = \lim_{n\to\infty} \frac{1}{n} \sum_{i=1}^{n} P_{\text{Beta}}(\varepsilon_i, \alpha, \beta) \tag{2.22}$$

where the $\varepsilon_i \in [0, 1]$ are randomly sampled from a uniform distribution. The parameters of the beta distribution are calculated from Equations 2.19 and 2.20 if the original efficiency was determined with a pure Tag and Probe method. If there are corrections applied, (α, β) are calculated with a numerical algorithm that is designed to satisfy the following conditions:

$$P_{\text{Beta}}(\varepsilon - \sigma_{\varepsilon,\text{low}}, \alpha, \beta) = P_{\text{Beta}}(\varepsilon + \sigma_{\varepsilon,\text{high}}, \alpha, \beta) \tag{2.23}$$

$$68\% = \int_{\varepsilon-\sigma_{\varepsilon,\text{low}}}^{\varepsilon+\sigma_{\varepsilon,\text{high}}} P_{\text{Beta}}(\varepsilon, \alpha, \beta)\,\mathrm{d}\,\varepsilon. \tag{2.24}$$

The criterion is a mathematical formulation that the 1σ confidence interval has to agree between the calculated beta distribution and the calculated value. Wherever 68% is mentioned in this section it is actually the 1σ confidence interval calculated from the Gaussian error function.

The starting value for the optimisation is chosen to match Equation 2.24 and uses the expression for the mode(m) of the beta distribution which is at this stage required to be in the centre of the confidence interval:

$$m = \frac{\alpha - 1}{\alpha + \beta - 2} \tag{2.25}$$

$$\beta = (1/m - 1)\alpha + (2 - 1/m) \tag{2.26}$$

The formula for the mode can be derived as follows: Sufficient condition for the maximum in ε of $P_{\text{Beta}}(\varepsilon, \alpha, \beta)$ to be at the point m:

$$\frac{\partial P_{\text{Beta}}(\varepsilon, \alpha, \beta)}{\partial \varepsilon}|_{\varepsilon=m} = 0 \tag{2.27}$$

$$\frac{\partial^2 P_{\text{Beta}}(\varepsilon, \alpha, \beta)}{\partial \varepsilon^2}|_{\varepsilon=m} < 0 \tag{2.28}$$

The derivatives are:

$$\frac{\partial P_{\text{Beta}}(\varepsilon, \alpha, \beta)}{\partial \varepsilon} = \left(\frac{\alpha - 1}{\varepsilon} - \frac{\beta - 1}{1 - \varepsilon}\right) P_{\text{Beta}}(\varepsilon, \alpha, \beta) \tag{2.29}$$

$$\frac{\partial^2 P_{\text{Beta}}(\varepsilon, \alpha, \beta)}{\partial \varepsilon^2} = \left(\left(\frac{\alpha - 1}{\varepsilon} - \frac{\beta - 1}{1 - \varepsilon}\right)^2 - \frac{\alpha - 1}{\varepsilon^2} - \frac{\beta - 1}{(1 - \varepsilon)^2}\right) P_{\text{Beta}}(\varepsilon, \alpha, \beta) \tag{2.30}$$

From Equation 2.29 it can be easily derived that there cannot be a maximum unless Equation 2.25 holds. Inserting Equation 2.25 into Equation 2.30 yields:

$$\begin{aligned}
\frac{\partial^2 P_{\text{Beta}}(\varepsilon,\alpha,\beta)}{\partial\varepsilon^2}\Big|_{\varepsilon=m} &= \left(\left(\frac{\alpha-1}{\varepsilon}-\frac{\beta-1}{1-\varepsilon}\right)^2-\frac{\alpha-1}{\varepsilon^2}-\frac{\beta-1}{(1-\varepsilon)^2}\right)\\
&\times P_{\text{Beta}}(\varepsilon,\alpha,\beta)\\
&= \left(0^2-\frac{(\alpha-1)(\alpha+\beta-2)^2}{(\alpha-1)^2}+\frac{(\alpha+\beta-2)^2(\beta-1)}{(\beta-1)^2}\right)\\
&\times P_{\text{Beta}}(\varepsilon,\alpha,\beta)\\
&= \left(-\frac{(\alpha+\beta-2)^2}{\alpha-1}-\frac{(\alpha+\beta-2)^2}{\beta-1}\right)P_{\text{Beta}}(\varepsilon,\alpha,\beta)\\
&= \left(-\frac{(\alpha+\beta-2)^2\left((\beta-1)+(\alpha-1)\right)}{(\alpha-1)(\beta-1)}\right)P_{\text{Beta}}(\varepsilon,\alpha,\beta)\\
&= \left(-\frac{(\alpha+\beta-2)^2\left((\beta+\alpha-2)\right)}{(\alpha-1)(\beta-1)}\right)P_{\text{Beta}}(\varepsilon,\alpha,\beta) \quad (2.31)
\end{aligned}$$

using

$$\begin{aligned}
1-m &= 1-\frac{\alpha-1}{\alpha+\beta-2}\\
&= \frac{\alpha+\beta-2-\alpha+1}{\alpha+\beta-2}\\
&= \frac{\beta-1}{\alpha+\beta-2}. \quad (2.32)
\end{aligned}$$

Equation 2.31 shows that $\frac{\partial^2 P}{\partial\varepsilon^2}$ is negative if $\alpha > 1$ and $\beta > 1$ which is the case if $n > k$ and $k \neq 0$.

The expression for the mode allows α to be scanned one dimensionally to satisfy Equation 2.24 with β continuously adjusted according to Equation 2.26. The integral can be expressed, using the regularised incomplete beta function I_x which is defined to be primitive integral of the Beta distribution

$$I_x(p,q) = \frac{B_x(p,q)}{B(p,q)} \qquad 8.392 \text{ in } [84] \qquad (2.33)$$

$$B_x(p,q) = \int_0^x t^{p-1}(1-t)^{q-1} \qquad 8.391 \text{ in } [84] \qquad (2.34)$$

as

$$\int_{\varepsilon_{\text{low}}}^{\varepsilon_{\text{high}}} P_{\text{Beta}}(\varepsilon,\alpha,\beta)\,\mathrm{d}\,\varepsilon = I_{\varepsilon_{\text{high}}}(\alpha,\beta) - I_{\varepsilon_{\text{low}}}(\alpha,\beta). \qquad (2.35)$$

This procedure results in a starting value that satisfies Equation 2.24 in a reasonable approximation. However, convergence to a good precision for Equation 2.24 with the current algorithm is much slower than it is for Equation 2.23. From this a χ^2 optimisation is started. Equations 2.23 and 2.24 are expressed as χ^2 and the following algorithm is used:

1. Follow the gradient of $P_{\text{Beta}}(\varepsilon, \alpha, \beta)$ in α and β at one edge until the χ^2 worsens.

2. If the integral in Equation 2.24 is larger than 68% the chosen edge has to be lowered otherwise it has to be increased.

3. If the integral has to be increased, increase the edge with the lower $P_{\text{Beta}}(\varepsilon, \alpha, \beta)$ otherwise lower the edge with the higher $P_{\text{Beta}}(\varepsilon, \alpha, \beta)$.

This algorithm converges fast to a solution that obeys Equation 2.23. Unfortunately the convergence in terms of Equation 2.24 is very slow. Therefore an additional step is applied until a satisfactory result is found. If the algorithm arrives at a stage where Equation 2.23 is fulfilled to high precision but Equation 2.24 is not α and β are increased or lowered simultaneously depending on whether the integral has to be lowered or increased. When this is done the mode as calculated from Equation 2.25 is required to remain in the confidence interval. Than the previous optimisation for Equation 2.23 is used again. This algorithm can be used to obtain a $\chi^2 < 10^{-6}$ but with the confidence internals used $\chi^2 < 10^{-10}$ could not be achieved. The gradient can be calculated analytically as follows. The calculation is split into numerator $N(\alpha, \beta, \varepsilon)$ and denominator $B(\alpha, \beta)$.

$$
\begin{aligned}
\frac{\partial B(\alpha,\beta)}{\partial \alpha} &= \frac{\partial}{\partial \alpha}\frac{\Gamma(\alpha)\Gamma(\beta)}{\Gamma(\alpha+\beta)} && \text{8.384(1) in [84]} \\
&= \frac{\frac{\partial \Gamma(\alpha)}{\partial \alpha}\Gamma(\beta)\Gamma(\alpha+\beta) - \Gamma(\alpha)\Gamma(\beta)\frac{\partial \Gamma(\alpha+\beta)}{\partial \alpha}}{\Gamma^2(\alpha+\beta)} \\
&= \frac{\frac{\partial \Gamma(\alpha)}{\partial \alpha}\Gamma(\beta)\Gamma(\alpha+\beta)}{\Gamma^2(\alpha+\beta)} - \frac{\Gamma(\alpha)\Gamma(\beta)\frac{\partial \Gamma(\alpha+\beta)}{\partial \alpha}}{\Gamma^2(\alpha+\beta)} \\
&= \frac{\Gamma(\alpha)\frac{\partial \Gamma(\alpha)}{\partial \alpha}\Gamma(\beta)}{\Gamma(\alpha)\Gamma(\alpha+\beta)} - \frac{\Gamma(\alpha)\Gamma(\beta)\psi(\alpha+\beta)}{\Gamma(\alpha+\beta)} && \text{8.361(1) in [84]} \\
&= \frac{\Gamma(\alpha)\psi(\alpha)\Gamma(\beta)}{\Gamma(\alpha+\beta)} - B(\alpha,\beta)\psi(\alpha+\beta) && \text{8.384(1) in [84]} \\
&= B(\alpha,\beta)\left(\psi(\alpha) - \psi(\alpha+\beta)\right) && \text{8.384(1) in [84]}
\end{aligned}
\tag{2.36}
$$

using the digamma function $\psi(x)$ defined as:

$$\psi(x) = \frac{\mathrm{d}}{\mathrm{d}\,x}\ln\left(\Gamma(x)\right) \qquad 8.361(1) \text{ in } [84] \tag{2.37}$$

$$= \frac{\Gamma'(x)}{\Gamma(x)}. \tag{2.38}$$

For the numerator the calculation is:

$$\begin{aligned}\frac{\partial N(\alpha,\beta,\varepsilon)}{\partial\alpha} &= \frac{\partial}{\partial\alpha}\varepsilon^{\alpha-1}(1-\varepsilon)^{\beta-1}\\ &= \frac{\partial}{\partial\alpha}e^{\ln(\varepsilon)(\alpha-1)}(1-\varepsilon)^{\beta-1}\\ &= \ln(\varepsilon)e^{\ln(\varepsilon)(\alpha-1)}(1-\varepsilon)^{\beta-1}\\ &= \ln(\varepsilon)N(\alpha,\beta,\varepsilon)\end{aligned} \tag{2.39}$$

and a analogous calculation yields:

$$\frac{\partial N(\alpha,\beta,\varepsilon)}{\partial\beta} = \ln(1-\varepsilon)N(\alpha,\beta,\varepsilon) \tag{2.40}$$

This leads to the gradient of $P_{\mathrm{Beta}}(\varepsilon,\alpha,\beta)$

$$\begin{aligned}\frac{\partial P_{\mathrm{Beta}}(\varepsilon,\alpha,\beta)}{\partial\alpha} &= \frac{\ln(\varepsilon)N(\alpha,\beta,\varepsilon)B(\alpha,\beta) - N(\alpha,\beta,\varepsilon)B(\alpha,\beta)\left(\psi(\alpha)-\psi(\alpha+\beta)\right)}{B^2(\alpha,\beta)}\\ &= \frac{N(\alpha,\beta,\varepsilon)\left(\ln(\varepsilon)-\psi(\alpha)+\psi(\alpha+\beta)\right)}{B(\alpha,\beta)}\\ &= P_{\mathrm{Beta}}(\varepsilon,\alpha,\beta)\left(\psi(\alpha+\beta)-\psi(\alpha)+\ln(\varepsilon)\right)\\ \frac{\partial P_{\mathrm{Beta}}(\varepsilon,\alpha,\beta)}{\partial\beta} &= P_{\mathrm{Beta}}(\varepsilon,\alpha,\beta)\left(\psi(\alpha+\beta)-\psi(\beta)+\ln(1-\varepsilon)\right)\end{aligned} \tag{2.41}$$

All special functions are evaluated using the routines provided in the Gnu Scientific Library (`GSL`) package and the algorithm was added to the LHCb software as the newly created package `Phys/EWHighPTMuonEff`.

Chapter 3

Studies of the associated Production of Z Bosons with Jets at $\sqrt{s} = 7$ TeV and the Jet Reconstruction in LHCb

In this chapter a collection of studies related to jet reconstruction are presented. After the first established signals of jets measured with the LHCb detector, the effort to reconstruct jets in LHCb increased and lead to the publication of a cross section measurement of the associated production of Z bosons and jets. Even though I contributed significantly to this measurement and I am a proponent of the paper [77] the paper and the corresponding analysis note was written by William James Barter. It was the first published result using jets from the LHCb collaboration.

3.1 Established Signal

All plots in this section are created using LHCb data. These plots did not undergo the LHCb review. The rules of the collaboration make all results in the following sections classified as "LHCb unofficial". The results in Section 3.5 are official LHCb results that did undergo the full review.

3.1.1 Early Jet Definition and Z Candidate Definition

The jet reconstruction starts from the reconstructed tracks with the pion mass hypothesis assigned. Additionally neutral ECAL clusters without matching track are added[1]. The track selection is:

- $p_T > 200\,\text{MeV}$ corresponding to the acceptance of the tracking algorithm.
- $\frac{\sigma_p}{\|p\|} < 10\%$ rejects tracks which are compatible with a straight line and thus zero curvature and infinite momentum.

Those particles are clustered with an anti-k_T jet algorithm with an R parameter of one half. The jets are required to satisfy:

- $p_T > 5\,\text{GeV}$.
- At least three particles in the jet.
- The largest transverse momentum of a single particle has to be less than 90% of the jets p_T.

This is compared to simulated events from Pythia on detector level. The comparison can be found in Figures 3.1 to 3.3 where all distributions are normalised to unity. The measurement is performed on the $36\,\text{pb}^{-1}$ dataset taken in 2010. For all the variables a reasonable agreement from data and simulation are observed. The most striking evidence for a signal for associated production of Z bosons with jets originates from the correlations between jets and Z boson. In Figure 3.4 the distributions of the difference in polar angle are shown. This distribution shows a strong enhancement at $\pm\pi$ which means the Z and the jet fly apart back to back. The same can be seen in the Δ_R distribution in Figure 3.6. In Figure 3.5 the Δ_{p_T} distribution is presented. From this distribution it can be seen that not only the direction in the transverse plane matches but also the magnitude of the momentum. It is expected that the jet multiplicity falls rapidly and the selected events

[1] From the `StdLoosePhotons` container.

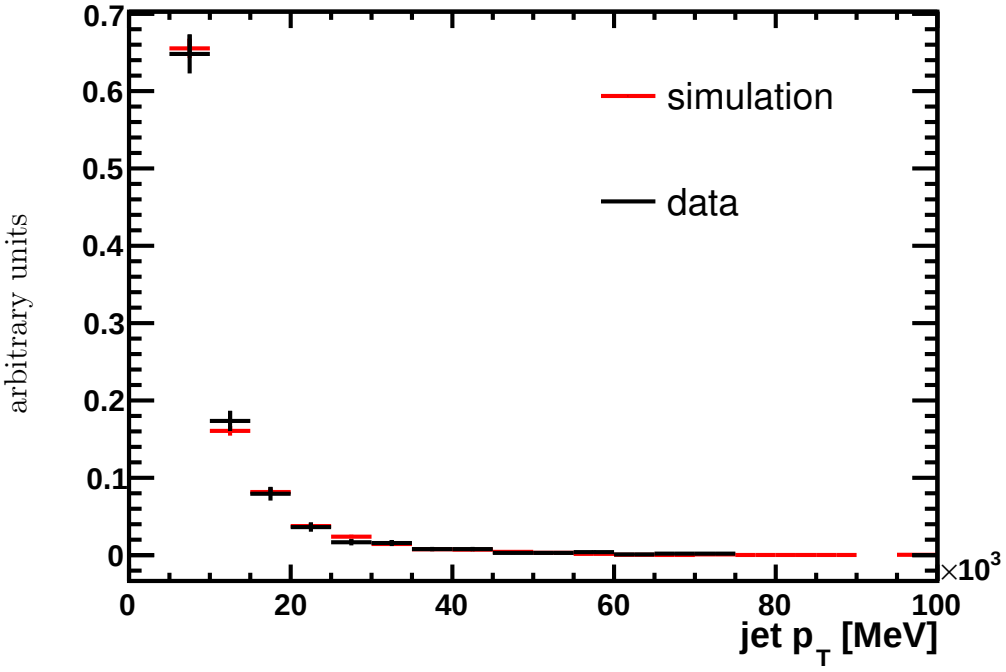

Figure 3.1: Transverse momentum distribution for raw jets in event with Z bosons.

are dominated by the associated production of a single jet and a Z boson. This is also seen in Figure 3.8. Momentum conservation demands in this case that the jet and the Z boson carry the same transverse momentum in opposite direction. This strict requirement holds if the jet and the Z are the only particles produced and is diluted by soft particles radiated as well as the proton remnant and the jet resolution.

In order to test whether these distributions are indeed caused by momentum correlations, an exclusive sample of Z events with exactly one jet is selected. The distributions are shown next to the fully inclusive distributions in Figures 3.4 to 3.7. It can be seen in Figure 3.4 that the peaks at $\pm\pi$ get enhanced by the requirement of a single jet and the difference in transverse momentum moves closer to zero as visible in Figure 3.4.

Comparing the simulation to data, a general pattern can be seen. The expected peaks in the distributions are broader in data compared to simulation. One reason is an insufficient description of the physics process that underestimates the jet multiplicity as it can be seen from Figure 3.8. Furthermore the distributions are broader due to a larger resolution due to pileup which was not effectively rejected at this stage.

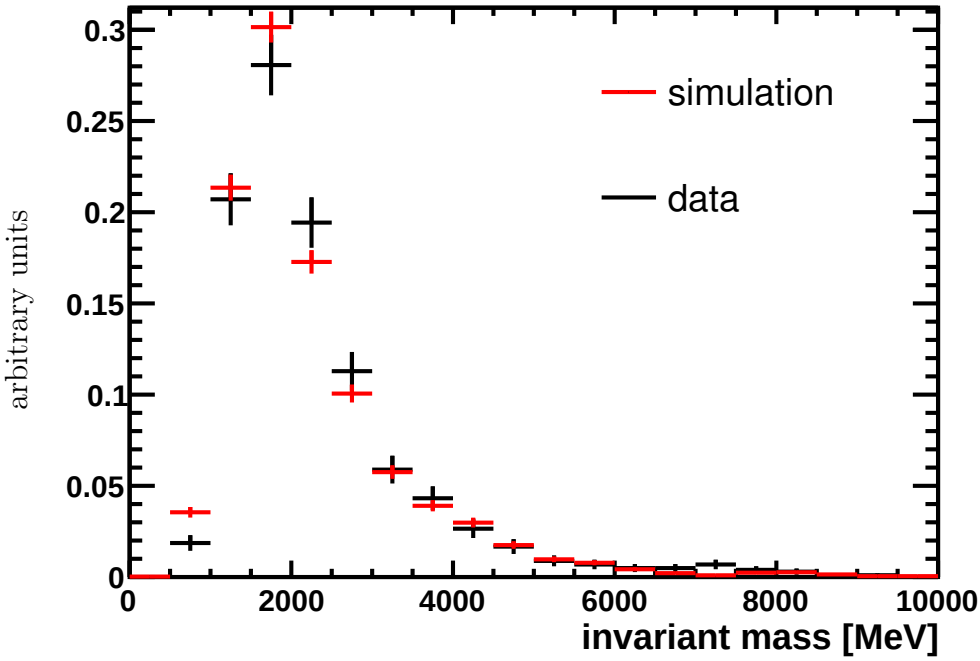

Figure 3.2: Invariant mass distribution for raw jets in event with Z bosons.

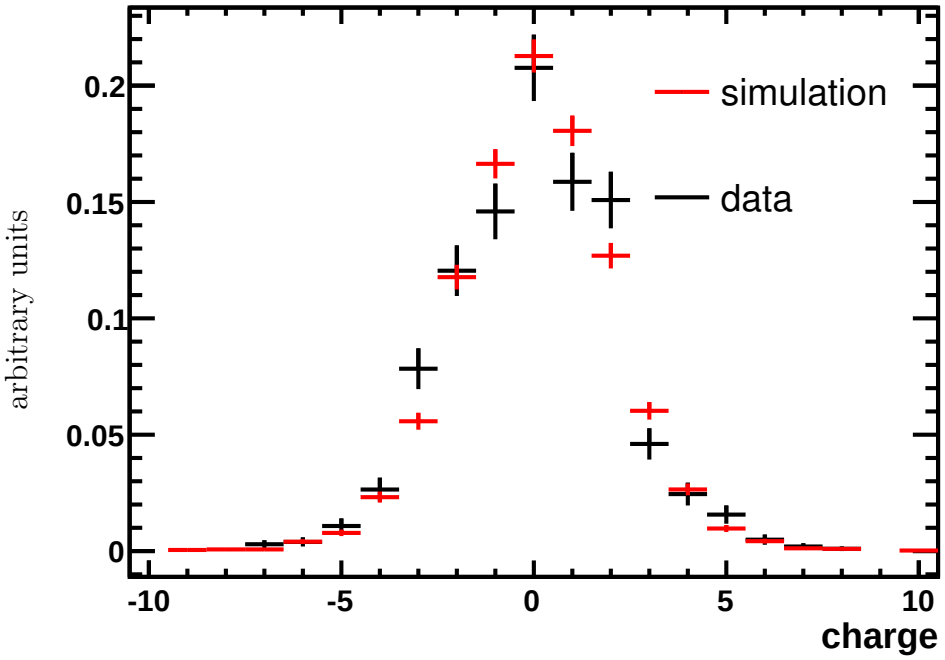

Figure 3.3: Jet charge distribution for raw jets in event with Z bosons. There is a slight shift in the positive direction as expected for soft forward jets from the $q = 2$ initial state.

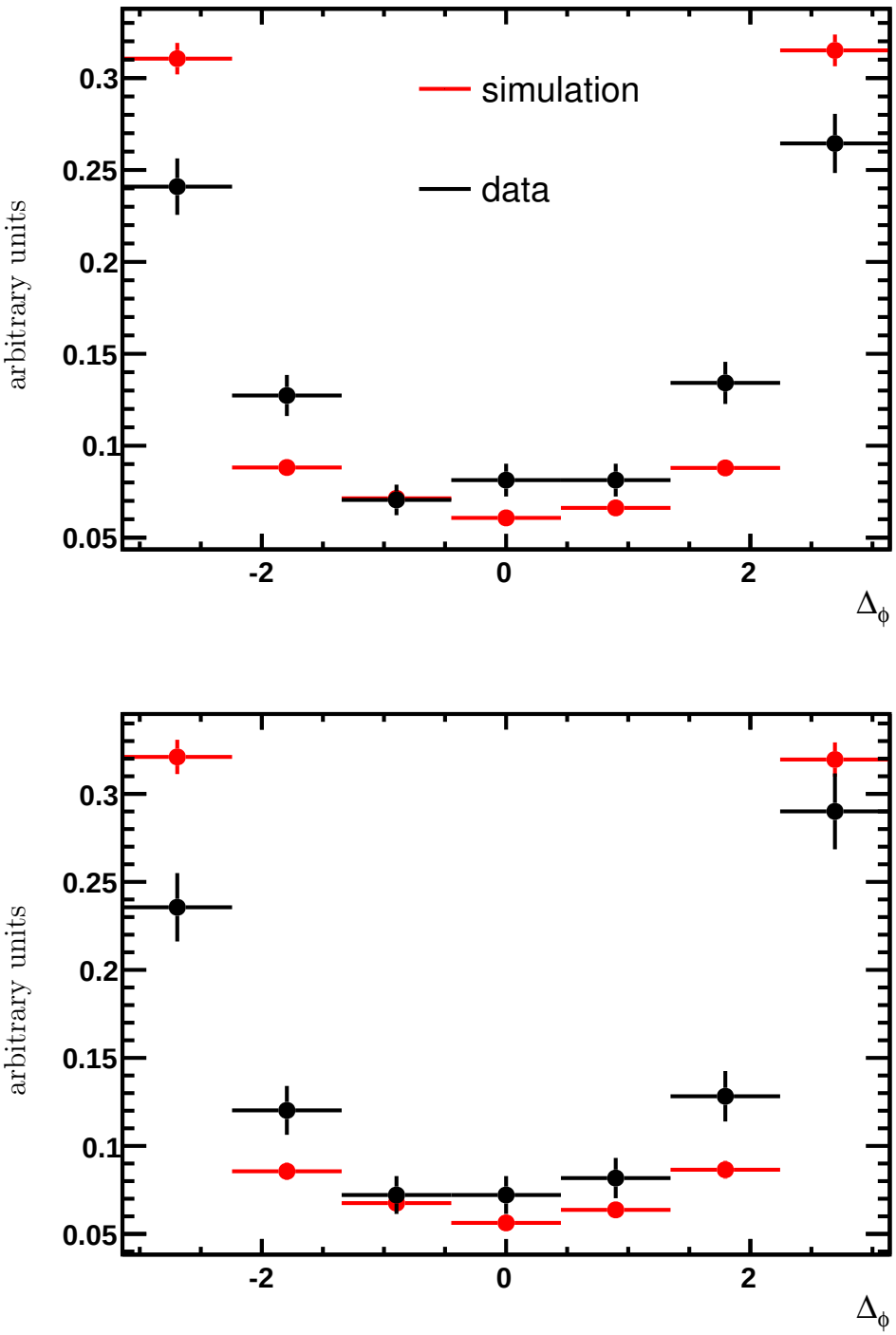

Figure 3.4: Difference in polar angle between Z boson and jet. The upper plot shows the inclusive distribution while the lower is enhanced in exclusive Z plus on jet events.

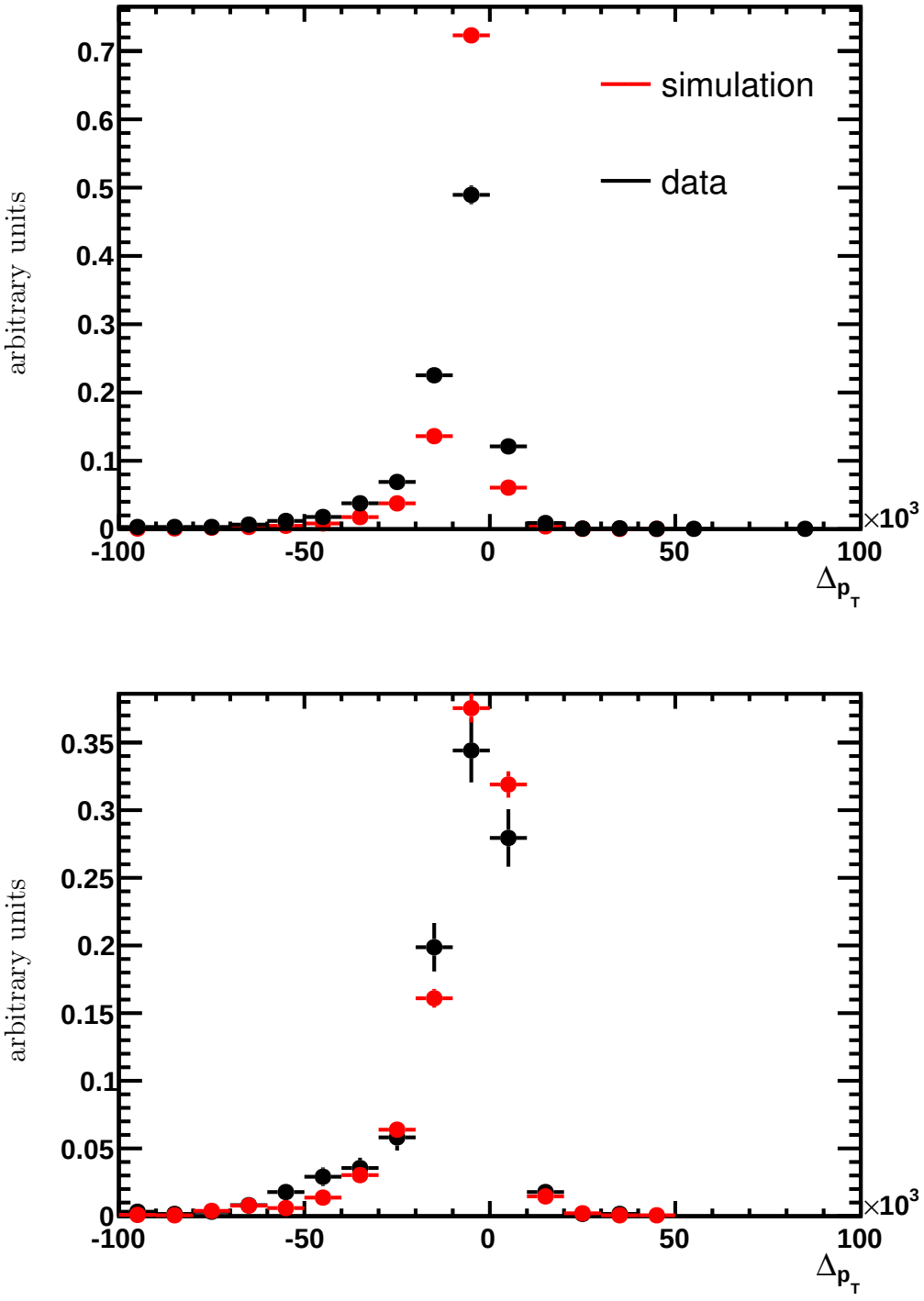

Figure 3.5: Difference in p_T between Z boson and jet. The upper plot shows the inclusive distribution while the lower is enhanced in exclusive Z plus on jet events. The Z boson and the recoil against each other. This leads to the peak at zero. This peak is shifted towards negative values from Z plus multi jet events. I moves closer to zero in the single jet enhanced sample.

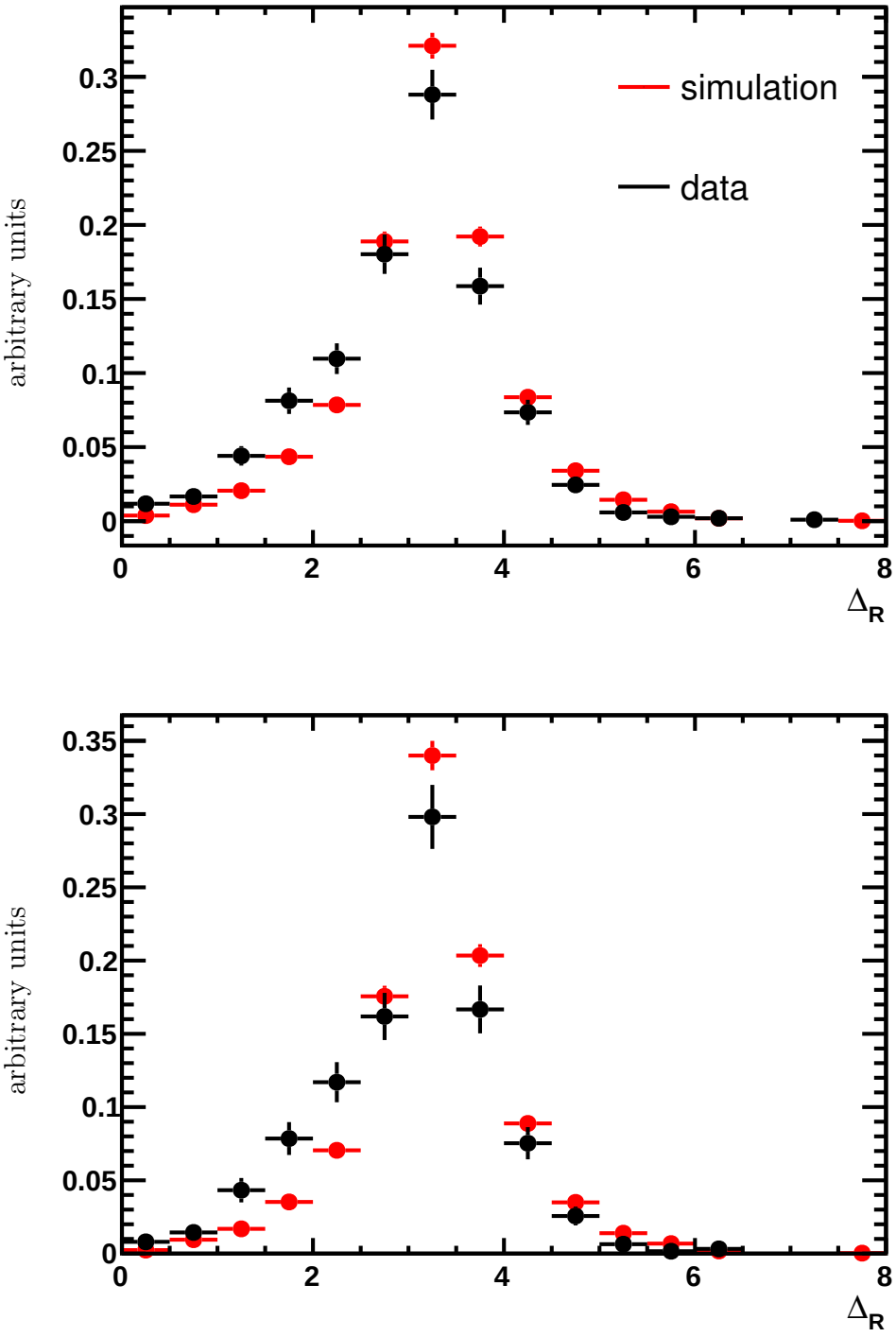

Figure 3.6: Distance in (η, ϕ) space between Z boson and jet. The upper plot shows the inclusive distribution while the lower is enhanced in exclusive Z plus on jet events. The peak at $\pm\pi$ from Figure 3.4 is preserved in this distribution. It is enhanced once the single jet events are selected and is overestimated in simulation.

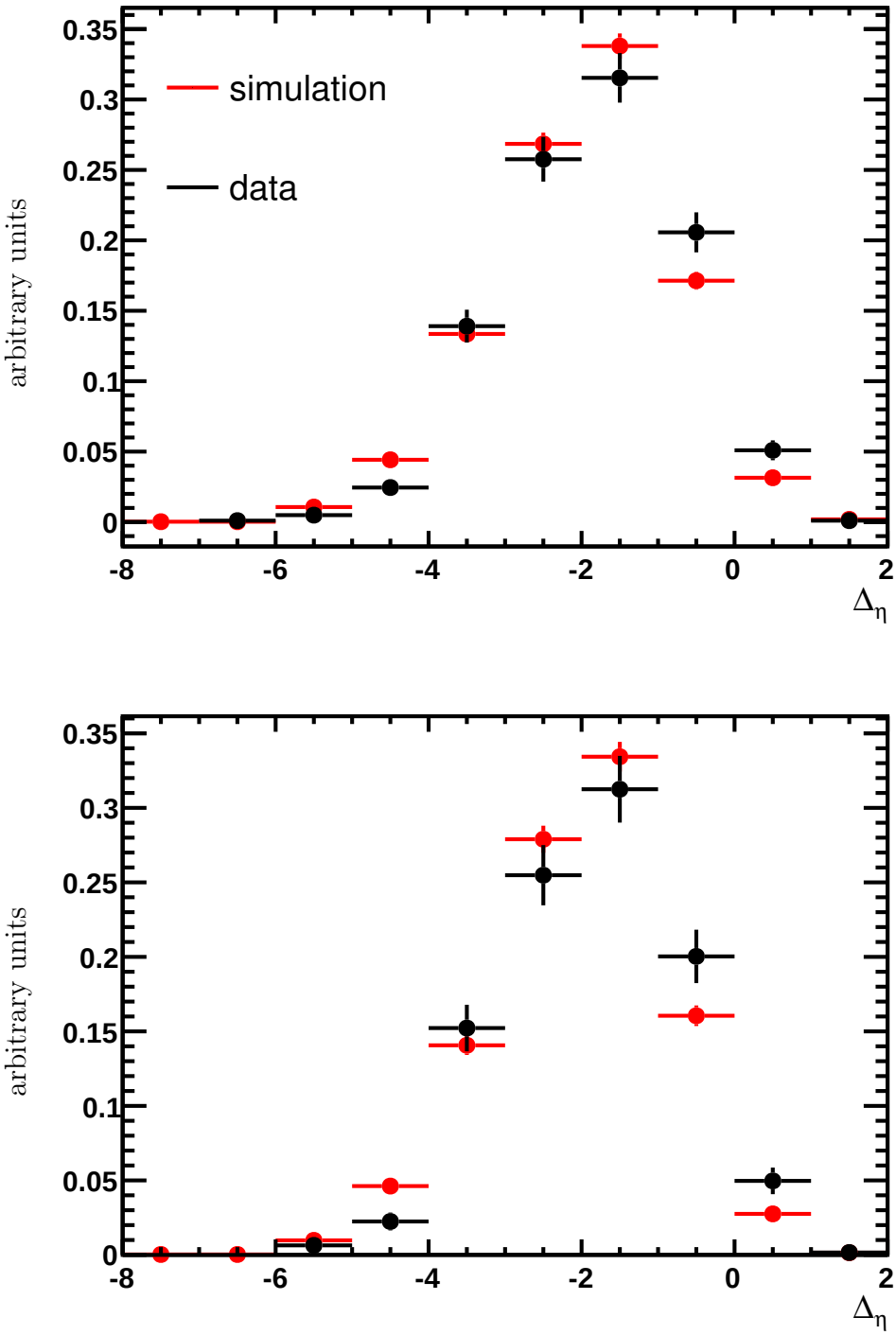

Figure 3.7: Difference in rapidity between Z boson and jet. The upper plot shows the inclusive distribution while the lower is enhanced in exclusive Z plus on jet events.

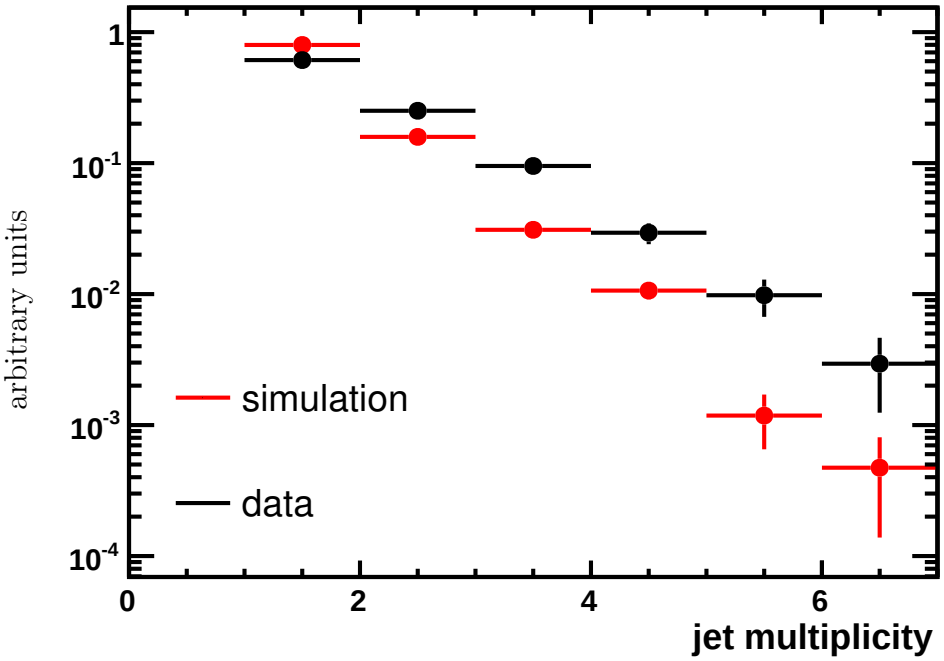

Figure 3.8: Jet multiplicity distribution for raw jets in event with at least on jet and a Z boson. The observed multiplicity is higher than predicted by PYTHIA.

3.2 Next Steps

The jets discussed so far are raw track-photon jets. These use the energy as it was measured in the detector with a limited particle acceptance. The definition used so far was only taking into account prompt stable charged particles and photons. The photon reconstruction is limited by the saturation in the ECAL, furthermore, neutrons, K^0_L and to some extent K^0_S are missed in this approach.

These deficits led to the development of what we now call ParticleFlow jets in LHCb. These were suggested and implemented by Victor Coco. These jets have the following improvements with respect to the jets I used to show that the LHCb detector is capable of jet reconstruction. The new algorithm also includes neutral clusters from the HCAL. To avoid double counting a χ^2 criterion is used to reject clusters from charged particles. That χ^2 criterion is based on the distance between the extrapolated impact position in the calorimeters and the reconstructed cluster. In case the energy of the charged particle is significantly higher than the energy assigned to the matched track, the additional energy is added as a neutral cluster. This procedure is beyond what the hadron calorimeter is designed for but improves the jet energy

resolution by 10%.

Instead of the pion mass hypothesis the tracks get the most probable particle hypothesis assigned. Hence a track can now have a π^+, p, K^+, e^+ or μ^+ hypothesis based on the measurement in the RICHes and the other PID subdetectors. This also allows for bremsstrahlung corrections to the electrons.

Two prong decays like $K^{*0} \rightarrow K^+\pi^-$; $\Lambda \rightarrow p\pi^-$; or $\phi \rightarrow K^+K^-$- so called V^0s - are reconstructed and the candidates used for that are removed from the set of primary particles in order to avoid double counting.

Upstream and VeLo tracks are now included with zero momentum assigned. Thus they do not change the energy of the jet but link it to a primary vertex. The jets are matched to the primary vertices by requiring that they contain at least three pointing particles. Pointing particles are prompt tracks and V^0s. When the jets are matched to a PV the influence of pile up jets is reduced.

3.3 Jet Energy Correction and Jet Matching

In order to obtain a measurement which is unbiased from detector effects a correction is needed. Several types of jets are defined.

Parton jets are jets consisting of quarks and gluons. Those jets can be calculated without taking hadronisation effects into account. These jets can not be observed in an experiment since partons are not asymptotic states.

Particle jets are jets consisting out of true particles in simulated events. The particle content of these jets can vary. In LHCb we chose the following particle content: The neutrinos were excluded in order to allow a common jet energy scale correction for light, charm and beauty jets. Due to semileptonic decays of heavy states those corrections are expected to be larger for heavy quark jets than for light jets.

Raw jets are jets with the energy reconstructed directly from the jet algorithm without additional corrections for invisible particles and mis measurements. Those jets are the starting point of the correction.

Corrected jets are raw jets that have a correction applied. The correction is tuned in order to remove any known bias in the energy measurement. The distributions obtained from corrected jets are blurred by the finite resolution. This has to be corrected for by an unfolding procedure

which is then applied on the level of the measured distributions of a specific analysis and not on the level of jet candidates.

In the language just defined the distributions shown so far correspond to raw jets without any unfolding applied.

The different levels of jets have to be matched. By construction this matching can not be perfect. Assuming a parton jet starts form a u quark which radiated more partons than the whole state that is formed from this will carry a charge of $\frac{2}{3}$ and the colour of the initial u quark. A particle jet cannot carry these quantum numbers. The charge will be integer and the state is a colour singlet. So the parton jet has to be colour connected to another parton jet to exchange colour and charge and thus energy. Matching parton jets to particle jets is not the topic of this thesis but similar problems arise when particle jets are matched to raw jets in simulated events.

For the matching of particle jets to raw jets there are several possibilities. With the given definition of a particle jet a perfect matching seems possible since every particle can potentially be reconstructed in the detector. So a truth matching can be performed on the particle level. In the simulation a true particle deposits energy in the active volume of a simulated detector that is then digitised to mimic the response of the front end electronics. These data are then analysed by the reconstruction algorithm which first builds clusters and then combines clusters to tracks. The clusters can be matched to the true particles and so can the tracks. Both is done by majority vote so if a large fraction of the clusters in a track are assigned to a true particle the track is assumed to correspond to that particle. This ansatz can be extended to the jets.

Once a large fraction of the of tracks and clusters in a raw jet is assigned to particles of a particle jet the raw jet is assigned to the particle jet. This criterion has the problem that the efficiency for the assignments is limited and thus better measured particles are more likely to be assigned to tracks than worse measurements. If only matched jets are considered this introduces a bias towards better measured jets. Another problem is that the experimental criteria are not infrared save. After many studies I abandoned all my efforts on that path.

The jet reconstruction group developed another strategy. There the jets are matched according to distance in η, ϕ space [85]. The two definitions are

Method 1 a true jet is matched to the closest jet in η, ϕ space.

Method 2 a true jet is matched to the hardest jet within it's "cone radius" of 0.5.

Both methods do give very similar results as it can be seen in Figure 3.9 were the distance distribution of the matches is shown.

From this method the quality of the jet reconstruction is assessed. It was documented in [85]. Also jet energy correction factors where obtained from the jets matched this way.

3.4 Uniformity of the Jet Reconstruction and Performance of the Hadronic Calorimeter

Once angular distributions are measured it is important to check whether the reconstruction efficiency is uniform in the angular variables. One way of doing this is using a process that is expected to be symmetric in the variable and check whether this is observed in the data. In order to get a large sample of jets to do this which is largely independent of the Z sample the $W^{\pm}$ stripping line was used. This stripping line requires a muon with $p_T > 10\,\text{GeV}$. This sample is dominated by semileptonic beauty decays; $W^{\pm}$ and Z events. The polar angle distribution is shown in Figure 3.10. This is compared to a smoothed symmetric version of the same data. Technically the smoothing was performed by a Fourier transform with the high frequencies removed. The symmetry was imposed on that distribution by removing the odd terms. The Fourier transform was chosen in order to get the boundary conditions right. That means the smoothed distribution has to give the same values at $\pm\pi$. The same argument holds for the derivatives.

Many structures are visible in the jet ϕ distribution. The structure is partially understood and explained in the following.

The comparison to the smoothed distribution reveals that there are a few spikes in the distribution which are expected to be noisy cells.[2]

There are broad peaks around zero and $\pm\pi$. Those are due to misidentified soft charged particles. A soft charged particle emitted forward will have a low p_T and should have little impact on the jet reconstruction. If this particle is not reconstructed as a track but measured in the CALOs it will be measured at a higher p_T if it was bend to the outside in the magnetic field. This is because in the neutral hypothesis a straight line to the PV is assumed which corresponds to an higher scattering angle with respect to the actual curved trajectory. This is depicted in Figure 3.11. The peak at $\pm\pi$ is larger than the one at zero. The origin of this difference is unknown.

Leaving aside the peaks from the charged particles there are two broader peaks remaining. To see what to expect from pure geometry a simplified

[2]Most notably the spike at 2.2.

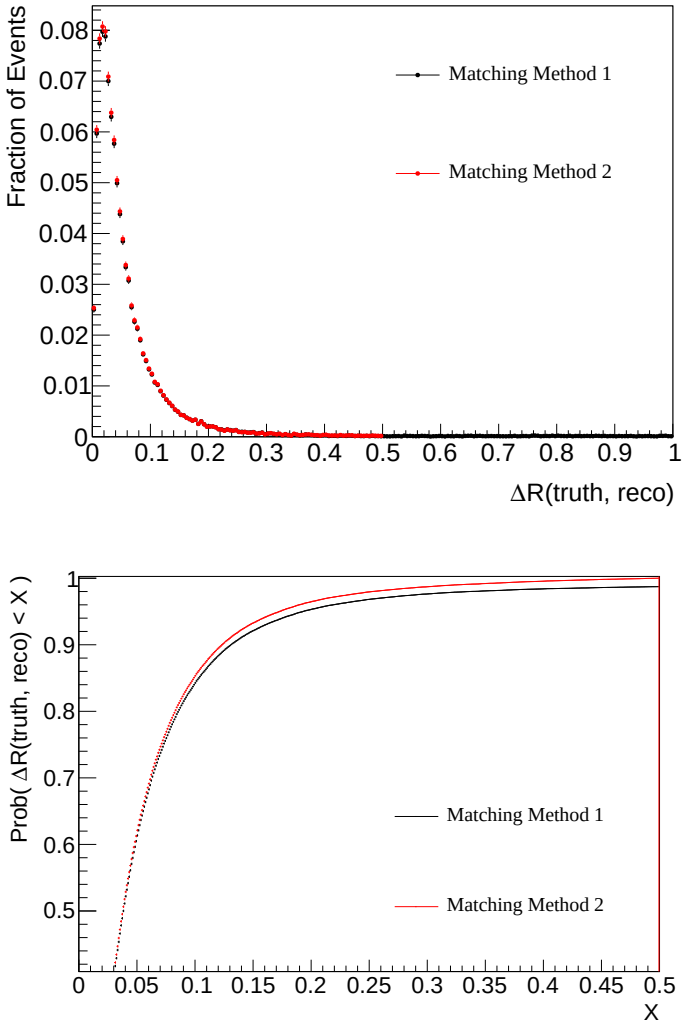

Figure 3.9: Matching distance for simulated particle jets and the corresponding reconstructed raw jets. From [85].

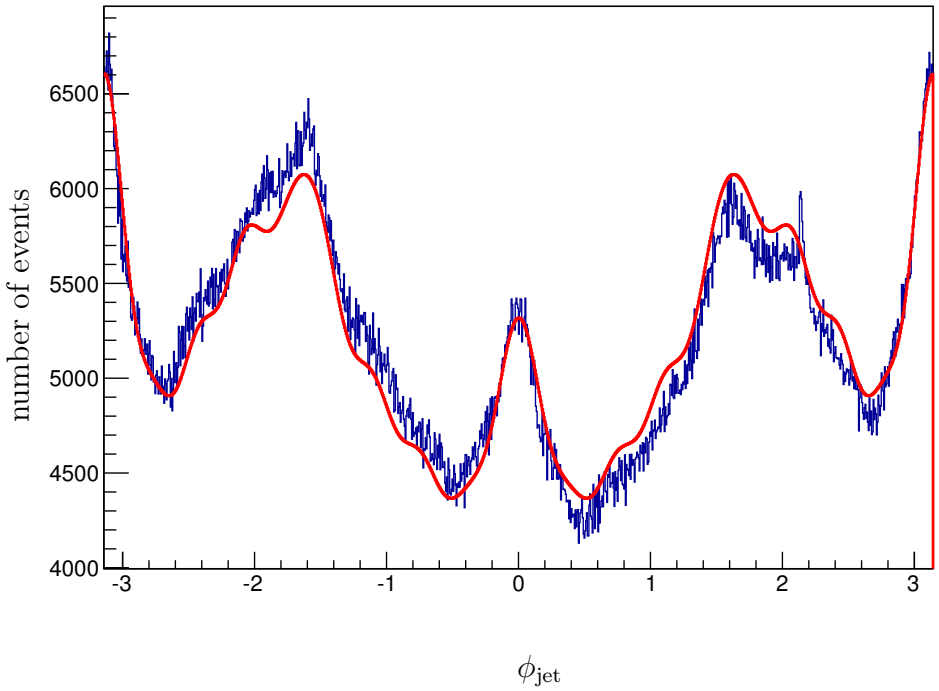

Figure 3.10: Polar angle distribution of reconstructed jets. The axis is zoomed to enhance the visibility of the effects discussed.

rectangular acceptance model is used. The used values are inspired from Figure 3.12 and are set to $a = 0.28$ and $b = 0.22$. Then the boundaries of the calorimeter in terms of ϕ are given by

$$r_{\max} = \begin{cases} \sqrt{b^2 + b^2 \cot^2(\phi)} & \text{horizontal boundary} \\ \sqrt{a^2 + a^2 \tan^2(\phi)} & \text{vertical boundary} \end{cases}$$

The surface element is then given by:

$$\int_0^{r_{\max}} r \, \mathrm{d}\, r = \frac{1}{2} r_{\max}^2 \tag{3.1}$$

If the particle fluxes are symmetric around the origin and positive the edges of the acceptance must be visible at the same position in the ϕ distribution. The heights of the observed spikes do depend on the flux in the outer regions of the HCAL but the qualitative features remain.

So the geometry would suggest that those peaks are in fact twin peaks caused by the four edged calorimeter. The best candidates for the twin peaks are at ± 2 and ± 1.8 and pronounced in the Fourier - smoothed distribution - where they also could be an artefact of the removed frequencies.

Assuming the twin peaks are at the positions mentioned then there is a slope in the data that cannot be explained just by the coordinate transformation. At least the HCAL geometry suggests that the twin peaks should be at about $\|\phi\| \in \{0.7, 2.5\}$ and further apart than observed. However this simplified picture might change if acceptance of other subdetectors and the gap between inner and outer HCAL are taken into account. The central hole in the HCAL does not contribute extra edges since the reconstruction algorithm imposes a limit on η that excludes that region.

Another feature observed in these data is that the data lie below the smoothed curve on the negative side and above on the positive side. This indicates a top down asymmetry in the detector. One reason for this might be that the calorimeters are mounted vertically while LHC is tilted by 2.5% at IP8.

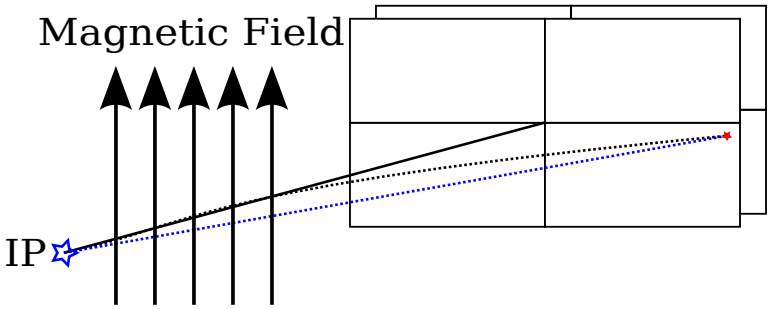

Figure 3.11: Many soft hadrons are emitted forward. If a charged hadron is not reconstructed as a track (black dotted) but seen in the hadron calorimeter then the hadron is assumed to be neutral. In this case the only known information about the particle is the cluster energy which gets combined with the assumption that it was a neutral particle produced at the PV. That means a straight line from the PV to the cluster is assumed for the trajectory (blue dotted) . Since for many hadrons the initial scattering angle ϑ is small it tends to lead to an overestimation of the scattering angle. This then leads to an overestimation of the scattering angle. Since p_T is calculated from the scattering angle and the cluster energy p_T is overestimated. The dipole field indicated by the arrows bends these particles towards the sides. This explains why these misidentified particles are seen at $0, \pm\pi$ in ϕ.

3.4.1 Hot Cells in the HCAL

One source of wrong measurements of neutral hadrons are noisy cells in the calorimeters. Those are best identified by investigating the digits from the cells themselves instead of looking at jets or clusters. The distributions are shown in Figure 3.14 as function of the row and column indices. Since the particle production is enhanced in the forward region the distributions are dominated by the physics. In order to focus on the technical aspect an asymmetry variable was used:

$$x_{i,j} = \frac{n_{i,j} - \frac{1}{4}\sum_{\text{4 Cells}} n_{k,l}}{\sum_{\text{4 Cells}} n_{k,l}} \tag{3.2}$$

"4 Cells" refers to the four cells that are at the positions mirrored at the $x-z$ any $y-z$ plane measured in row and column index. The four cells should see very similar illumination and are used as reference cells for each other. If the illumination is symmetric around the beam and all four cells work correctly then this variable is close to zero. This renders noisy cells more visible. The obtained distributions are shown in Figures 3.15 and 3.16.

The inner HCAL is more noisy than the outer HCAL. The maximal value of the asymmetry variable is about 0.2 in the inner HCAL while it is about 0.08 for the outer HCAL. In the outer HCAL there are only isolated noisy cells while in the inner HCAL there is row 24 which is noisy in columns 3 - 10. The energy spectra of six identified noisy cells are shown in Figures 3.17 to 3.22 and listed in Table 3.1. The spectra show different behaviour. Some have distinct regions where the rate is higher while others don't have visible features.

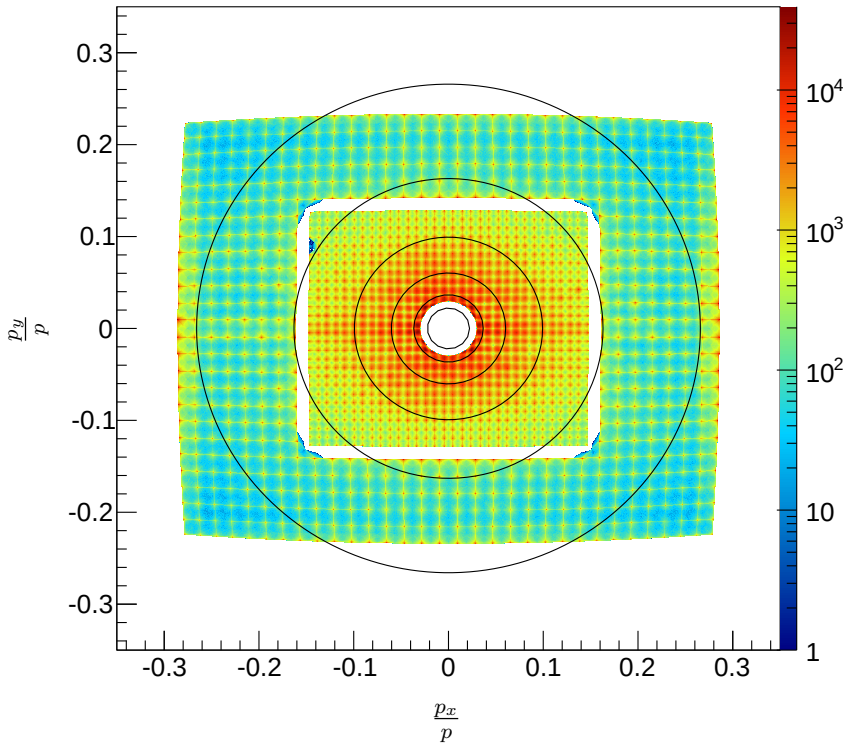

Figure 3.12: Reconstructed neutral hadrons. No noisy cells visible in this view but a dead cell in the inner HCAL. The boundary between inner and outer HCAL is clearly visible. The rings depict the pseudorapidity $\eta \in \{2.0, 2.5, 3.0, 3.5, 4.0, 4.5\}$. There is a limit at high pseudorapidities in the neutral hadron reconstruction algorithm.

HCAL region	column	row	cell ID
Inner	23	26	5783
Inner	23	8	5576
Inner	0	19	5312
Outer	0	16	1024
Outer	0	22	1408
Outer	26	22	1034

Table 3.1: Identified hot cells in the HCAL. The spectra are shown in Figures 3.17 to 3.22.

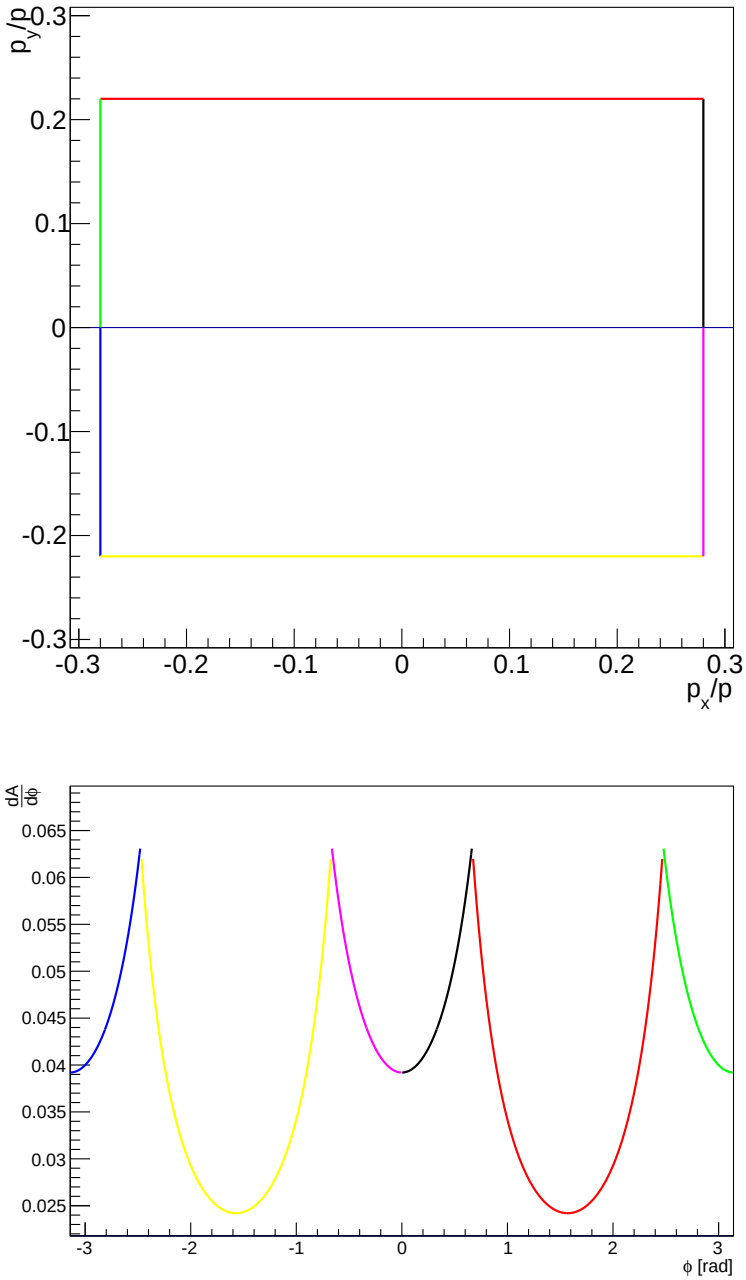

Figure 3.13: Acceptance model for the HCAL both in Cartesian and in polar coordinates. This acceptance model assumes everything is seen in a rectangular region with $\|p_x/p\| < 0.28$ and $\|p_y/p\| < 0.22$. It neglects the hole in the centre for the beampipe as well as the dead region between inner and outer HCAL. The different colours indicate the boundaries and match between the plots.

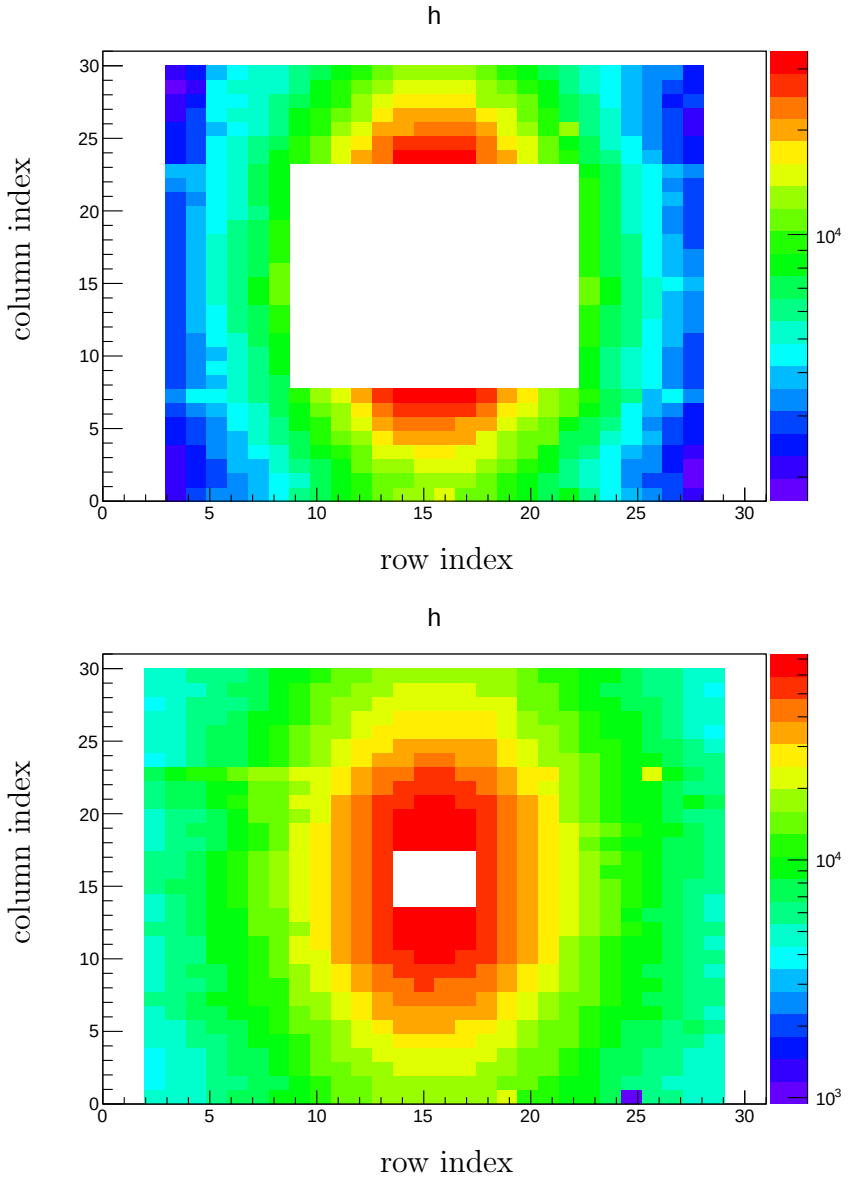

Figure 3.14: Distribution of HCAL cells above threshold. The top plot shows the outer and the bottom plot shows the inner HCAL.

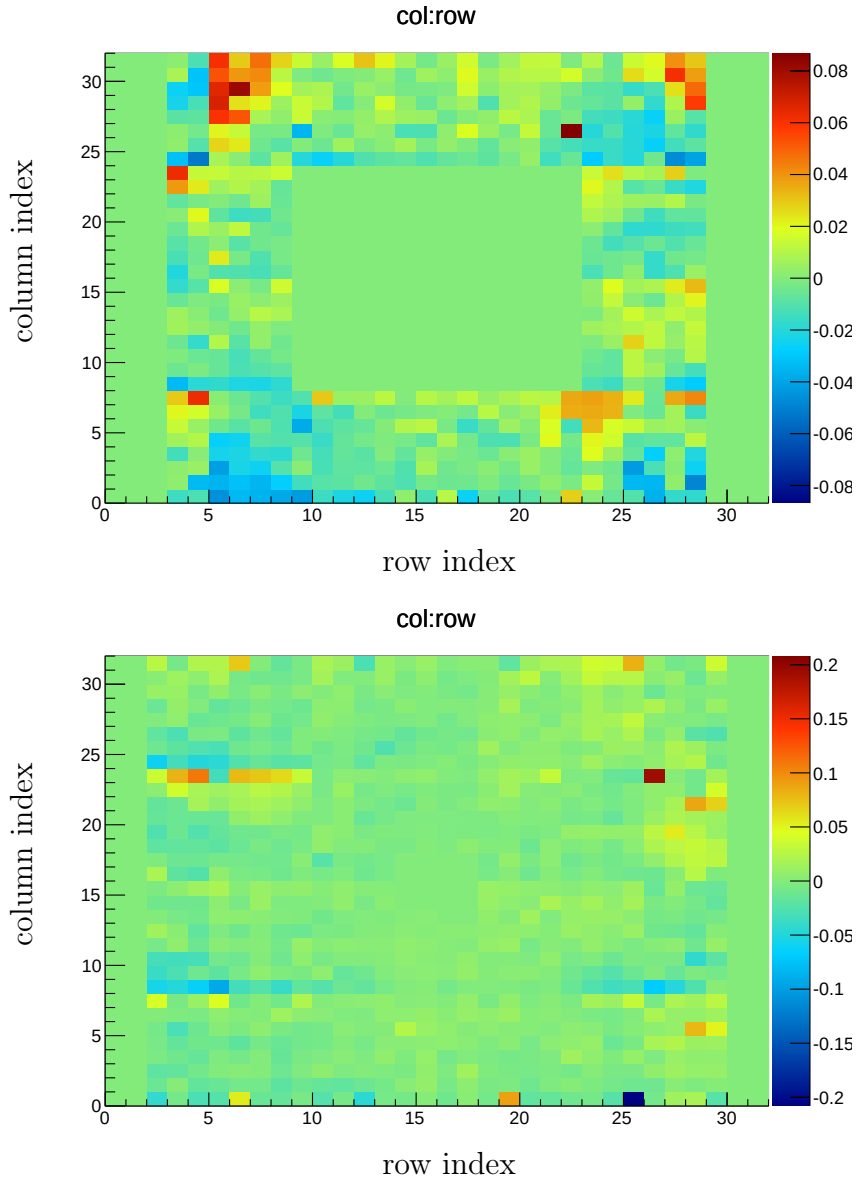

Figure 3.15: Asymmetry measured in number of cells above threshold. The top plot shows the outer and the bottom plot shows the inner HCAL.

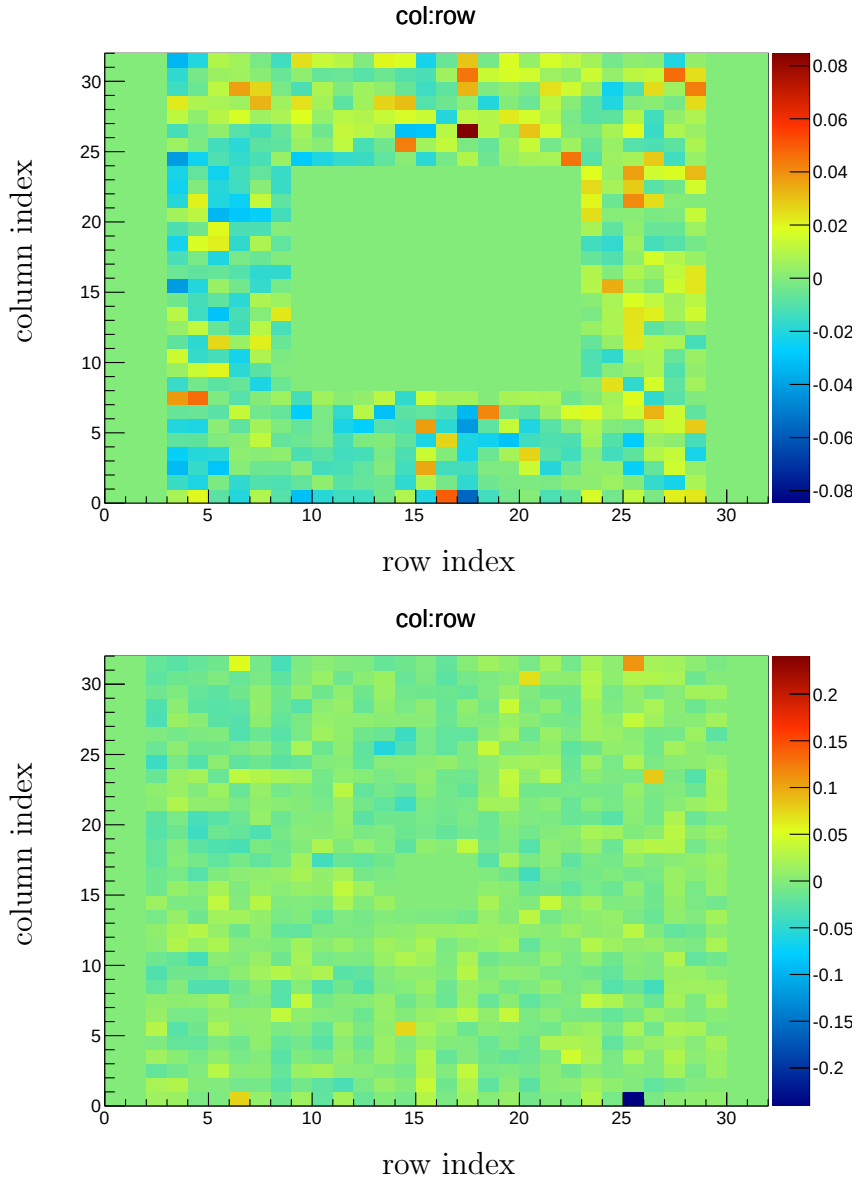

Figure 3.16: Asymmetry measured in number of cells above threshold. The top plot shows the outer and the bottom plot shows the inner HCAL.

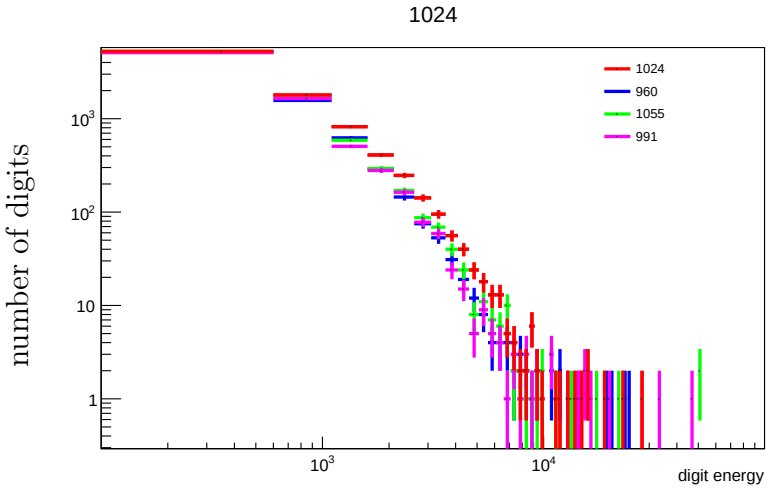

Figure 3.17: Cell 1024 has a higher rate in the intermediate energy range compared to the reference cells.

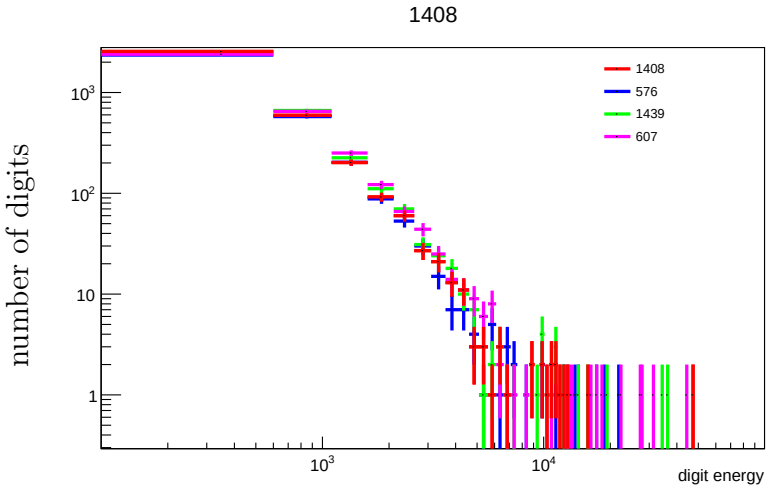

Figure 3.18: Cell 1408 has no obvious pattern but still a asymmetry variable of 6%.

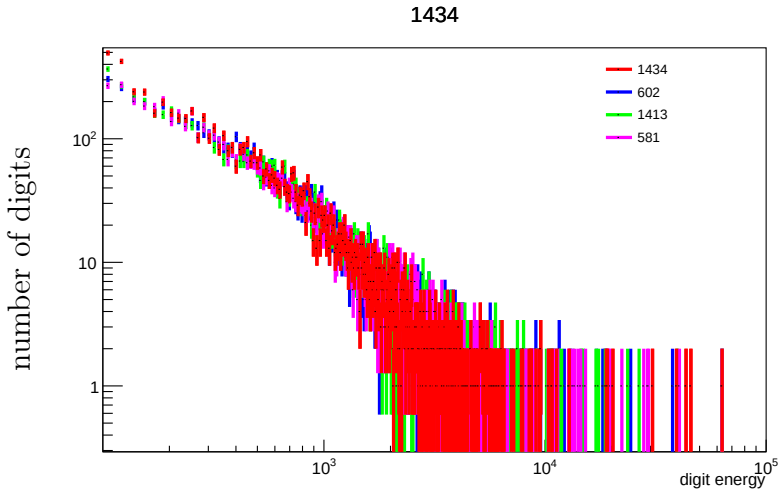

Figure 3.19: Cell 1434 has most of the excess events measured at low energy.

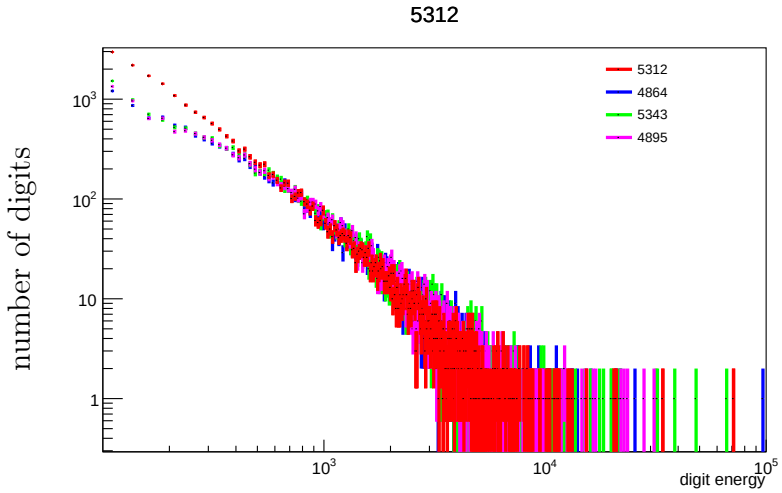

Figure 3.20: Cell 5312 also has a large excess at low energy.

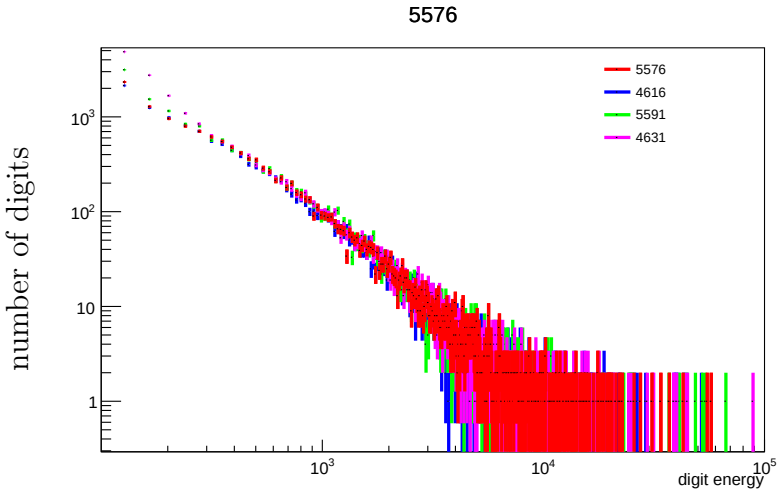

Figure 3.21: Cell 5576 also has a large excess at low energy.

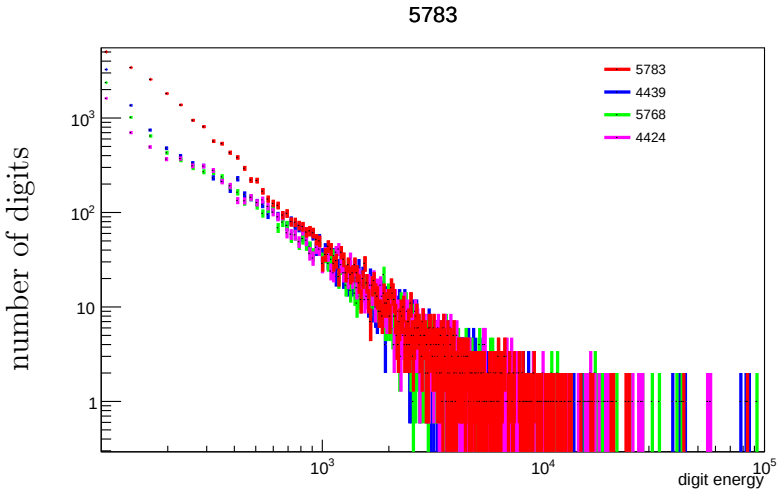

Figure 3.22: Cell 5783 also has a large excess at low energy.

The studies mentioned above lead to cross checks of the official LHCb analysis of the associated production of Z bosons with jets. The results of the official analysis are published in [77] and summarised in the following section.

3.5 Results

The jet selection criteria have been evolved from the initial criteria described before. The Z boson is selected the same way as before. The jets are required to have $p_T > 10(20)\,\text{GeV}$ and $2 < \eta < 4.5$. In order to avoid bias from reconstructed final state radiation an angular distance of 0.4 between the jet and the muons is required. The jet quality criteria are as described in Section 3.3. The cross section for the associated production has been measured to be:

$$16.0 \pm 0.2(stat.) \pm 1.2(syst.) \pm 0.6(lumi.)\,\text{pb}$$

for a jet transverse momentum threshold at 10 GeV and:

$$6.3 \pm 0.1(stat.) \pm 0.5(syst.) \pm 0.2(lumi.)\,\text{pb}$$

for a jet threshold at 20 GeV. When the ratio between the total inclusive Z boson production and the associated production with jets is taken the uncertainties for the Z reconstruction and the luminosity determination largely cancel. The measured ratios are $0.209 \pm 0.002(stat.) \pm 0.015(syst.)$ and $0.083 \pm 0.001(stat.) \pm 0.007(syst.)$. Nevertheless the systematic uncertainty is dominated by the uncertainty of jet energy scale and therefore does not cancel in the ratio.

Measurements of the cross section ratios differential in leading jet (Figure 3.23) and Z boson (Figure 3.24) transverse momentum; leading jet pseudorapidity (Figure 3.25); rapidity of the Z boson (Figure 3.27); difference in the azimuthal angle (Figure 3.28) and in the rapidity of the Z boson and the leading jet (Figure 3.26) are are compared to (N)LO predictions with parton shower from POWHEG and PYTHIA using three different PDF sets.

The p_T^{jet} distribution in 3.23 is predicted too soft at LO but is reasonable described in the NLO prediction. The p_T^{Z} distribution in 3.24 distributions are poorly described in the low region. Surprisingly the LO prediction overshoots in the lowest bin for the 10 GeV threshold while it overshoots for the 20 GeV threshold. The (pseudo) rapidity distributions are mainly shown in Figures 3.25 to 3.27 are mainly sensitive to the PDFs. This can be seen from the large variations from the different PDF sets. The $\|\Delta\Phi\|$ distribution

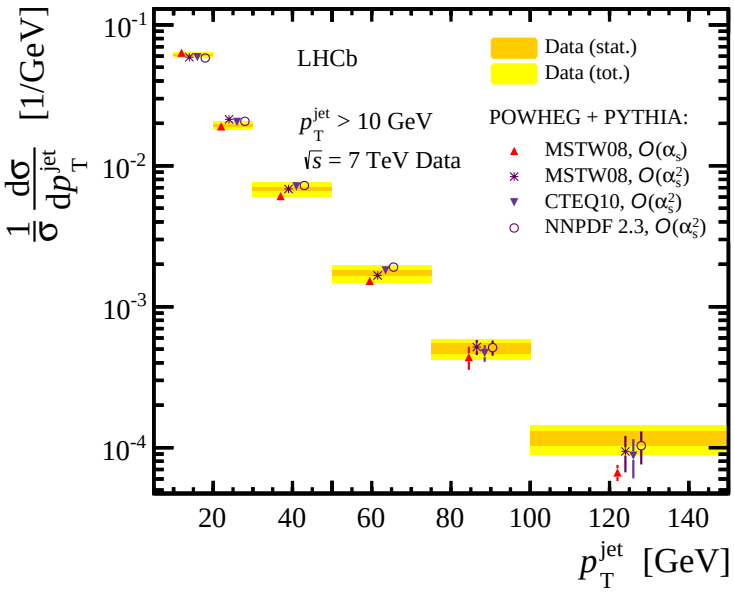

Figure 3.23: Transverse momentum spectrum of the leading jet in events with Z bosons.

is sensitive to additional QCD radiation. As expected the LO with parton shower prediction peaks much more pronounced than observed in data.

Summarising the arguments that were used to establish the signal were turned into a precise measurement.

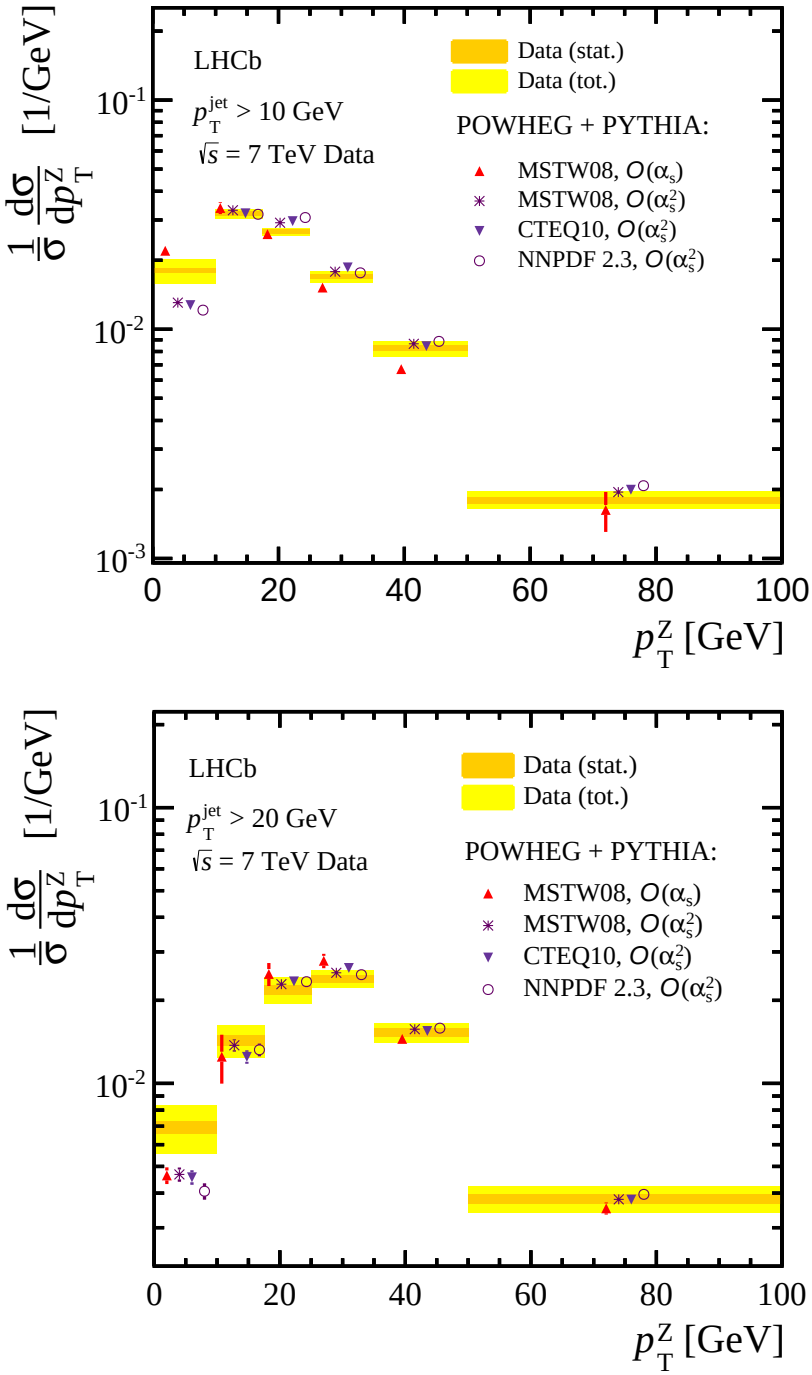

Figure 3.24: Transverse momentum spectrum of the Z boson in events with jet above $p_T > 10\,\text{GeV}$ (top) and $p_T > 20\,\text{GeV}$ (bottom).

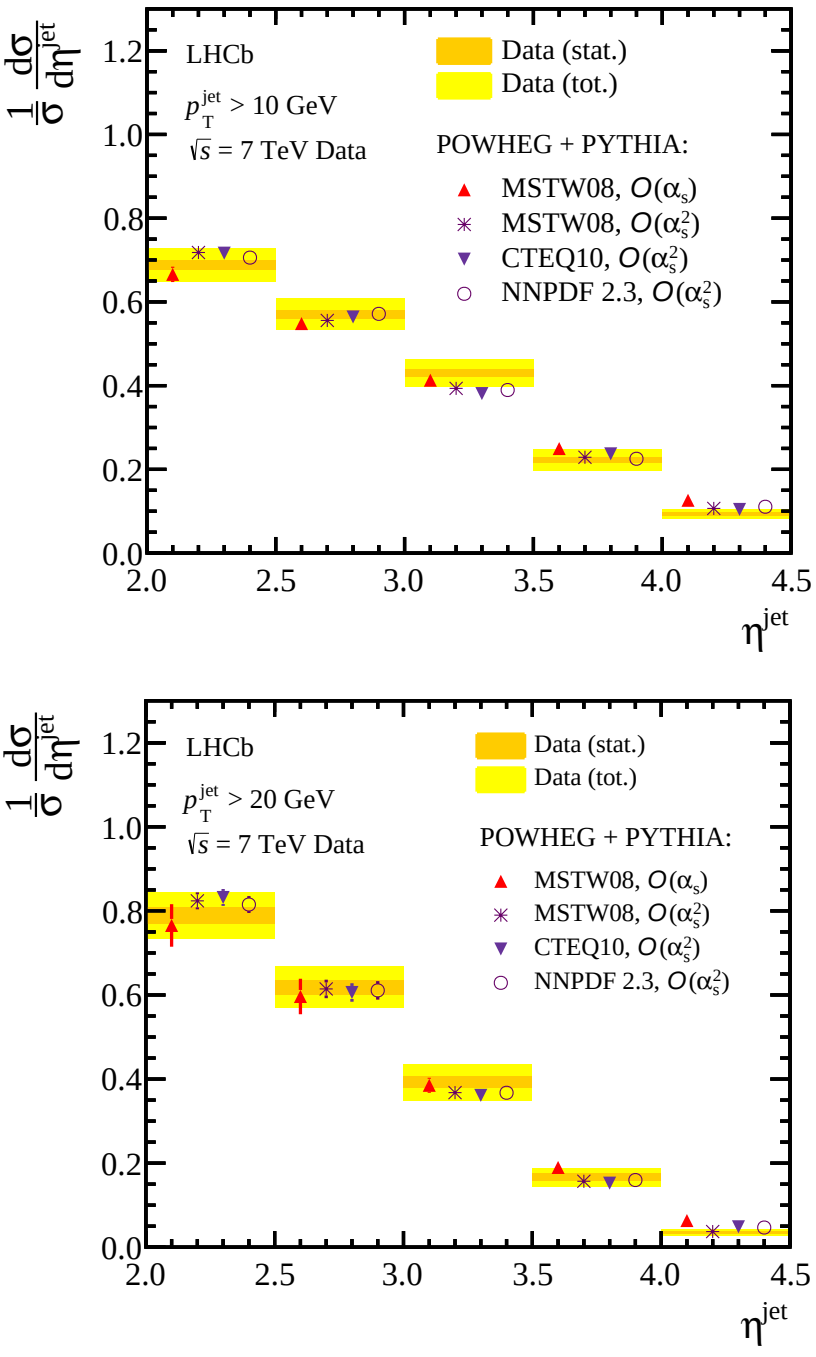

Figure 3.25: Pseudorapidity distribution of the leading jet in Z plus jet events with the jet above $p_T > 10\,\text{GeV}$ (top) and $p_T > 20\,\text{GeV}$ (bottom).

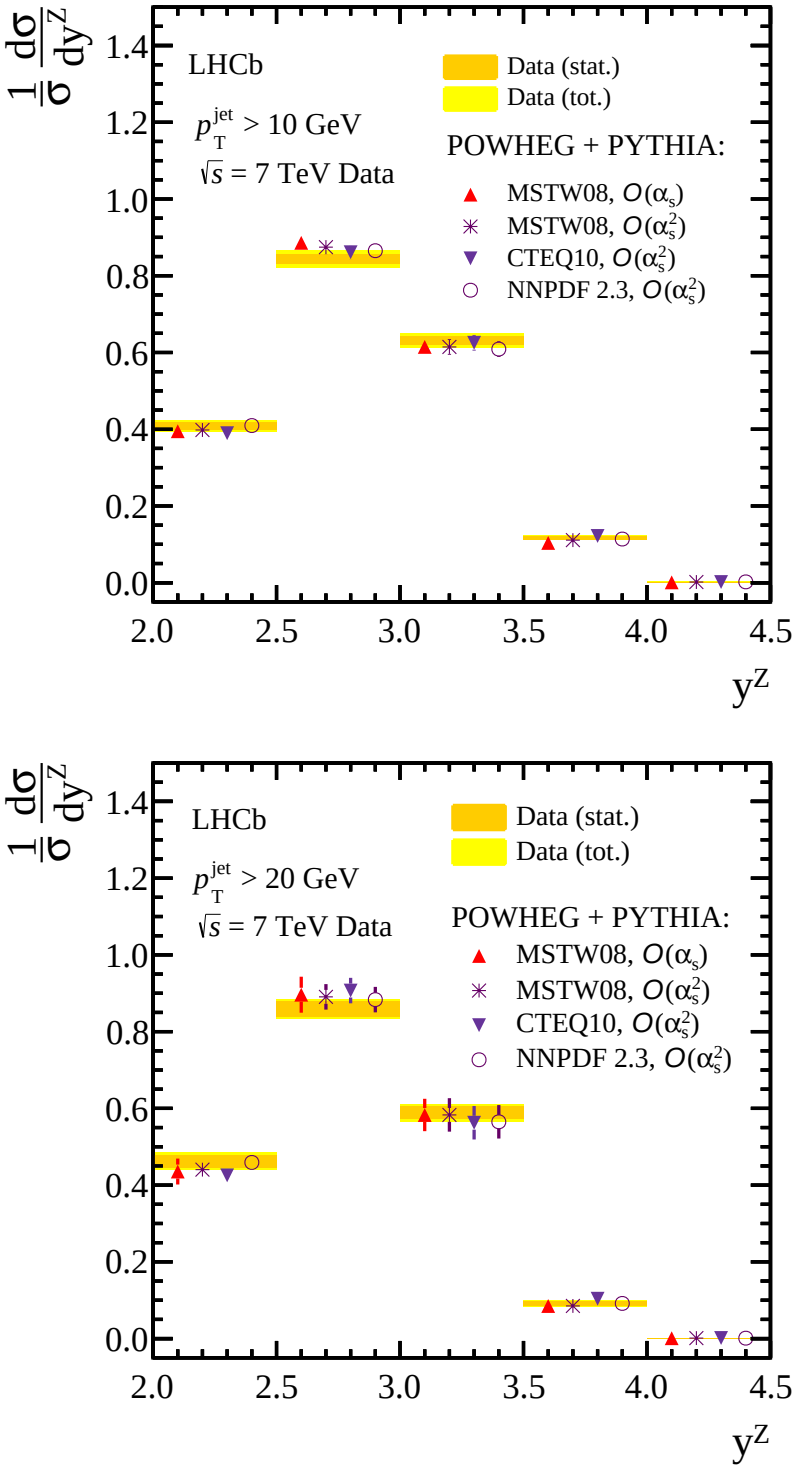

Figure 3.26: Rapidity distribution of the Z boson in events with jet above $p_T >$ 10 GeV (top) and $p_T > 20$ GeV (bottom).

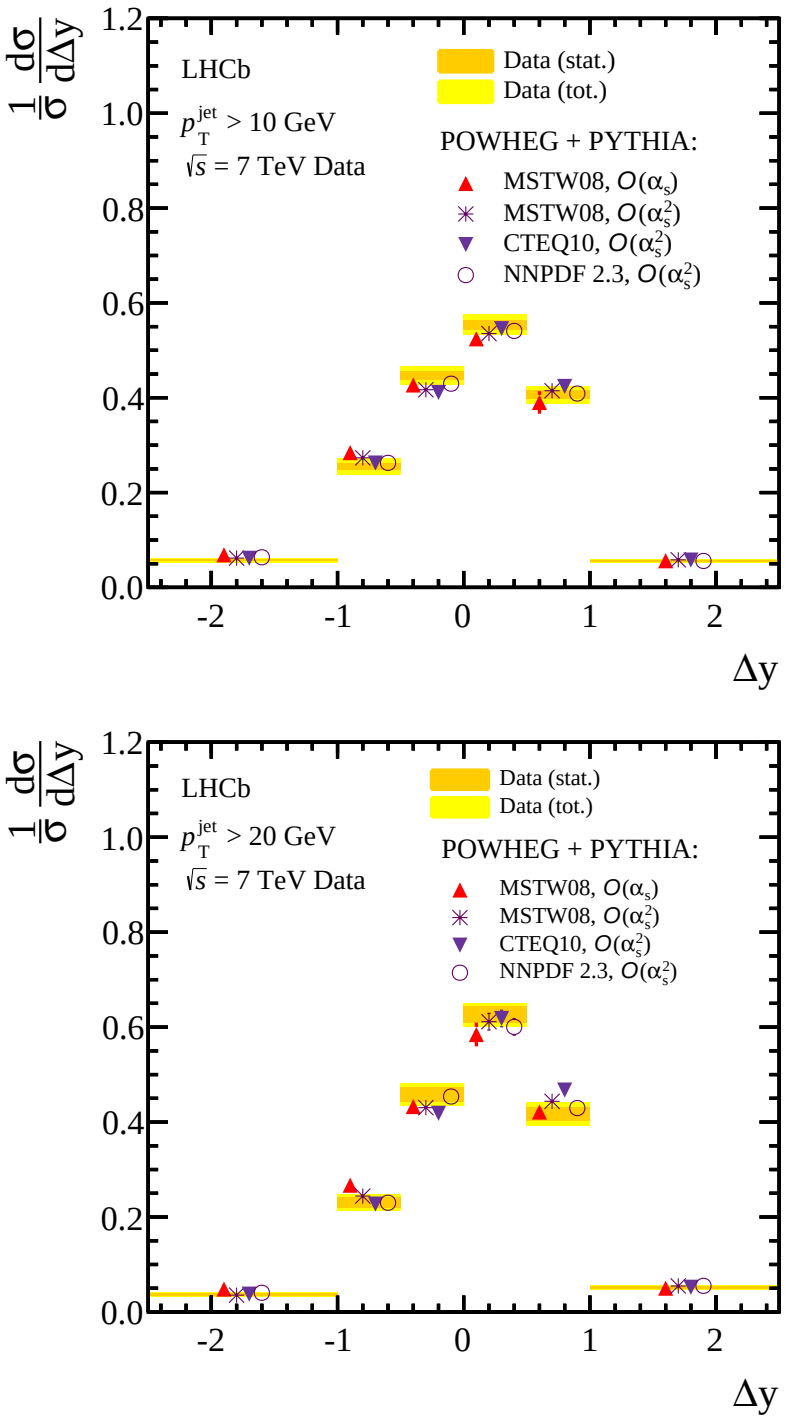

Figure 3.27: Difference in rapidity of the leading jet and the Z boson.

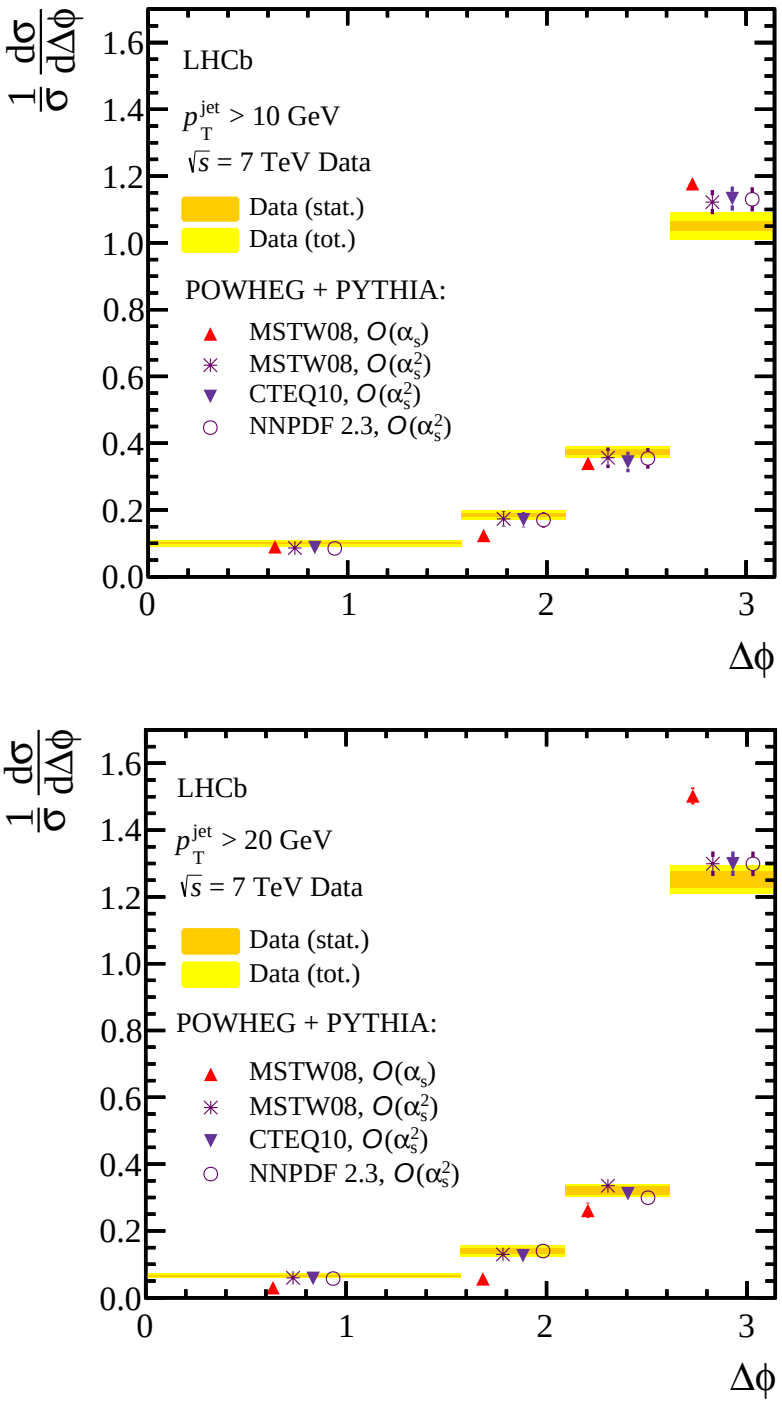

Figure 3.28: Difference in polar angle of the leading jet and the Z boson.

Chapter 4

Measurement of the Cross Section for the Associated Production of Z Bosons with D Mesons at $\sqrt{s} = 7$ TeV

This chapter is a revised version of the analysis note LHCb-ANA-2013-047 that accompanied the publication of the shown results [78]. That note was written by myself; Vanya Belyaev and Katharina Müller.

4.1 Introduction

A search for the associated production of Z bosons and charmed hadrons is presented. The analysis is based on the full pp dataset taken in 2011 at $\sqrt{s} = 7$ TeV. The Z boson is reconstructed in the $Z \to \mu^+\mu^-$ final state and the charmed hadrons are reconstructed in the following final states:

- $D^0 \to K^-\pi^+$,
- $D^+ \to K^-\pi^+\pi^+$,
- $D_s^+ \to (K^-K^+)_\Phi\pi^+$ and
- $\Lambda_c^+ \to pK^-\pi^+$.

The branching fractions are shown in Table 4.2.

Unless explicitly stated charge conjugated modes are implied throughout this chapter. Like in the rest of this thesis Z production includes the virtual photon contribution. The charmed hadron reconstruction exploits the track reconstruction and particle identification capabilities of the LHCb detector and selects very pure samples of charmed hadrons [69].

This analysis is sensitive to similar physical properties of the proton compared to those probed with the double charm production paper [40] and the inclusive $Z \to \mu^+\mu^-$ measurement in [69]. The focus however is shifted to high Bjorken–x and the charm parton density function instead of charm production at low x in [40] and light quark and gluon parton density functions in [69].

This measurement can also provide insights into the charm production mechanism; double parton scattering (DPS) [86–89] and intrinsic charm (IC) [30] models.

4.2 Strategy

The analysis combines the Z candidates from [69] with the charmed hadron candidates from [40]. The properties reused from those analyses are summarised in Sections 4.4.1 and 4.4.2. The key tool for the combination is the `DecayTreeFitter`. This tool is used to differentiate between events with Z plus D from a single pp interaction (signal) and the Z and D production in two different pp interactions (pileup). The selection criterion based on this is described in Section 4.4.3 and the residual background from pileup in Section 4.6.1. The residual background is assessed using a two dimensional fit to the $\mu^+\mu^-$ and charm hadron candidate mass described in Section 4.7.

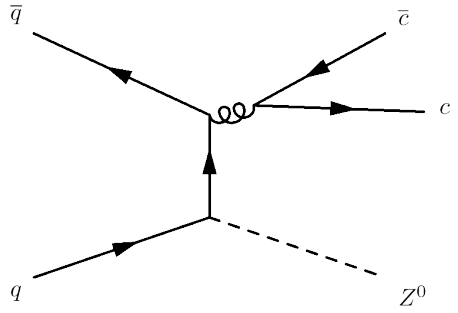

(a) $c\bar{c}$ production with Z-strahlung from initial state.

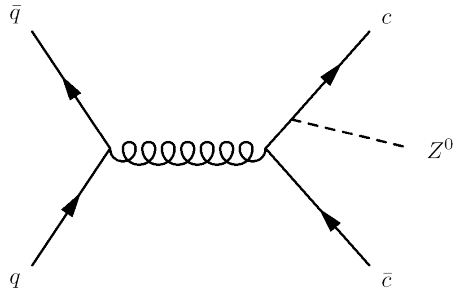

(b) $q\bar{q} \rightarrow c\bar{c}$ production with Z-strahlung from final state.

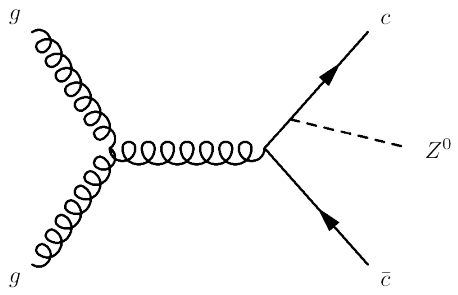

(c) $gg \rightarrow c\bar{c}$ production with Z-strahlung from final state. Can be switched off in MCFM with the `omitgg` flag.

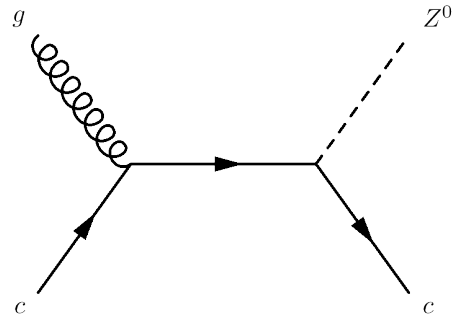

(d) c quark scattered out of the sea with Z-strahlung from final state.

Figure 4.1: Single parton scatter Z plus c production processes at tree level.

4.3 Theory Input

4.3.1 Single Parton Scattering (MCFM)

The prediction from matrix element was calculated using MCFM [2] is used to predict the signal cross section and the background from Z plus b production. MCFM features several processes that contribute to the signal and background. The following are used in this paper:

process 56: $Zc\bar{c}$ production Z strahlung from final state heavy quarks from heavy quark pair production and Z strahlung from initial state quarks with a heavy quark pair production [90]. E.g. Figures 4.1a to 4.1c. This process uses a zero mass approximation for the c quark mass. This approximation requires $m_c \ll p_T$ which does not hold in

the phase space in question.

process 262: Zc production Z strahlung from heavy quarks in the initial state [91], e.g. Figure 4.1d.

process 264: Zc$\bar{c}$ production Same as 56 but with a massive c, e.g. Figures 4.1a to 4.1c. Unlike 56 it can only calculate LO cross sections.

process 267: Zc$\bar{c}$ production Real radiation diagrams that include two final-state charm quarks but without the diagrams of the type shown in Figures 4.1a and 4.1b [91]. Only the real part is used in the calculation. The virtual corrections like Figure 4.1c are already taken into account in 262.

The values calculated are summarised in Table 4.1. The final cross section is calculated in two ways:

$$\sigma^{\dagger}_{1c} = \sigma^{262}_{1c} + \sigma^{267,\texttt{real, incl=F}}_{1c} + \sigma^{264,\texttt{omitgg, incl=F}}_{1c} + \sigma^{264}_{1c} - \sigma^{264,\texttt{incl=F}}_{1c} \quad (4.1)$$

$$\sigma^{\dagger}_{2c} = \sigma^{264}_{2c} \quad (4.2)$$

$$\sigma^{\ddagger}_{1c} = \sigma^{262}_{1c} + \sigma^{267,\texttt{real, incl=F}}_{1c} + \sigma^{56,\texttt{omitgg, incl=F}}_{1c} + \sigma^{56}_{1c} \quad (4.3)$$

$$\sigma^{\ddagger}_{2c} = \sigma^{56}_{2c} \quad (4.4)$$

The two combinations $\sigma^{\dagger}$ and $\sigma^{\ddagger}$ use different approximations. For $\sigma^{\ddagger}$ the c$\bar{c}$ contribution is calculated at NLO with respect to the tree level process for Zc$\bar{c}$ i.e. at NNLO for inclusive Z plus c production neglecting the c mass while for $\sigma^{\dagger}$ the c$\bar{c}$ contribution is calculated at LO with respect to the tree level process for Zc$\bar{c}$ i.e. at NLO for inclusive Z plus c production using a massive c in the calculation. Since there are LO calculations for Zc$\bar{c}$ production available for both the massive and the massless calculations the validity of the massless approximation can be tested using this process. The LO cross section from process 264 is calculated as:

$$\sigma_{1c} = \sigma^{264}_{1c} - \sigma^{264,\texttt{incl=F}}_{1c} \quad (4.5)$$

while the cross section from process 56 is calculated as $\sigma^{56,\texttt{LO}}_{1c}$. The cross section calculated with the massless approximation is 75% higher compared to the massive calculation so this measurement is in a region where the massless approximation doesn't hold. Therefore $\sigma^{\dagger}$ is used to compare the measurement to. The Z $\rightarrow \mu^+\mu^-$is required to be in the fiducial volume of this analysis: $60 < m_{\mu^+\mu^-} < 120$ GeV; $p_{T,\mu} > 20$ GeV and $2 < \eta_{\mu} < 4.5$. The c and $\bar{c}$ are required to satisfy the kinematic properties of the D: $2 < p_{T,c} < 12$ GeV and $2 < y_c < 4$.

process	n_c	σ		PDF	scale	parameter	order
		[fb]					
262	1	803.83	†‡	$^{+43.11}_{-46.40}$	$^{+173.00}_{-102.96}$	`incl=T`	NLO
267	1	−4.85	†‡	$^{+0.6}_{-0.5}$	$^{+1.11}_{-2.00}$	`real, incl=F`	NLO
264	1	100.54	†	$^{+4.83}_{-2.88}$	$^{+25.98}_{-15.17}$	`incl=T, omitgg`	LO
264	1	218.83	†	$^{+6.31}_{-13.62}$	$^{+61.02}_{-46.62}$	`incl=T`	LO
264	1	146.20	†	$^{+6.89}_{-4.99}$	$^{+38.59}_{-25.22}$	`incl=F`	LO
56	1	369.12	‡	$^{+102.94}_{-192.85}$	$^{+95.26}_{-60.86}$		NLO
56	1	35.46	‡	$^{+17.65}_{-25.85}$	$^{+8.45}_{-6.20}$	`incl=F, omitgg`	NLO
56	1	127.69					LO
264	2	78.45	†	$^{+1.61}_{-2.53}$	$^{+22.60}_{-13.46}$		LO
56	2	51.35					LO
56	2	114.37	‡	$^{+14.54}_{-18.85}$	$^{+30.79}_{-11.59}$		NLO
comb†	1	972.15		$^{+41.11}_{-46.78}$	$^{+219.41}_{-138.43}$		
comb‡	1	1203.57		$^{+121.96}_{-217.74}$	$^{+274.75}_{-168.92}$		

Table 4.1: The exact definition of the parameters as a well as of (N)LO can be found in the MCFM manual [91]. (N)LO is not always defined with respect to the Z plus c signal process.

	σ_D [μb]	f	$\mathcal{B}$ [%]
$D^0 \to K^-\pi^+$	620.63	0.56	3.88 ± 0.05
$D^+ \to K^-\pi^+\pi^+$	244.28	0.25	9.13 ± 0.19
$D_s^+ \to (\phi \to K^-K^+)\pi^+$	74.07	0.08	2.28 ± 0.12
$\Lambda_c^+ \to pK^-\pi^+$	179.59	0.09	5.0 ± 1.3

Table 4.2: Ingredients used to calculate the DPS cross section and to convert the Z plus c numbers into Z plus D numbers. For the $Z \to \mu^+\mu^-$cross section $\sigma_Z = 76.7 \pm 1.77 \pm 3.37 \pm 2.77$ pb [69] was used. The inclusive charm cross section $\sigma(D)$ is taken from [92], extrapolated to the fiducial volume of this analysis and quoted irrespective of the decay. The factorisation probability f is taken from [92] and the branching fractions from [10].

To bring the predicted Zc cross section numbers into the context of this measurement the hadronisation and the decay into the considered final states was approximately corrected for. For these corrections any alteration of momentum or rapidity during the hadronisation was neglected. The probability (f) for a c to hadronise into a D was taken from [92]. The branching fraction ($\mathcal{B}$) into the considered final states is taken from [10]. Using these numbers the cross section was calculated as:

$$\sigma_{\text{MCFM,Z D}} = \sigma_{1c} \cdot f \cdot \mathcal{B} + 2 \cdot \sigma_{2c} \cdot f \cdot \mathcal{B} \tag{4.6}$$

where σ_{1c} denotes the cross section with exactly one c in the acceptance and σ_{2c} is the cross section with both the c and the $\bar{\text{c}}$ in the LHCb acceptance. Since there is already a large error from the simplified hadronisation model, correlations between σ_{1c} and σ_{2c} were ignored. Two uncertainties are considered. The first uncertainty originates from the uncertainties on the parton density functions and the second uncertainty is from scale variations. All calculations with MCFM were performed with Version 6.4 and the MSTW08 [93] PDF set.

4.3.2 Double Parton Scattering

I am not aware of a tool that calculates DPS cross sections without assuming the two scatters to be independent. Therefore the naïve factorised description is used [86–89] for double parton scattering:

$$\sigma^{\text{DPS}}_{\text{Z plus D}} = \frac{\sigma_{\text{Z}}\sigma_{\text{D}}}{\sigma_{\text{eff}}} \tag{4.7}$$

where $\sigma_{\text{eff}} = 14.5 \pm 1.7^{+1.7}_{-2.3}$ mb was measured in [94] and $\sigma_{\text{Z}} = 76.7 \pm 1.77 \pm 3.37 \pm 2.77$ pb in [69]. The inclusive cross section numbers for the charmed hadrons (σ_{D}) were taken from a previous measurement of LHCb [95]. Some extrapolation is needed to match the fiducial volume of [95] to the volume used in the analysis at hands. This is described in detail in appendix A.2. The used numbers are summarised in Table 4.2. A prediction for the DPS cross section by an evaluation of Equation 1.45 would be beneficial to compare the DPS model to the the data at hands. This especially applies in the phase space region probed by the measurement presented.

4.3.3 Dimuon Invariant Mass (FEWZ)

In this analysis an accurate description of the Z invariant mass distribution is needed. To account for the contribution of the γ^* to the Z mass peak

Datasets	Year	Version	Int. Luminosity
Main Analysis	2011	Reco 12	1 fb^{-1}
Z Efficiencies and mass shape	2011	Reco 12	1 fb^{-1}
D Efficiencies and mass shapes	2011	Reco 9	355 pb^{-1}
Pileup Studies	2011 & 2012	Reco 14	3 fb^{-1}

Table 4.3: Datasets used in this analysis. The Reco 9 dataset is based on the first 355 pb^{-1} of the same raw data as the Reco 12 dataset. Also the Reco 14 dataset is based an the raw data used for Reco 12 together with the data taken in 2012.

FEWZ [96] is used for the $Z\gamma^* \to \mu^+\mu^-$ invariant mass distribution in the kinematic range considered in this analysis. The mass window was chosen wider to avoid edge effects. FEWZ was run at NNLO with the MSTW08 [93] PDF set and the following phase space selection applied:

- $p_{T,\mu} > 20$ GeV
- $2 < \eta_\mu < 4.5$
- $55 < m_{\mu^+\mu^-} < 125$ GeV

The mass shape was binned in bins of 500 MeV width. This selection matches the fiducial volume of this analysis apart from the invariant mass.

4.4 Selection and Dataset

The analysis is based on the full pp dataset taken in 2011 at $\sqrt{s} = 7$ TeV. The data were reconstructed using Reco 12. Events were selected using the single high p_T muon trigger *i.e.* at least one of the muons from the $Z \to \mu^+\mu^-$ decay has to be triggered on signal (TOS) on all of the following trigger lines:

- `L0Muon`
- `Hlt1SingleMuonHighPTDecision`
- `Hlt2SingleMuonHighPTDecision`

The trigger requires a muon with a transverse momentum $p_{T,\mu} > 10$ GeV in Hlt2 and a SPD multiplicity $n_{\mathrm{SPD}} < 600$ in L0. The offline selection starts from the $W \to \mu\nu_\mu$ stripping line (`StrippingWMuLine`). Other datasets were used for calibration and cross checks. Those are summarised in Table 4.3 as well as in the relevant subsections.

This analysis relies heavily on the efficiencies and purities measured in the previous analyses [40,69,70]. Those relevant for this analysis are summarised in this section.

4.4.1 Selection and Properties of the Z Candidates

The $Z \rightarrow \mu^+\mu^-$selection is taken from [69, 70]. Candidate $Z \rightarrow \mu^+\mu^-$events are selected by requiring a pair of well reconstructed tracks identified as muons; the invariant mass of the two muons must be measured in the range $60 < m_{\mu^+\mu^-} < 120$ GeV. Each muon track must have $p_{T_\mu} > 20$ GeV and lie in the pseudorapidity range $2.0 < \eta_\mu < 4.5$. The relative uncertainty on the momentum measurement is required to be less than 10%. The purity of the Z boson sample was estimated in [69] to be $\rho_Z = 0.997 \pm 0.001$. The main background contribution are semileptonic decays of heavy quarks which were estimated from data.

Since the selection is the same all efficiencies (trigger, muon tracking, muon ID and global event cuts (GEC)) and their uncertainties needed for the cross section determination can be reused from [70]. Those were calculated using Tag and Probe methods on the $Z \rightarrow \mu^+\mu^-$resonance. The analysis relies on the fact that the efficiency of the $\chi^2_{\mathrm{DTF}}/n_{\mathrm{d.o.f}} < 5$ criterion on the Z-D combination is unity. In order for to this to hold on top of the selection in [70] an additional criterion($\chi^2_{\mathrm{DTF}}/n_{\mathrm{d.o.f}} < 5$) is applied on the Z candidate. For details on that see Section 4.4.3. The $\log_{10}(\chi^2_{\mathrm{DTF}}/n_{\mathrm{d.o.f}})$ distribution is shown in Figure 4.2. The efficiency of the $\chi^2_{\mathrm{DTF}}/n_{\mathrm{d.o.f}} < 5$ criterion is measured to be $96.38 \pm 0.08\%$. The region at high $\log_{10}(\chi^2_{\mathrm{DTF}}/n_{\mathrm{d.o.f}})$ was checked and shows a clear Z resonance so it is not dominated by background. These events are Z events with no PV reconstructed or where the PV got lost after the muon tracks were removed. The double peak structure around $\log_{10}(\chi^2_{\mathrm{DTF}}/n_{\mathrm{d.o.f}}) \approx 0$ disappears if the muons are required to have both very high or very both low rapidity.

4.4.2 Charmed Hadron Selection and Properties

The charmed hadron selection is the same as in [40] which uses 355 pb^{-1} of data reconstructed using Reco 9. The main difference is the trigger requirement. In [40] the charmed hadron had to pass the trigger on charm triggers while in this analysis one of the muons from the Z triggers the events. The particle selection efficiencies and mass shapes are well known using $\mathcal{O}(10^6)$ candidates in [40]. This knowledge is reused in this analysis. The efficiencies are shown in Figures 4.4 and 4.5. The efficiencies used in [40] were calculated without any trigger requirement. The change in efficiencies between

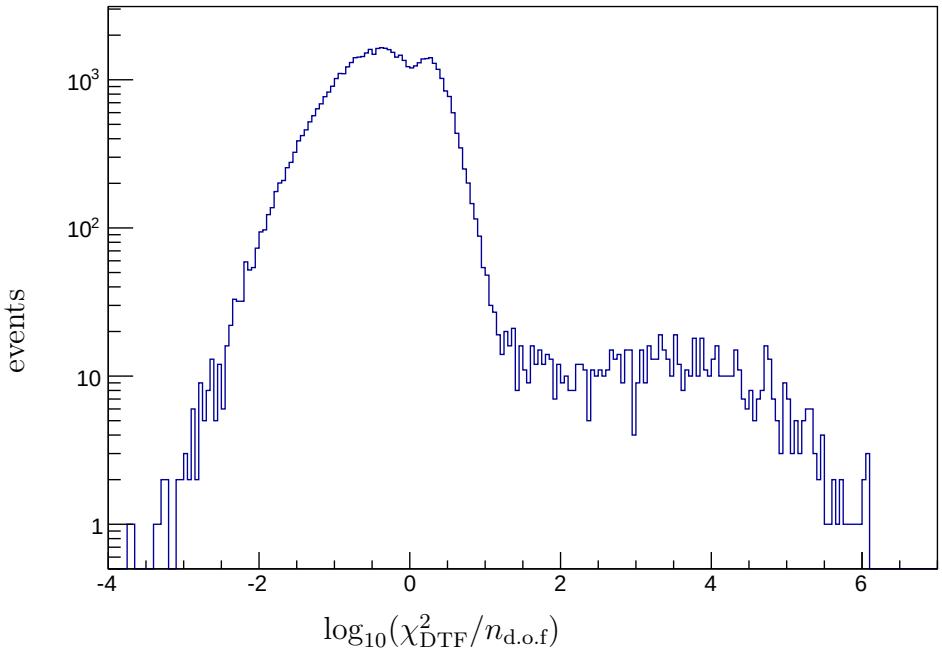

Figure 4.2: $\log_{10}(\chi^2_{\mathrm{DTF}}/n_{\mathrm{d.o.f}})$ distribution for inclusive Z events.

Table 4.4: Selection criteria for charged particles(h) used for the reconstruction of charm hadrons. From [40]

Track selection	
$h^{\pm}$	$\chi^2_{\rm tr}/{\rm ndf} < 5$
$h^{\pm}$	$p^{\rm T} > 250$ MeV/c & $2 < \eta < 5$ & $\chi^2_{\rm IP} > 9$
$\pi^{\pm}, K^{\pm}$	$3.2 < p < 100$ GeV/c
$p^{\pm}$	$10 < p < 100$ GeV/c
Particle identification	
$\pi^{\pm}$	$\Delta \ln \mathcal{L}_{\pi/K} > 2$
$K^{\pm}$	$\Delta \ln \mathcal{L}_{K/\pi} > 2$
$p, \bar{p}$	$\Delta \ln \mathcal{L}_{p/K} > 10$ & $\Delta \ln \mathcal{L}_{p/\pi} > 10$

Reco 9 and Reco 12 is discussed in Section 4.8.1. The selection criteria for the final state hadrons are summarized in Table 4.4. From these selected hadrons the charmed hadrons are combined in the following final states: $D^0 \to K^-\pi^+$, $D^+ \to K^-\pi^+\pi^+$, $D_s^+ \to (K^-K^+)_\Phi\pi^+$ and $\Lambda_c^+ \to pK^-\pi^+$. The selection criteria that are applied to the combined charmed hadron candidates are summarized in Table 4.5. All charmed hadrons are required to have a rapidity $y_{\rm D}$ reconstructed in the range $2 < y_{\rm D} < 4$ and transverse momentum $2 < p_{T,{\rm D}} < 12$ GeV. The invariant mass distributions of the inclusive charmed hadrons without requiring a $Z \to \mu^+\mu^-$candidate are shown in Figure 4.3 (from [40] which used charm triggers instead of muon triggers). The impurity on the inclusive sample has been estimated using simulation to be 1.7% (1.3%,2.6%,4.5%) for D^0 (D^+,D_s^+,Λ_c^+) candidates [95] (Table 3.3). In the fits to the signal shapes these background contributions were accounted for in separate background shapes.

Table 4.5: Criteria used for the selection of charm hadrons.

	D^0	D^+	D_s^+	Λ_c^+
	$K^-\pi^+$	$K^-\pi^+\pi^+$	$(K^+K^-)_\phi\,\pi^+$	$pK^-\pi^+$
y_D	$2 < y_D < 4$	$2 < y_D < 4$	$2 < y_D < 4$	$2 < y_D < 4$
$p^{T,D}$ [GeV]	$2 < p_{T,D} < 12$	$2 < p_{T,D} < 12$	$2 < p_{T,D} < 12$	$2 < p_{T,D} < 12$
χ^2_{VX}	< 9	< 25	< 25	< 25
χ^2_{IP}	< 9	< 9	< 9	< 9
$\frac{\chi^2_{fit}}{ndf}$	< 5	< 5	< 5	< 5
$c\tau$ [μm]	$c\tau > 100$	$c\tau > 100$	$c\tau > 100$	$c\tau > 100$ $c\tau < 500$
m [GeV]	$1.82 < m < 1.92$	$1.82 < m < 1.91$	$1.90 < m < 2.05$	$2.24 < m < 2.325$
m_{KK}[GeV]	—	—	< 1.04	—

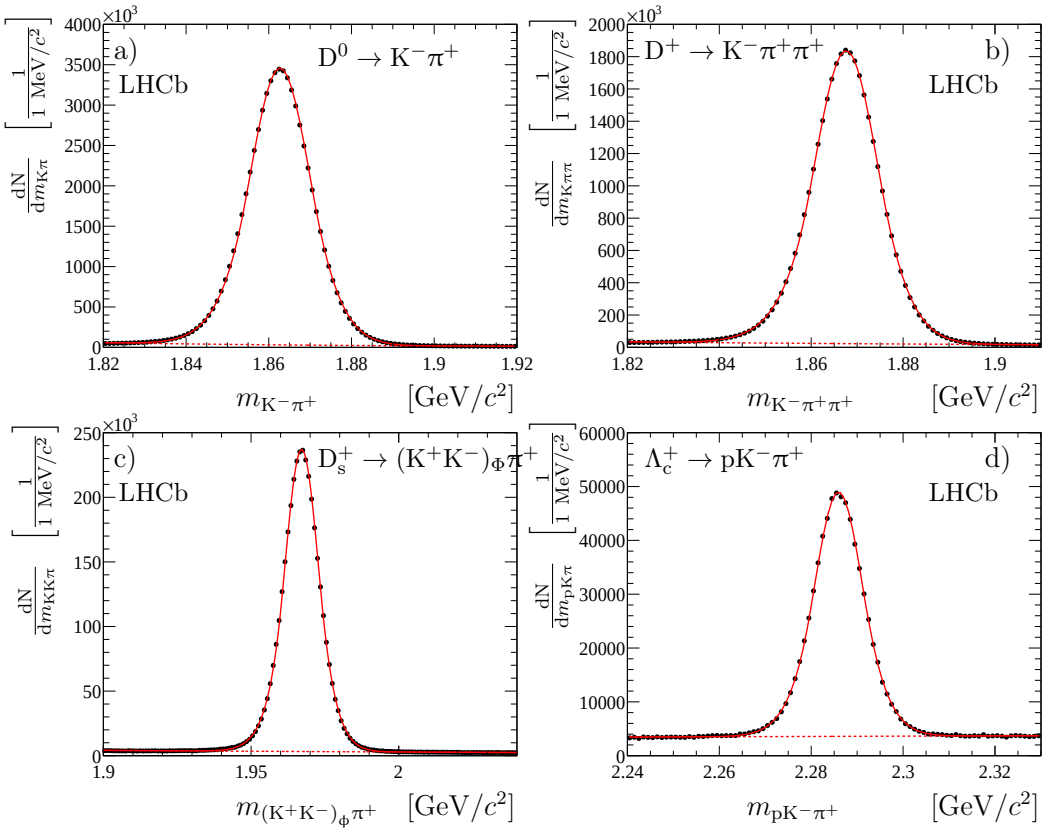

Figure 4.3: Invariant mass distributions for selected a) D^0, b) D^+, c) D_s^+ and d) Λ_c^+ candidates. The solid line corresponds to the total fitted probability density function(PDF) whilst the dotted line shows the background component. The PDF is described in Section 4.7.2. The figure is taken from [40] and therefore uses 355 pb^{-1} of data.

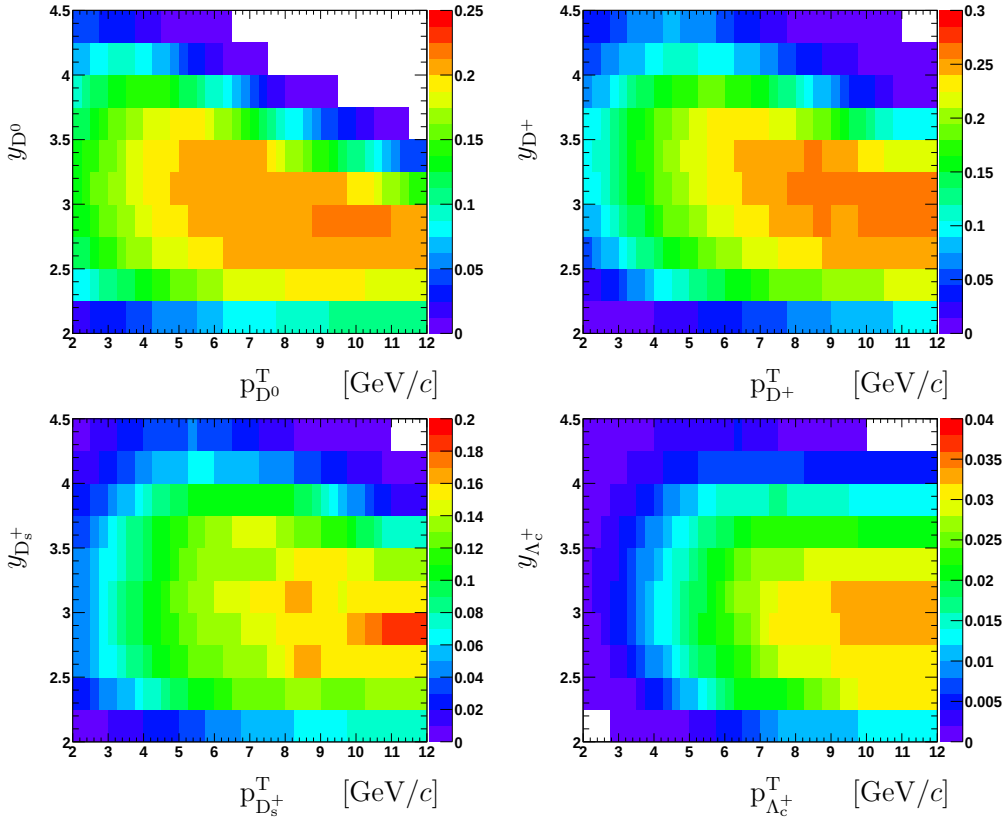

Figure 4.4: The acceptance, reconstruction and selection efficiencies $\varepsilon^{\text{reco}}$ for open charm hadrons: D^0 (top left), D^+ (top right), D_s^+ (bottom left) and Λ_c^+ (bottom right) as functions of particle transverse momentum and rapidity. This is Figure 5.2 in [95].

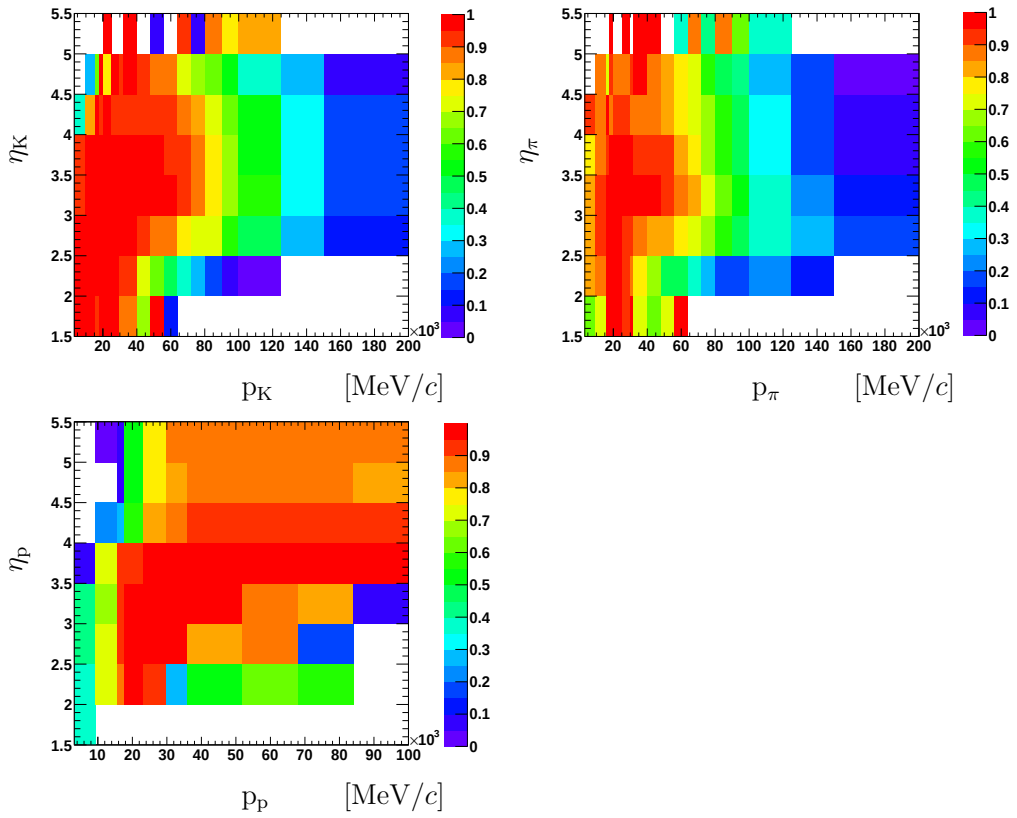

Figure 4.5: The hadron identification efficiencies $\varepsilon^{\mathrm{ID}}_{\pi,\mathrm{K,p}}$, for kaons (top left), pions (top right) and protons (bottom left) as function of particle momentum and pseudorapidity. This is Figure 5.3 in [95].

4.4.3 Combination of Z and Charmed Hadrons

For this analysis the efficiency corrected candidates from [40, 70] are combined. The candidates were fit with the tool `DecayTreeFitter` to the hypothesis that both originate from the same primary vertex (PV) [97]. For the charmed hadrons an extra degree of freedom to allow for a finite flight distance is included in the fit. For the Z $\to\mu^+\mu^-$candidates the muons are required to originate from the PV. The χ^2 of this hypothesis ($\chi^2_{\rm DTF}$) is required to be $\chi^2_{\rm DTF}/n_{\rm d.o.f} < 5$. The efficiency of the $\chi^2_{\rm DTF}/n_{\rm d.o.f} < 5$ on signal is unity by construction as it can be seen form the following approximate calculation: [1]

$$\begin{aligned}
\frac{\chi^2_{\rm Z\ +D,DTF}}{n_{\rm Z\ +D,d.o.f}} &= \frac{\chi^2_{\rm Z,DTF}+\chi^2_{\rm D,DTF}}{n_{\rm Z,d.o.f}+n_{\rm D,d.o.f}} \\
&= \frac{\chi^2_{\rm Z,DTF}}{n_{\rm Z,d.o.f}+n_{\rm D,d.o.f}} + \frac{\chi^2_{\rm D,DTF}}{n_{\rm Z,d.o.f}+n_{\rm D,d.o.f}} \\
&= \frac{\chi^2_{\rm Z,DTF}}{n_{\rm Z,d.o.f}}\frac{n_{\rm Z,d.o.f}}{n_{\rm Z,d.o.f}+n_{\rm D,d.o.f}} + \frac{\chi^2_{\rm D,DTF}}{n_{\rm D,d.o.f}}\frac{n_{\rm D,d.o.f}}{n_{\rm Z,d.o.f}+n_{\rm D,d.o.f}} \\
&\leq 5\frac{n_{\rm Z,d.o.f}}{n_{\rm Z,d.o.f}+n_{\rm D,d.o.f}} + 5\frac{n_{\rm D,d.o.f}}{n_{\rm Z,d.o.f}+n_{\rm D,d.o.f}} = 5 \qquad (4.8)
\end{aligned}$$

Here, temporary extra labels (Z,D,Z +D) are introduced in order to explicitly name the hypothesis this $\chi^2_{\rm NDF}$ and $n_{\rm d.o.f}$ corresponds to.

4.5 Properties of the Selected Candidates

The invariant mass of the Z D combination is shown in Figure 4.6. The individual invariant mass distributions are shown in Figure 4.7. There are no obvious signs for t $\to$Zc. If this exists it might easily be suppressed by the $2 < p_T < 12\,\text{GeV}$ requirement on the D.

More properties of the candidates are given in Table 4.6.

4.6 Background Estimation

An event is considered as signal if the charmed hadron is produced in the same pp interaction as the Z boson. Events where the charmed hadron is

[1] This calculation is exact if the PV position does not change when all tracks used in the candidates are removed. This is a good approximation for the daughters of the charmed hadrons but not necessarily for prompt high momentum muons.

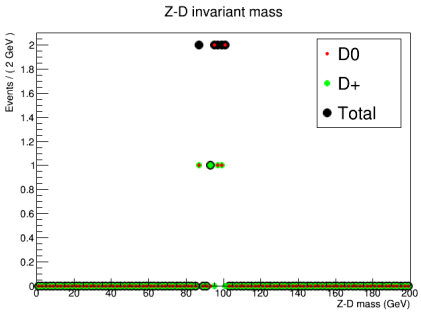

Figure 4.6: Invariant mass of the ZD combination. No events are observes outside the shown range $60 < m_{\mathrm{ZD}} < 120\,\mathrm{GeV}$.

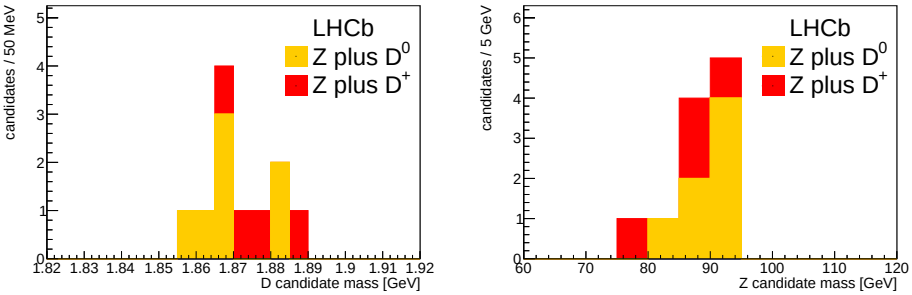

Figure 4.7: Invariant mass of the D (left) and Z (right) candidates.

	m_{D} [GeV]	m_{Z} [GeV]	$p_{T,\mathrm{Z}}$ [GeV]	$p_{T,\mathrm{D}}$ [GeV]	y_{Z}	y_{D}	$\left\|\frac{\Delta\Phi_{\mathrm{ZD}}}{\pi}\right\|$
$\overline{\mathrm{D}}^0$	1.857	90.8	3.31	3.79	2.63	3.88	0.89
D^0	1.88	93.53	20.84	3.25	2.45	3.98	0.9
D^0	1.866	90.17	4.58	2.04	2.79	4.23	0.74
D^0	1.86	81.63	29.52	3.57	3.41	2.94	0.45
$\overline{\mathrm{D}}^0$	1.882	89.54	50.0	2.88	3.28	3.85	0.78
$\overline{\mathrm{D}}^0$	1.867	90.56	36.66	6.9	2.36	3.07	0.88
$\overline{\mathrm{D}}^0$	1.866	89.08	29.5	6.24	2.35	2.68	0.3
D^-	1.876	79.37	7.42	6.65	2.61	3.06	0.03
D^-	1.872	88.22	50.0	5.68	2.8	3.96	0.41
D^+	1.886	88.69	4.53	2.96	2.45	3.08	0.96
D^-	1.869	92.61	2.65	2.73	2.82	3.63	0.71
$\mathrm{D}^-{}_{\to\Phi\pi^-}$	1.869	89.51	4.13	3.27	2.82	3.46	0.05

Table 4.6: Properties of the selected candidates. The $\mathrm{D}^-{}_{\to\Phi\pi^-}$ candidate was not included in the cross section measurement. It would have acquired a very large weight from the low branching fraction $\mathcal{B}(\mathrm{D}^+ \to (\Phi \to \mathrm{K}^+\mathrm{K}^-)\pi^+) = 2.65^{+0.08}_{-0.09} \cdot 10^{-3}$ [10].

produced from a beauty hadron decay are considered as background. Several types of backgrounds are considered:

pileup: Real Z $\rightarrow\mu^+\mu^-$and $D^0 \rightarrow K^-\pi^+$ in the same bunch crossing but in different pp interactions.

combinatorial D: A real Z but a combinatorial D from a random combination of stable hadrons.

combinatorial Z: A real D but a combinatorial Z.

full combinatorial: Background without a real D or Z. This background is estimated from a fit to the invariant mass distributions which is described in Section 4.7.

feed down from b: B $\rightarrow$ D decays from Zb production.

4.6.1 Background from Pileup

The background from pileup was assessed using two methods. The main method is inspired from [40] and uses χ^2_{DTF}. The second method calculates an upper limit by treating every other PV close to the Z $\rightarrow\mu^+\mu^-$ vertex is a potential source of a $D^0 \rightarrow K^-\pi^+$ which may be assigned to the Z.

Pileup Estimation from χ^2_{DTF}

To estimate the contribution from pileup events, where the Z and the charm candidate come from different proton-proton interactions (including two interaction vertices reconstructed as one), the requirement on $\chi^2_{\mathrm{Z\ D,DTF}} < 5$ has been removed, while keeping $\chi^2_{\mathrm{Z,DTF}}/n_{\mathrm{d.o.f}} < 5$ and $\chi^2_{\mathrm{D,DTF}}/n_{\mathrm{d.o.f}} < 5$. For events where the Z and the D come from the same primary vertex one has the following decomposition:

$$\chi^2_{\mathrm{Z\ D,DTF}} = \chi^2_{\mathrm{Z,DTF}} + \chi^2_{\mathrm{D,DTF}} \tag{4.9}$$

This identity is valid modulo some relatively small corrections (of typically of order $\mathcal{O}$ (1) or significantly smaller). These arise since the PV position slightly shifts when the tracks from the Z and the D candidates are removed. Due to the selection criteria, the tracks used for the D-reconstruction have practically no impact on the PV position, but high-p_T muons from Z-decays have a larger effect on the PV-reconstruction.

As shown before in Equation 4.8 $\chi^2_{\mathrm{Z\ D,DTF}}/n_{\mathrm{d.o.f}} < 5$ follows from the selection criteria if Z boson and D meson originate from the same PV.

$$\begin{aligned} p_{T\mathrm{D}} &> 1\,\mathrm{GeV} \\ \Delta \ln \mathcal{L}_{\mathrm{K}/\pi} &> 0 \end{aligned}$$

Table 4.7: Loosend selection criteria.

For events where the Z and the D come from different primary vertices there is also an additional contribution $\chi^2_{\mathrm{VD(PV_Z,PV_D)}}$ for the right part of Equation 4.9, where χ^2_{VD} is the χ^2 of the distance between the two primary vertices. This contribution is large:

$$\chi^2_{\mathrm{VD}}(\mathrm{PV_Z},\mathrm{PV_D}) = \left(\frac{\delta_z}{\sigma_z}\right)^2 + \cdots > \left(\frac{\delta_z}{\sigma_z}\right)^2 \approx \left(\frac{5\ \mathrm{cm}}{0.2\ \mathrm{mm}}\right)^2 = 6.25{\cdot}10^4 \quad (4.10)$$

where δ_z and σ_z are the distance and it's measured uncertainty in the z direction. Therefore it is concluded that all events with $\chi^2_{\mathrm{Z\ D,DTF}}/n_{\mathrm{d.o.f}} > 5$ come from pileup [modulo some small corrections discussed above].

By studying the shape of the $\chi^2_{\mathrm{Z\ D,DTF}}/n_{\mathrm{d.o.f}}$ distribution separately for the region $\chi^2_{\mathrm{Z\ D,DTF}}/n_{\mathrm{d.o.f}} > 5$ one can extract the contribution from pileup and extrapolate it into the signal region with $\chi^2_{\mathrm{Z\ D,DTF}}/n_{\mathrm{d.o.f}} < 5$. This technique has been used in [40] with great success.

The distributions of $\chi^2_{\mathrm{ZD^0,DTF}}/n_{\mathrm{d.o.f}}$ and $\chi^2_{\mathrm{ZD^+,DTF}}/n_{\mathrm{d.o.f}}$ are shown in Figure 4.8. There are no events in the region of large values of $\chi^2_{\mathrm{Z\ D,DTF}}$ where pileup events would be expected (see Equation 4.10). However the very small statistic does not allow to make solid conclusions from these distributions. To esimate the pileup contribution we performed two cross-checks on the full dataset of 3 fb^{-1} taken in 2011 and 2012 reconstructed with Reco 14:

1. We have loosened the selection criteria used for the $\mathrm{D^0}$ and the Z selection to increase the statistics of the sample. The criteria are summarised in Table 4.7. The distribution of $\chi^2_{\mathrm{ZD^0,DTF}}$ for such a loose selection is shown in Figure 4.9(a). In this plot one clearly sees two components: a narrow distribution with $\chi^2_{\mathrm{ZD^0,DTF}}/n_{\mathrm{d.o.f}} < 5$ and a wide structure in the region $\chi^2_{\mathrm{Z\ D,DTF}}/n_{\mathrm{d.o.f}} > 5$. We perform a fit to these distributions using a model that contains two components:

   (a) The component that describes the signal $\mathrm{ZD^0}$ events from the same PV. We expect this component to follow a scaled χ^2-distribution with 7 degrees of freedom. If the Gamma-distribution is interpreted as as a continuous extension of the χ^2-distribution we observe 8.35 ± 1.06 degrees of freedom.

(b) The component that describes pileup. For this component we have also used a Gamma-distribution.

The choice of the shape to describe the pileup contribution is motivated by e.g. [40], where such shapes described the pileup data well. Note that we expect that the major part of $\chi^2_{\mathrm{Z\ D,DTF}}/n_{\mathrm{d.o.f}}$ for a pileup event comes from $\chi^2_{\mathrm{VD}}(\mathrm{PV_Z}, \mathrm{PV_D})$, and this also should follow a scaled χ^2 distribution. It also provides some support for the choice of Gamma-distributions to parametrise the shape of the pileup distributions. It supports also that up to a scaling factor, related to the number of degrees of freedom, the shape of the pileup distribution is process-independent.

The fits of Figure 4.9(a) with the model described above allows to extrapolate the observed pileup events in the $\chi^2_{\mathrm{ZD^0,DTF}}/n_{\mathrm{d.o.f}} > 5$ region to the $\chi^2_{\mathrm{ZD^0,DTF}}/n_{\mathrm{d.o.f}} < 5$ region. $2.8 \pm 0.56\%$ of the events in the signal region are expected to be from pileup.

2. As an additional cross-check of the validity of the Gamma-distribution as a model for pileup, we have performed a study of events with $\mathrm{D^0}$ +track, where $\mathrm{D^0}$ candidates have been selected using loose cuts and "tracks" have been selected as high-p_T tracks in the acceptance of the muon chambers with $20 < p_T < 75$ GeV. Events with $\chi^2_{\mathrm{D^0,DTF}}/n_{\mathrm{d.o.f}} < 5$ and $\chi^2_{\mathrm{"track",DTF}}/n_{\mathrm{d.o.f}} = \chi^2_{\mathrm{"track",IP}}/2 < 5$ are selected. The distribution of $\chi^2_{\mathrm{D^0\ +"track",DTF}}/n_{\mathrm{d.o.f}}$ is shown in Figure 4.9(b). Similar to the distributions discussed above the distribution contains a large statistics peak at small values of $\chi^2_{\mathrm{D^0\ +"track",DTF}}/n_{\mathrm{d.o.f}} < 5$ which corresponds to events where a prompt D and a prompt track form a vertex, and a wide structure at large values of $\chi^2_{\mathrm{D^0\ +"track",DTF}}/n_{\mathrm{d.o.f}}$. Note that for this particular case we also expect some additional contribution from events where the high-p_T tracks come from heavy flavour decays [e.g. bbbar $\rightarrow$ "track" + $\mathrm{D^0}$ + ...]. Here the typical value of χ^2_{DTF} is expected at the level of O(500). Prompt tracks with a $\mathrm{D^0}$ from a b decay also contribute to this final state. To account for these contributions two additional terms (again described by Gamma–distributions) are added into fit.

The high statistics fit of Figure 4.9(b) supports the assumption that the pileup contribution is described well by the Gamma–distribution. The fit parameters for signal, pileup and $\mathrm{b\bar{b}}$-components are well compatible with the expected values.

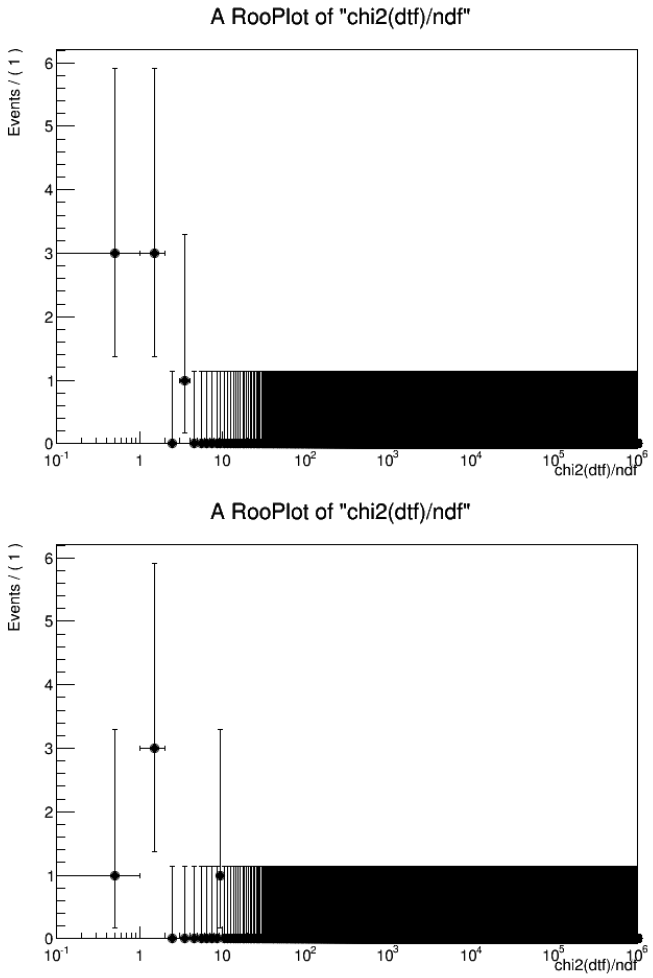

Figure 4.8: χ^2_{DTF} of the Z plus D^0 (top) and Z plus D^+ (bottom) candidates.

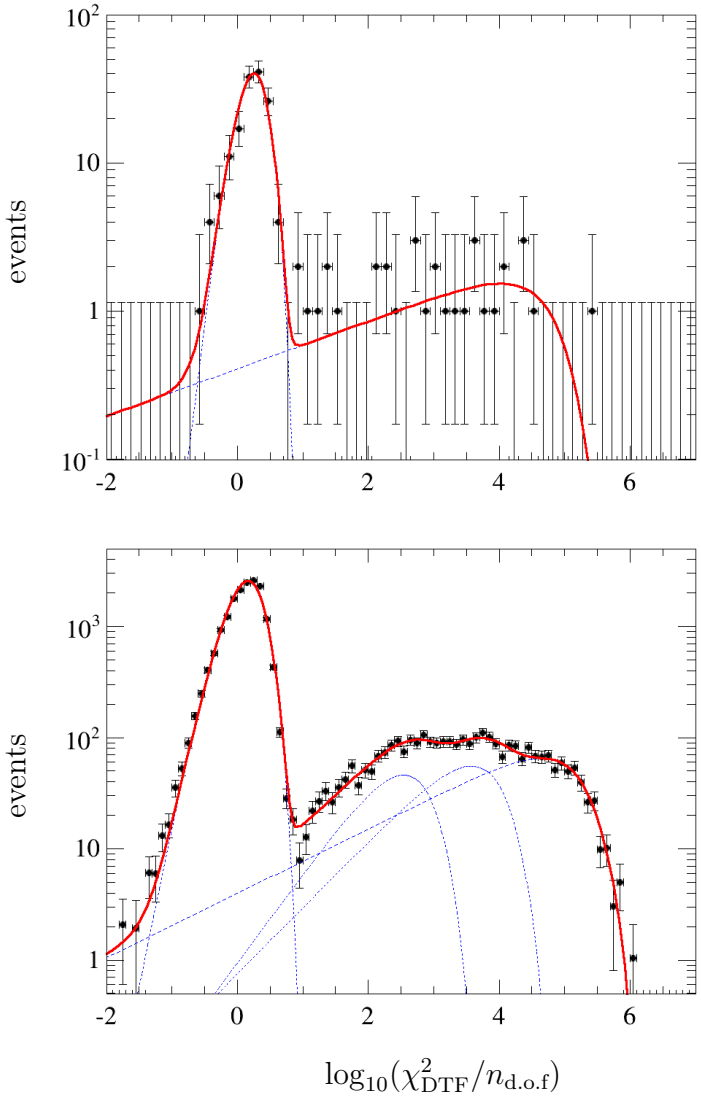

Figure 4.9: $\chi^2_{\rm DTF}$ of the Z plus D^0 (3 fb^{-1} of data taken in 2011-2012) (left) fit with a Gamma-distribution for signal and another for pileup. Track plus D^0 (right) candidates fit with a Gamma-distribution for signal, another for pileup and two more for background from b decays with different topologies.

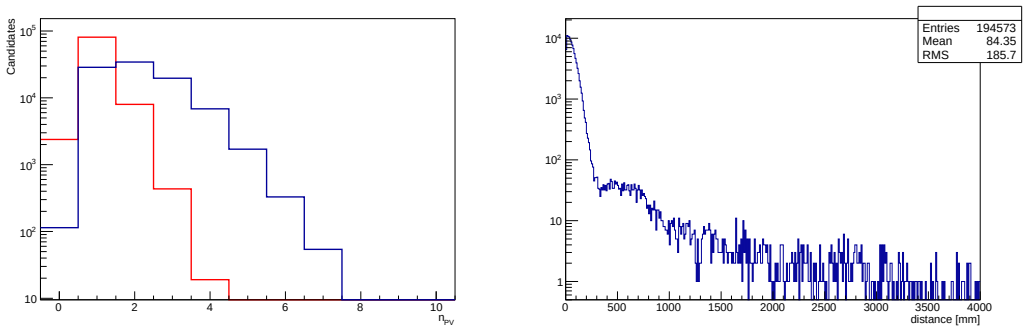

Figure 4.10: Number of primary vertices in Z $\rightarrow\mu^+\mu^-$ events(blue, left). Number of primary vertices closer than 50 mm to the Z $\rightarrow\mu^+\mu^-$ vertex (red, left). Distribution of the distance between the pileup vertices and the Z $\rightarrow\mu^+\mu^-$ vertex(right). The left plot contains the primary vertices from the Z while the right one does not.

Pileup Estimation from Cross Sections and Primary Vertices

An upper limit on the number of background events can also be derived from the number of additional PVs(n_{PV}) in the bunch crossing. The distribution in Z $\rightarrow\mu^+\mu^-$ events is shown in Figure 4.10. There are 103011 additional PVs in the events that contain Z $\rightarrow\mu^+\mu^-$ candidates. The probability for producing a D^0 $\rightarrow\mathrm{K}^-\pi^+$ candidate for any vertex is given by:

$$P = \frac{\varepsilon_{\mathrm{D}^0}}{\varepsilon_{\mathrm{PV}}}\frac{\sigma_{\mathrm{D}^0}}{\sigma_{\mathrm{inel.}}}\mathcal{B}(\mathrm{D}^0 \rightarrow \mathrm{K}^-\pi^+) \tag{4.11}$$

where $\sigma_{\mathrm{D}^0\rightarrow\mathrm{K}^-\pi^+} = 620.63 \pm 8.09\,\mu\mathrm{b}$ [92] is the cross section times branching fraction for D^0 $\rightarrow\mathrm{K}^-\pi^+$ production and $\sigma_{\mathrm{inel.}} = 73.15 \pm 1.26\,\mathrm{mb}$ [98] is the total inelastic cross section. The efficiencies $\varepsilon_{\mathrm{D}^0}$ are $\varepsilon_{\mathrm{PV}}$ the efficiencies to reconstruct a PV and a D^0 respectively.

If the PV reconstruction efficiency, the D^0 $\rightarrow\mathrm{K}^-\pi^+$ efficiency and the different fiducial volume for $\sigma_{\mathrm{D}^0\rightarrow\mathrm{K}^-\pi^+}$ in [92] are neglected the number of D^0 $\rightarrow\mathrm{K}^-\pi^+$ candidates produced in the same bunch crossing is given by:

$$\begin{aligned} n_{\text{pot. pileup}} &= \frac{\varepsilon_{\mathrm{D}^0}}{\varepsilon_{\mathrm{PV}}} P \cdot \left(\sum n_{\mathrm{PV}} - n_{\mathrm{Z}}\right) \\ &= \frac{\varepsilon_{\mathrm{D}^0}}{\varepsilon_{\mathrm{PV}}} 103'011 \cdot \frac{620.63 \pm 8.09\,\mu\mathrm{b}}{73.15 \pm 1.26\,\mathrm{mb}} \cdot (3.88 \pm 0.05)\% = 33.91. \end{aligned} \tag{4.12}$$

Neglecting efficiencies and differences in the fiducial volumes is a conservative estimate since the reconstruction efficiencies for PVs are higher than those for D^0 mesons and the fiducial volume in [92] extents to lower $p_{T\mathrm{D}}$ where the cross section is high. The resolution of Z vertices is of the order $150 - 180$ μm so a

vertex distance $\chi^2 < 5$ roughly corresponds to a distance of 1 mm. To avoid a potential bias from a reduced second PV reconstruction efficiency close to the PV a 1 cm window is used to search for extra PVs and extrapolated linearly to 1 mm. The distribution of the distances between the Z vertex and the pileup PVs is shown in Figure 4.10 (right). From that figure the number of Z events used in the calculation is subtracted in the lowest bin. It can be seen that the assumption that the distribution of pileup vertices stays constant between 1 cm and 1 mm is conservative.

This way the following upper limit on pileup events in Z + D^0 events is derived:

$$n_{\text{pot. pileup,1 cm}} = \frac{\varepsilon_{D^0}}{\varepsilon_{PV}} 8907 \cdot \frac{620.63 \pm 8.09\,\mu b}{73.15 \pm 1.26\,mb} \cdot (3.88 \pm 0.05)\% \leq 2.39$$

$$n_{\text{pot. pileup,1 mm}} = \frac{\varepsilon_{D^0}}{\varepsilon_{PV}} \frac{8907}{10} \cdot \frac{620.63 \pm 8.09\,\mu b}{73.15 \pm 1.26\,mb} \cdot (3.88 \pm 0.05)\% \leq 0.24$$

This results in 0.24 potentially overlapping events. This corresponds to $0.24/7 = 3.4\%$ which agrees nicely with the result estimated in the previous section. It has to be emphasised again that this is a conservatively calculated upper limit and not an estimate of the background.

For the cross section calculation the value from the fits of Figure 4.9(a) is used; $2.8 \pm 0.56\%$ of the events in the signal region are expected to be from pileup.

4.6.2 Combinatorial Background for the Z Candidates

The fraction of combinatorial background in events with associated production of $Z \to \mu^+\mu^-$ with c–hadrons is assumed to be equal to the fraction of background in events of associated production of $Z \to \mu^+\mu^-$ with jets [2]. For Z plus jets the impurity in $Z \to \mu^+\mu^-$ plus jets events was estimated by comparing the invariant mass distribution of $Z \to \mu^+\mu^-$in events with jets to inclusive $Z \to \mu^+\mu^-$events to be 3.1 ± 0.6‰ [99]. This comparison is shown in Figure 4.11(a,b).

Since this background is small, no additional fit shape is introduced into the fit model. Instead the small background contribution is corrected by a purity factor.

As a cross check this background is included in the fit model with the normalisation and the slope as free parameters. The additional background is then found to be consistent with zero.

[2] Anti $k_T, R = 0.5, p_T > 10$ GeV jets.

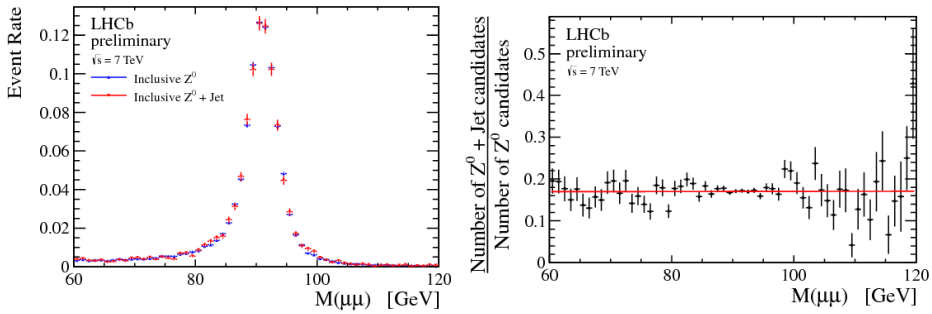

Figure 4.11: The left plot shows the dimuon mass spectrum in data, for Z + jet events (blue) and all Z events (red) scaled to the same integral (unity) and overlaid. The right plot show the ratio of the number of Z events to the number of Z + jet events seen as a function of the dimuon invariant mass. A straight line fit, $p_0 + p_1 \cdot m_{\mu^+\mu^-}$ returns $p_0 = 0.17 \pm 0.02$ and $p_1 = (1 \pm 22) \cdot 10^{-5}$. These distributions are not corrected for any inefficiencies in Z or jet detection. (From [99].)

4.6.3 Background with Real Z and Combinatorial D

The combinatorial background in inclusive charm events was estimated in [40, 95] to be 1.7% (1.3%,2.6%,4.5%) for D^0 (D^+,D_s^+,Λ_c^+) candidates. Since the events analysed in the analysis at hand have much higher Q^2 compared to the inclusive charm production studied in [40, 95], the assumption that the background remains constant is not justified. Therefore this background has to be determined directly for the Z plus D sample. This is done using a two dimensional fit in $m_{K\pi} : m_{\mu^+\mu^-}$ with the fit models described in Section 4.7.

4.6.4 Feed Down from Beauty Hadrons

As for the Zc signal there are two mechanisms that lead to Zb background production: Double Parton Scattering and Single Parton Scattering.

Double Parton Scattering

The contamination from beauty hadron decays was estimated from simulation for [40] in [95] to be 1.7%, 1.3%, 2.6%, 4.5% for D^0, D^+, D_s^+, Λ_c^+. In the DPS paradigm the process producing the b or c–quark is more or less independent of the Z production and therefore the spectra and values don't change. If factorisation is assumed, the processes are indeed independent. In a more realistic description of the four parton phase space the effective $\sqrt{s}$ for b or c–quark production is biased downwards from sum rules on Bjorken–x: $x_{b1} + x_{Z1} \leq 1$ and $x_{b2} + x_{Z2} \leq 1$ where x_{pi} denotes the Bjorken–x of the parton from beam i producing the particle p. This is not a small correction

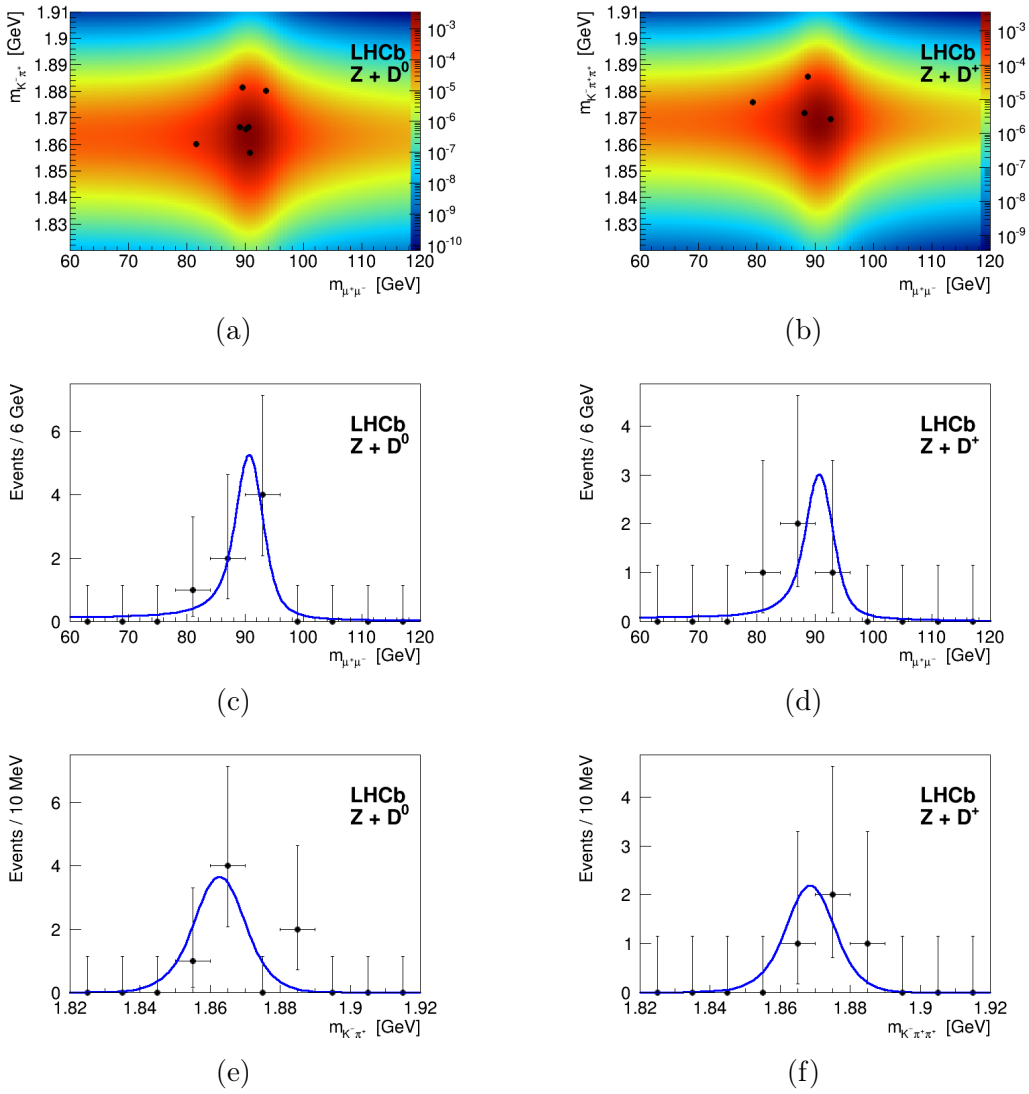

Figure 4.12: Invariant mass of the Z plus D^0 (left) and Z plus D^+ (right) candidates compared to the baseline fit described Section 4.7.

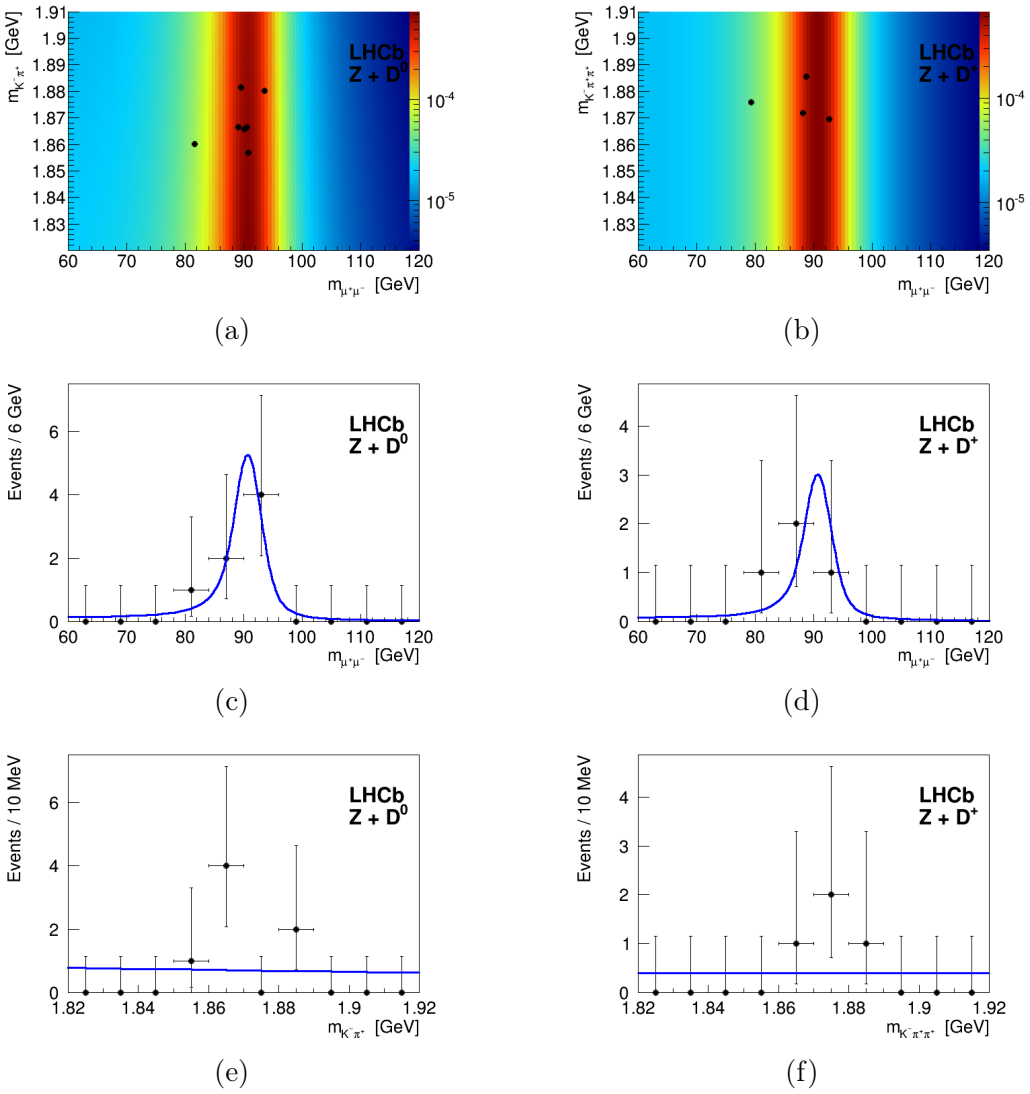

Figure 4.13: Invariant mass of the ZD^0 (left) and ZD^+ (right) candidates fit with a model that was constrained to have zero Z D candidates.

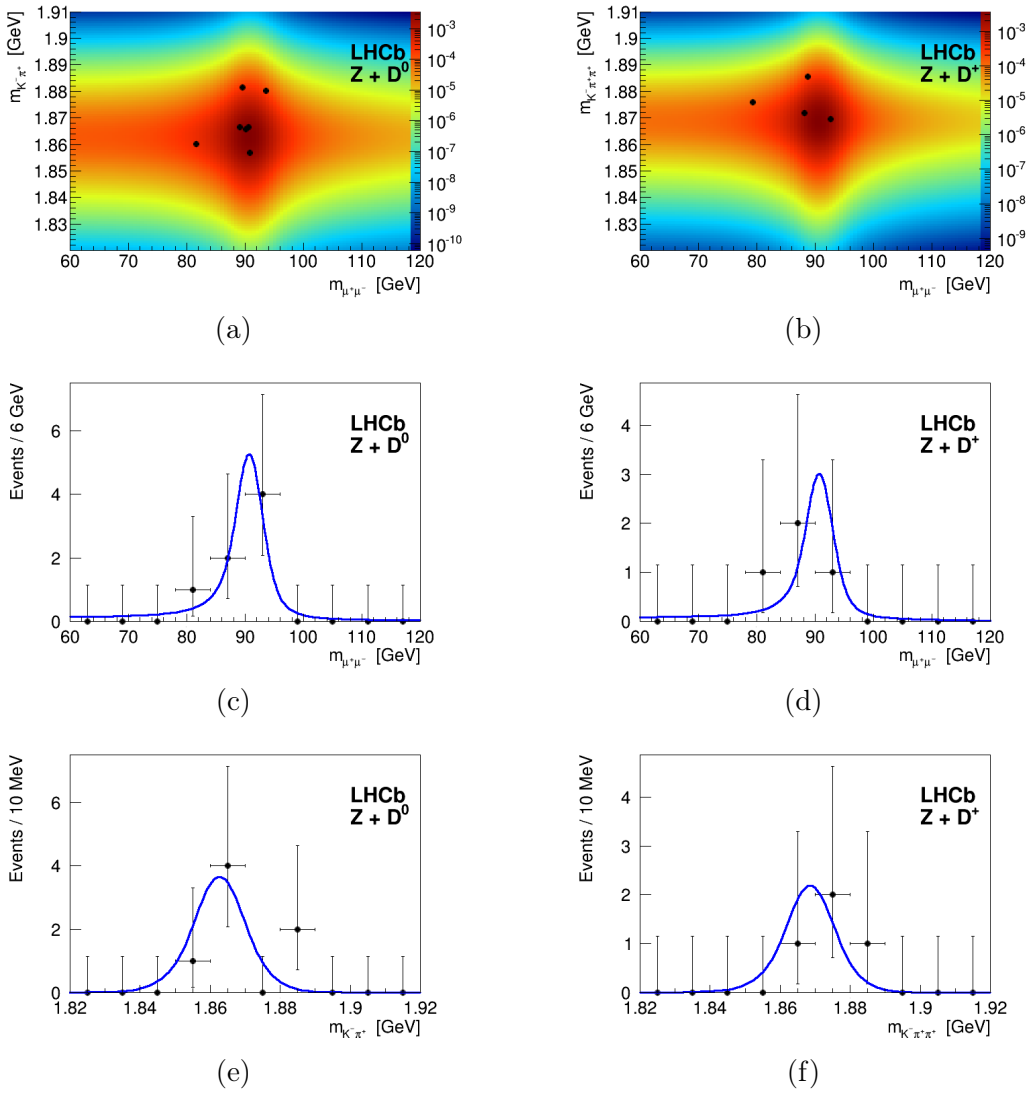

Figure 4.14: Invariant mass of the Z plus D^0 (left) and Z plus D^+ (right) candidates fit with a flat background model. Note that the flat background does not change the shape of the contours.

since $x_{\mathrm{Z1}} = \frac{m_{\mathrm{Z}}}{\sqrt{s}} \exp(y)$ is rather large at LHCb. This reduces the phase space available for beauty quarks to be produced and therefore using the numbers from [40] is a conservative estimate.

Single Parton Scattering

For SPS we use the cross section ratio as determined with MCFM [2] (See Section 4.3.1). This leads to a suppression factor of approximately: [3]

$$\frac{\sigma_{\mathrm{Z+bj(261)}}}{\sigma_{\mathrm{Z+cj(262)}}} = (79.5^{+6.0}_{-6.9}\ (\mathrm{PDF})^{+14.0}_{-14.6}\ (\mathrm{scale}))\%. \tag{4.13}$$

A possible contribution from b decays to the background in Z+D^0 is further suppressed by the branching fraction $\mathcal{B}$ ($\mathrm{B}^0/\mathrm{B}^+$/b-baryon admixture $\rightarrow \mathrm{D}^0$) = 59% [10] and the selection criteria for the D. The suppression is even stronger for D^+:$\mathcal{B}$ ($\mathrm{B}^0/\mathrm{B}^+$/b-baryon admixture $\rightarrow \mathrm{D}^+$) = 23% [10]. The $\chi^2_{\mathrm{DTF}} < 5$ criterion is implicitly a requirement on IP_{D} and therefore selects mainly prompt Ds. This leads to an additional suppression factor of about 5-7. So the background from feed down is conservatively estimated to be $\approx 79.5\% \cdot 59\%/5 = 9.4\%(3.7\%)$ for D^0 (D^+) produced in SPS.

Combination of DPS and SPS

The comparison of the measured cross section to MCFM suggests (see Section 4.9) that the cross section is dominated by DPS. Therefore the b induced background is expected to be dominated by DPS as well. A quantitative estimate of the fractions is not possible because there is no theory prediction for the DPS part of the cross section available that takes into account the correlations among the partons. Since the individual contributions to feed-down from Z plus a b quark from DPS and SPS are unknown, we assume that the contamination from b-quark decays is dominated by DPS. This assumption is in line with the theoretical predictions for Z plus charm quark production shown in Table 4.10 and leads to a background estimate of 1.7%(1.3%). Since the contribution from SPS is not known an uncertainty is assigned that corresponds to the assumption that not more than half of the events originate from SPS. This leads to an uncertainty of $(9.4\% - 1.7\%)/2 = 3.85\%$ for D^0 and $(3.4\% - 1.3\%)/2 = 1.05\%$ for D^+.

[3] The errors have been calculated using naïve error propagation. No possible cancellation of errors was considered. Instead of a full calculation for the Zb cross section this comparison was performed only on the Z strahlung processes in MCFM(261(b quark) and 262(c quark)).

parameter	value from fit
μ	-0.022 $\pm$ 0.018 GeV
σ	1.671 $\pm$ 0.022 GeV
α	1.57 $\pm$ 0.04
n	1.73 $\pm$ 0.08

Table 4.8: Parameters obtained for the Crystal Ball function used to simulate the detector resolution and FSR effects in the Z $\rightarrow\mu^+\mu^-$mass distribution.

4.7 Fit and Determination of the Cross Sections

The signal purity is extracted from a simultaneous fit to m_{D} and m_{Z}. This part of the purity takes into account combinatorial background.

4.7.1 Z $\rightarrow\mu^+\mu^-$ Fit Model

The mass shape for Z $\rightarrow\mu^+\mu^-$was taken from FEWZ [96]. Since FEWZ does not contain any detector resolution effects or final state radiation (FSR) the distribution was convoluted with a Crystal Ball function [100]. The parameters for the Crystal Ball function were obtained by a fit to the measured mass distribution obtained in [70]. The fit together with the measured mass distribution without requiring c–hadrons is shown in Figure 4.15. The parameters of the Crystal Ball function are listed in Table 4.8. These parameters are fixed for the fit of the Z plus D distributions. There is good agreement between data and the resolution corrected FEWZ model. Therefore no additional background PDF is introduced for the baseline analysis. An exponential is used to test whether there is additional background present.

Convolution of the FEWZ distribution with a Gaussian only does not lead to a good description of the radiative tail, as can be seen in Figure 4.15(right).

4.7.2 Fit Model for Charmed Hadrons

The fit model for the c–hadrons is taken from [40, 95] (Table E.1). The invariant mass was fit with a Bukin function (appendix E in [95]) to the first 355 pb^{-1} of the data used in the analysis at hand. The Bukin function is a modified Novosibirsk function [101]. The background model is an exponential. The parameter of the Bukin function are given in Table 4.9 and the result of the fit is shown in Fig. 4.3.

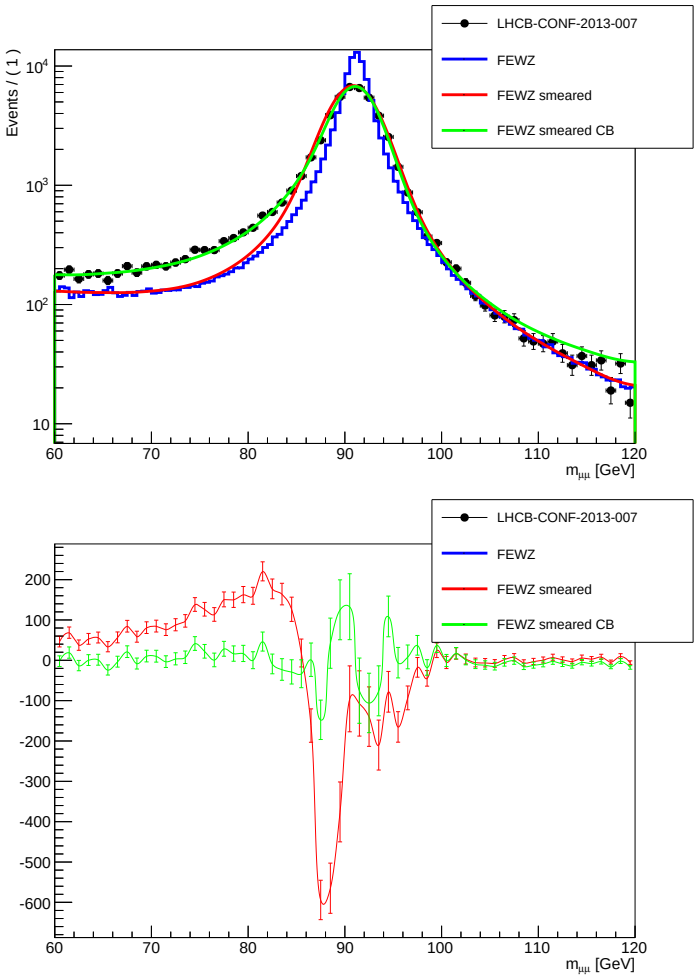

Figure 4.15: $Z \rightarrow \mu^+\mu^-$ invariant mass distribution compared to FEWZ (left). A Gaussian and a Crystal Ball resolution model were fit to the data. The Crystal Ball shape also describes FSR. It's clearly visible in the residual plot on the right side that the Gaussian resolution model fails to describe the radiative tail of the distribution.

Table 4.9: The parameters of the Bukin function obtained from the fit of the inclusive D^0, D^+, D_s^+ and Λ_c^+ signals. From Table E.1 in [95].

	D^0	D^+	D_s^+	Λ_c^+
m_0	1.8627	1.8676	1.9671	2.2860
σ_m	7.30	6.93	5.75	5.33
ξ [%]	-0.04 ± 0.01	-0.02 ± 0.01	-0.06 ± 0.05	0.18 ± 0.13
ρ_L	-0.171	-0.108	-0.093	-0.183
ρ_R	-0.290	-0.284	-0.186	-0.240

4.7.3 Two Dimensional Fit Shapes

The fit model is based on four fit shapes:

$s_D s_Z$: In this shape the two peaking mass shapes are combined. This has only the normalisation ($n_{s_D s_Z}$) as free parameter.

$s_D b_Z$: Has a signal shape for D in the hadron invariant mass and an exponential for the $\mu^+\mu^-$ invariant mass. The normalisation of this shape is set to zero in the baseline analysis. If allowed in the fit it has the normalisation ($n_{s_D b_Z}$) and the slope (τ_1) as free parameters.

$b_D s_Z$: Has a signal shape for Z in the $\mu^+\mu^-$ invariant mass and an exponential for the hadron invariant mass. It adds $n_{b_D s_Z}$ and τ_2 to the parameter set.

$b_D b_Z$: Here two more exponentials with independent slopes are used with three extra parameters $n_{b_D b_Z}, \tau_A$ and τ_B for the normalisation and the two slopes.

All parameters of the Bukin functions and the resolution model were fixed on the high statistics samples.

There were three fits performed:

baseline: Allowed $s_D s_Z$, $b_D s_Z$ and $b_D b_Z$ to float while $s_D b_Z$ is set to zero.

flat background: Same as baseline but with vanishing slopes of all exponentials.

Z background cross check: All four shapes are allowed to float.

background only: Allowed $s_D b_Z$, $b_D s_Z$ and $b_D b_Z$ to float, $s_D s_Z$ is constrained to zero.

All fit results are shown in Tables A.1, A.3, A.5, A.7, A.9 A.11, A.13, A.14, A.15 and A.16

The purity of the samples is calculated as:

$$\rho = \rho_{\mathrm{Z}} \cdot \frac{n_{\mathrm{s_D s_Z}}}{n_{Events}}. \tag{4.14}$$

4.7.4 Cross Section Determination

The cross section is calculated as:

$$\sigma = \frac{\rho}{\int \mathcal{L}} \sum_{\mathrm{Events}} \frac{1}{\epsilon} \tag{4.15}$$

were ϵ denotes the efficiency of measuring this event based on geometrical and kinematic properties of the measured particles. This includes trigger, tracking, particle identification and other reconstruction related efficiencies. The momentum selection on the bachelor hadrons is accounted for in the efficiency numbers. Details can be found in [40, 69, 70]. It does not correct for the kinematic selection of the Z and the D since this would introduce a large model dependence into this measurement.

The statistical uncertainty is calculated in the Gaussian approximation as

$$\sigma_\sigma = \rho \sqrt{\sum_{\mathrm{Events}} \frac{1}{\epsilon^2}} \tag{4.16}$$

The uncertainty on ρ_{fit} is dominated by statistics. This is not assigned as systematic uncertainty to the measurement since it is already in the statistical uncertainty of the cross section. The systematic from the fit models is taken as the difference between the exponential and the flat background models. The difference is very small -0.00015 events for D^0 and -0.004 for D^+ and is therefore neglected.

4.8 Systematic Uncertainties

The systematic uncertainties are expected to be small with respect to the statistical uncertainties. The systematic uncertainties are only calculated for the final states were an quantitative result is quoted. These are ZD^0 and ZD^+. The following systematic uncertainties were considered in this analysis:

Efficiencies: Where available the trigger and reconstruction efficiencies were taken from [40, 69]. Also the uncertainties stated in these documents

were assigned to the cross section measurements. Those uncertainties of 4.5% (1.5%) mainly originate from limited statistics in the control channels. The calculation is described in the following sections.

Different Reco Versions The data – MC correction factors for MC11–Reco12 were applied instead of the baseline correction. The difference of about 1% is assigned as systematic uncertainty.

$\chi^2_{\mathrm{DTF}}/n_{\mathrm{d.o.f}} < 5$ on Z: The efficiency for the $\chi^2_{\mathrm{DTF}}/n_{\mathrm{d.o.f}} < 5$ criterion on the Z was evaluated for this analysis. The statistical uncertainty of this estimate of 0.08% is taken as systematic for the cross section.

pileup The pileup contamination is calculated to be $2.8 \pm 0.6\%$. This uncertainty is assigned as systematic uncertainty.

signal yield The purities returned from the baseline fit and the flat background model were compared. The difference of $\mathcal{O}(10^{-4})$ is neglected.

Z purity The impurity in the Z selection $3.1 \pm 0.6‰$. The uncertainty on the Z purity was determined in [99]. The Z sample is potentially cleaner with respect to to [69, 99] since the $\chi^2_{\mathrm{DTF}}/n_{\mathrm{d.o.f}} < 5$ on Z requirement potentially removed background from semileptonic heavy flavour decays. This effect must be small since the purity is very high already and cannot exceed unity. It is therefore neglected. Also a potential enrichment in background from the combination of a $\mathrm{b} \to \mathrm{D}\ \mu$ with an additional muon in the event is neglected. This background is also suppressed by the selection of the D which favours prompt D mesons.

Feed down from beauty hadrons The feed down from b decays was estimated with a precision of 3.85% (1.05%) for Z plus D^0 (D^+). This is assigned as systematic uncertainty.

4.8.1 Uncertainties on the Efficiencies

The uncertainties on the efficiencies are propagated by varying the efficiencies ten thousand times within their uncertainties and taking the standard deviation of this as uncertainty on the event yield. In addition, to account for the uncertainty on the efficiencies in the signal phase space that is not probed by the observed events, the kinematic properties of the $\mathrm{Z} \to \mu^+\mu^-$candidates were smeared. In total the estimated uncertainty due to efficiencies corresponds to 6.8 % (5.0 %).

As a cross check the following formula was used to propagate the uncertainties on the efficiencies to the yield (y).

$$\begin{aligned} 2\sigma_y &= \sum_{\text{events}} \frac{1}{\varepsilon_{\mathrm{D}} - \sigma_{\varepsilon_{\mathrm{D}}}} \frac{1}{\varepsilon_{\mathrm{Z}} - \sigma_{\varepsilon_{\mathrm{Z}}}} \\ &- \sum_{\text{events}} \frac{1}{\varepsilon_{\mathrm{D}} + \sigma_{\varepsilon_{\mathrm{D}}}} \frac{1}{\varepsilon_{\mathrm{Z}} + \sigma_{\varepsilon_{\mathrm{Z}}}} \end{aligned} \tag{4.17}$$

Here ε_{D}, ε_{Z} denote the efficiency to reconstruct a D, Z candidate where the latter also contains the trigger and GEC efficiency.

The observed yields with the reconstruction uncertainties are (100.089 ± 6.459) and (41.3491 ± 1.57915) for the Z plus D^0 and D^+ samples. This corresponds to an uncertainty of 6.5% and 3.8%. As expected these values are slightly higher than the values obtained with the random variations as all uncertainties are varied correlated. The numbers from the random variations were used for the final result.

Additional Uncertainties from Different Reconstruction Versions

The charm efficiency values were originally calculated for [40] which uses Reco 9. The analysis at hands uses Reco 12. To account for the difference the MC correction factors for MC11 and Reco12 provided by the tracking group were used to correct the cross section instead of the ones for Reco9 and MC 11 in the baseline analysis. The difference is assigned as systematic uncertainty and accounts for the tracking efficiency related differences between these reconstruction versions. The relative uncertainties $r = \left\| \frac{y_{\text{baseline}} - y_{\text{varied}}}{y_{\text{baseline}}} \right\|$ found are: 1% and 0.5% for the Z plus D^0 and D^+ samples.

4.9 Results

The cross section for associated production of $\mathrm{Z} \to \mu^+\mu^-$and c–hadrons is measured to be:

$$\begin{aligned} \sigma_{\mathrm{Z}\to\mu\mu,\mathrm{D}^0\to\mathrm{K}^-\pi^+} &= 97.1 \pm 43.4\ (\text{stat}) \pm 10.0\ (\text{syst}) \pm 3.4\,(\text{lumi})\,\text{fb} \\ \sigma_{\mathrm{Z}\to\mu\mu,\mathrm{D}^+\to\mathrm{K}^-\pi^+\pi^+} &= 40.3 \pm 20.6\ (\text{stat}) \pm 3.4\ (\text{syst}) \pm 1.4\,(\text{lumi})\,\text{fb} \end{aligned}$$

Division by the branching fractions $\mathcal{B}$ ($\mathrm{D}^0 \to \mathrm{K}^-\pi^+$) and $\mathcal{B}$ ($\mathrm{D}^+ \to \mathrm{K}^-\pi^+\pi^+$) yields:

$$\begin{aligned} \sigma_{\mathrm{Z}\to\mu\mu\mathrm{D}^0} &= 2.50 \pm 1.12 \pm 0.22\,\text{pb} \\ \sigma_{\mathrm{Z}\to\mu\mu\mathrm{D}^+} &= 0.44 \pm 0.23 \pm 0.03\,\text{pb}, \end{aligned}$$

where the first uncertainty is statistical and the second systematic. These cross sections correspond to the following fiducial region:

	Measured				MCFM massless					MCFM massive					DPS			
	[fb]	syst	stat	lumi	[fb]	PDF	scale	hadr	tot	[fb]	PDF	scale	hadr	tot	[fb]	σ_{incl}	σ_{eff}	tot
D^0	97	$^{+10}_{-10}$	$^{+43}_{-43}$	$^{+3}_{-3}$	33	$^{+4}_{-3}$	$^{+4}_{-7}$	$^{+2}_{-2}$	$^{+7}_{-7}$	24.8	$^{+0.2}_{-0.1}$	$^{+3.1}_{-4.9}$	$^{+1.4}_{-1.4}$	$^{+3.4}_{-5.1}$	64	$^{+4}_{-4}$	$^{+13}_{-11}$	$^{+13}_{-11}$
D^+	40	$^{+3}_{-3}$	$^{+21}_{-21}$	$^{+1}_{-1}$	34	$^{+5}_{-3}$	$^{+5}_{-7}$	$^{+3}_{-3}$	$^{+7}_{-8}$	25.4	$^{+0.2}_{-0.1}$	$^{+3.2}_{-5.0}$	$^{+2.1}_{-2.1}$	$^{+3.8}_{-5.5}$	59	$^{+4}_{-4}$	$^{+12}_{-10}$	$^{+12}_{-11}$
D_s^+		—			2.7	$^{+0.4}_{-0.2}$	$^{+0.4}_{-0.5}$	$^{+0.6}_{-0.6}$	$^{+0.8}_{-0.8}$	2.06	$^{+0.02}_{-0.01}$	$^{+0.26}_{-0.41}$	$^{+0.45}_{-0.45}$	$^{+0.52}_{-0.61}$	4.5	$^{+0.6}_{-0.6}$	$^{+0.9}_{-0.7}$	$^{+1.1}_{-0.9}$
Λ_c^+		—			7.0	$^{+1.0}_{-0.6}$	$^{+1.0}_{-1.4}$	$^{+2.8}_{-2.8}$	$^{+3.1}_{-3.1}$	5.31	$^{+0.04}_{-0.03}$	$^{+0.66}_{-1.05}$	$^{+2.08}_{-2.08}$	$^{+2.18}_{-2.33}$	24	$^{+6}_{-6}$	$^{+5}_{-4}$	$^{+8}_{-7}$

Table 4.10: Comparison of the measured cross sections and the theory predictions together with the parameters used in the cross section calculation. All cross section numbers are cross sections to to full final states i.e. $Z \to \mu^+\mu^- + D^0 \to K^-\pi^+$ and not corrected for branching fractions unless this is stated otherwise. The correction factors are tabulated in Table 4.2.

- $60 < m_{\mu^+\mu^-} < 120\,\text{GeV}$,
- $p_T(\mu^\pm) > 20\,\text{GeV}$,
- $2 < \eta(\mu^\pm) < 4.5$,
- $2 < p_T(D) < 12\,\text{GeV}$ and
- $2 < y(D) < 4$.

No $\Lambda_c^+ \to pK^-\pi^+$ or $D_s^+ \to \phi\pi^+$ was observed in association with a $Z \to \mu^+\mu^-$ which is expected due to the lower reconstruction efficiency for Λ_c^+ in LHCb and the lower cross section for D_s^+ production.

Three theory predictions were calculated for this processes. DPS from Equation 4.7 and a massive and a massless SPS predictions from MCFM. For the associative production of Z bosons and D^0 mesons the sum of DPS and SPS contributions is consistent with the measured cross section within the large uncertainties from both theory and experiment, while for ZD^+ case, the measured cross section lies below the expectations.

A graphical comparison to the available theory predictions is presented in Fig. 4.16 and the values are given in tables 4.10 and 4.11. The cross section corrected to c-quark level shown in Fig. 4.16c suggests that $Z + D^0$ is fluctuated upwards and $Z + D^+$ has fluctuated downwards and is consistent with one common Z +c cross section.

If oscillations between D^0 and $\overline{D}^0$, and the Double Cabibbo suppressed mode $D^0 \to K^+\pi^-$ are neglected, these modes also allow to determine whether a c or a $\bar{c}$ was produced. Four candidates contain a c quark and seven candidates contain a $\bar{c}$. The probability to measure $\|A\| = \left\|\frac{n_c - n_{\bar{c}}}{n_c + n_{\bar{c}}}\right\| \geq 27.3\%$

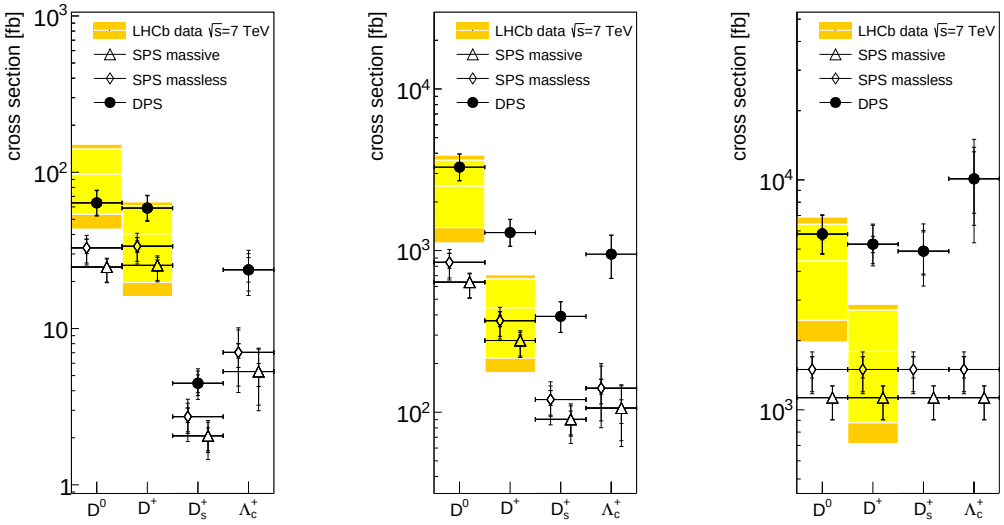

(a) Cross Section times branching fraction as measured.

(b) Cross Section corrected for branching fraction. As published.

(c) Cross Section corrected for branching fraction as well as for factorisation from c →c-hadron.

Figure 4.16: Graphical comparison to theory predictions. The numbers are shown in Tables 4.1, 4.2, 4.10 and 4.11.

	measured	MCFM massless	MCFM massive	DPS
ZD^0	$2.50 \pm 1.12 \pm 0.22$	$0.85^{+0.12\ +0.11}_{-0.07\ -0.17} \pm 0.05$	$0.64^{+0.01\ +0.08}_{-0.01\ -0.13} \pm 0.04$	$3.28^{+0.68}_{-0.58}$
ZD^+	$0.44 \pm 0.23 \pm 0.03$	$0.37^{+0.05\ +0.05}_{-0.03\ -0.07} \pm 0.03$	$0.28^{+0.01\ +0.04}_{-0.01\ -0.06} \pm 0.02$	$1.29^{+0.27}_{-0.23}$

Table 4.11: Comparison of the measured cross sections [pb] and the theoretical predictions for the associated production of a Z boson with an open charm meson. For the measured cross section the first uncertainty is statistical and the second systematic. For MCFM the first uncertainty is related to the uncertainties of the parton distribution functions, the second is the scale uncertainty and the third due to uncertainties associated with c-quark hadronisation as discussed in the text.

if n_{c} and $n_{\overline{\mathrm{c}}}$ follow a Poisson distribution of mean 5.5 is 40% so there is no significant c–$\overline{\mathrm{c}}$ asymmetry observed.

4.9.1 Intrinsic Charm

A possible dominance of the intrinsic charm mechanism [30] has been studied by investigating the p_T-spectrum of the D^0-candidates. If the IC mechanism was dominant, one would expect a very hard p_T-spectrum up to $p_{T,\mathrm{D}^0} = 35 - 40$ GeV [102]. We have studied the full data set (2011 and 2012) with released fiducial volume and particle identification cuts and the highest pt(D^0) found in (ZD^0) events was found to carry a $p_T \approx 11$ GeV. This does not provide support for a large contribution from the IC mechanism.

4.10 Significance of the Signal

Based on the signal PDFs introduced above the significance of the observation is assessed using toy experiments.

First, the measured events were fit with the hypothesis of zero Z plus D^0 events. The number of pure Z events and pure D^0 events was left floating. This distribution is shown in Fig. 4.13.

From this distribution events were sampled. Three scenarios were considered:

Scenario 0 The number of events follows a Poissonian where the mean is sampled from a Gaussian with the mean and standard deviation taken from the estimated background contribution from the baseline fit.

Scenario A Sample the number of observed events.

Scenario	$n_{\mathrm{Z+D^+}} \geq 4$	$n_{\mathrm{Z+D^0}} \geq 7$	$n_{\mathrm{Z+D^+}} + n_{\mathrm{Z+D^0}} \geq 11$	$n_{\mathrm{Z+D^+}} \geq 4 \vee n_{\mathrm{Z+D^0}} \geq 7$
0	3.28 ± 0.01	3.64 ± 0.02	3.44 ± 0.02	5.13 ± 0.02
A	3.47 ± 0.01	3.71 ± 0.02	3.55 ± 0.02	5.31 ± 0.02
B	3.45 ± 0.01	3.68 ± 0.02	3.53 ± 0.02	5.28 ± 0.02

Table 4.12: All significances obtained for different scenarios.

Scenario B The number of events follows a Poissonian with the mean set to the number of observed events.

Of these scenarios number 0 always yields the lowest significances. This it because the significance is dominated by the tails which receive a large contribution from the Gaussian in that scenario. Nevertheless all scenarios give very similar answers. We chose to quote the lowest significance.

The significance is calculated for several different cases: $n_{\mathrm{Z+D^+}} \geq 4$, $n_{\mathrm{Z+D^0}} \geq 7$, $n_{\mathrm{Z+D^+}} + n_{\mathrm{Z+D^0}} \geq 11$, $n_{\mathrm{Z+D^+}} \geq 4 \vee n_{\mathrm{Z+D^0}} \geq 7$ and shown in Tab. 4.12

4.10.1 Impact from Pileup on the Significance

The contribution of pileup is small. So small that it was not possible to determine with the original selection (see e.g. Fig 4.8). A loosened selection (Fig 4.9) allowed a determination of an upper limit on the pileup of $(2.8 \pm 0.6)\,\%$. In order to assign a p–value to this background the probability that this background fluctuates over the observed seven events is calculated treating the mean of the Poissonian as a random variable itself which is assumed to follow a normal distribution with the negative tail cut off.

$$p = \frac{\sum_7^\infty \int_0^\infty G(\mu, \mu_0, \sigma) P_k(\mu)\,\mathrm{d}\,\mu}{\int_0^\infty G(\mu, \mu_0, \sigma)\,\mathrm{d}\,\mu}. \tag{4.18}$$

Using Formula 8.352 in [103] the series over the poissionians can be rewritten as:

$$\sum_{k=m+1}^{\infty} f(k, \lambda) = \gamma(1 + m, \lambda)/m! \tag{4.19}$$

with

$$\gamma(\alpha, x) = \int_0^x e^{-t} t^{\alpha-1} dt. \tag{4.20}$$

This – together with the slightly different definition (with respect to [103] and Equation 4.20) of the incomplete Gamma function in the SciPy library leads to:

$$p = \langle \texttt{gammainc}(7, \mu) \rangle = 3.9 \cdot 10^{-9}, \tag{4.21}$$

where μ was sampled from a truncated Gaussian of mean 0.196 and sigma of 0.042 using 10^8 samples. It has to be stressed again that this probability is calculated from the loosened selection which is expected to let more background in than the baseline selection. In summary, the probability for a fluctuation of the pileup contribution is much smaller than the probability for the combinatorial background.

4.11 Conclusion

LHCb has evidence for the associated production of Z and charmed hadrons in pp collisions at an energy $\sqrt{s} = 7$ TeV using a dataset of 1 fb^{-1}. There were eleven candidates in total with seven D^0 and four D^+ mesons in association with a $\text{Z} \to \mu^+\mu^-$.

Due to the $\mathcal{O}(5\%)$ branching fractions a distinction of $\text{c}\bar{\text{c}}$ production and cases with only one c in the LHCb acceptance is not possible. It's already rare that the c hadronises in a D^0 which subsequently decays to $\text{K}^-\pi^+$ but then it's even rarer that the $\bar{\text{c}}$ also hadronises and decays as $\text{D}^0 \to \text{K}^-\pi^+$.

A natural extension of this analysis would be using c–tagged jets which would have the opposite properties. High efficiency that possibly allows to distinguish single from dicharm events but no access to the sign of the c–quantum number. Calibrated c–tagging for jets was not available in LHCb when these results were published. An analysis of the $\text{W}^\pm$c-jet final state has recently entered the LHCb review. This adds another flavour specific constraint to PDFs.

Chapter 5

Inclusive Z Production at $\sqrt{s} = 2.76$ TeV

In the beginning of 2013 the LHC was colliding protons at $\sqrt{s} = 2.76\,\text{TeV}$. This new collision energy provides another data point in the $(\sigma, \sqrt{s})$ plane. Unfortunately the LHC ran for only a short time at this energy allowing LHCb to take $3.31 \pm 0.08\,\text{pb}^{-1}$ of integrated luminosity. The results shown in this chapter are obtained using LHCb data but did not go though the internal LHCb review. Therefore the results are all unofficial LHCb results. The efficiency numbers [1] in this chapter are provided by Stephen Farry and the predictions from FEWZ [96] by Katharina Müller.

The production of heavy states like Z bosons is enhanced at central rapidities. This can be seen from Figure 2.5. Since the momentum fraction of the participating partons can't exceed unity the lower bound of the mass window of 60 GeV used in this measurement yields a kinematic boundary of $y_Z < 3.83$ (see Equation 1.55). Using the known Z mass Equation 1.55 yields a kinematic limit of $y_Z < 3.4$. The kinematic boundary leads to a reduced cross section at high invariant masses.

That also means that the instrumentation of LHCb at high η_μ can not be used to measure these events. The muon with the largest η_μ observed was reconstructed at $\eta_\mu = 4.01$. As can be seen from Figure 5.1 the low η_μ boundary that was used in the large statistics measurements [69, 70] at 7 TeV is not best suited for a measurement at $\sqrt{s} = 2.76$ TeV. Therefore it was investigated [1] if the interval can be extended towards lower η_μ. It was found that a measurement is possible for muons in the range $1.75 \leq \eta_\mu \leq 4.5$.

5.1 Dataset and Selection

The selection criteria are almost identical to the ones used in the measurements at 7 TeV [69, 70]. The only difference is that the pseudorapidity range and thus the rapidity range was opened towards lower values. The selection criteria are:

Trigger: The events are triggered on the single muon lines: `L0Muon, Hlt1SingleMuonHighPT and Hlt2SingleMuonHighPT`. At least one of the muons has to be TOS on all of these triggers. There was only one trigger configuration (TCK) used for this dataset: 0xA90046. That TCK has been used in 2012 to trigger about 60 pb^{-1} of data. This trigger path contains a global event cut at $n_{SPD} < 600$.

Tracking: The tracks are required to have $P(\chi^2, n_{d.o.f}) > 0.1\,\%$. It has to be stressed here that the track χ^2 doesn't follow a χ^2 distribution and this requirement leads to an inefficiency in excess of 0.1 %.

Muon Identification The muons are identified using hits in the muon chambers that are added to the track. That criterion is called `ISMUON` in LHCb jargon and software.

Kinematics: The p_T of both muons has to be larger than 20 GeV. The pseudorapidity η_μ is required to be between 1.75 and 4.5. The invariant mass of the Z $\rightarrow \mu^+\mu^-$candidate has to be reconstructed between 60 and 120 GeV.

The dataset consists of $3.31 \pm 0.08\,\mathrm{pb}^{-1}$ of data integrated luminosity taken in pp collisions at $\sqrt{s} = 2.76\,\mathrm{TeV}$ in 2013. Pileup was reduced with respect to the data taken in 2012 at 8 TeV and most of the bunch crossings did not lead to any hard interaction. The average number of visible interactions per bunch crossing was in the 0.4 regime. The distribution is shown in Figure 1.13.

5.2 Candiates

There are 32 candidates in the dataset. If the selection from the large statistics analyses [69, 70] ($\eta_\mu > 2$) is used that number drops to 19 candidates. The η_μ and y_Z distributions are shown, in Figures 5.1 and 5.2. In Figure 5.3 the cross section as a function of the invariant mass is compared to FEWZ. FEWZ was corrected for FSR and resolution as described in Section 4.7.1. It can be seen in both prediction and measurement that the loosened η_μ requirement increases the acceptance at high invariant mass.

5.3 Efficiency Correction and Cross Section Estimation

The efficiency correction is done event by event. For each event i the total efficiency ε_i is calculated according to Equation 2.9. For each event weights are then calculated as

$$w_i = \varepsilon_i^{-1}. \tag{5.1}$$

The cross section is then calculated as:

$$\sigma = \frac{1}{\int \mathcal{L}} \sum_i w^i. \tag{5.2}$$

If the measurement is performed differentially an additional division by the bin width is performed. The reconstruction and trigger efficiency numbers are taken from [1]. Even though the GEC are applied in the trigger the GEC efficiency is calculated independently from the efficiencies to *reconstruct* the muon at the trigger level. The calculation of the GEC efficiency is presented in Section 2.8. Due to the lower pileup the GEC efficiency approaches unity and the remaining inefficiency is neglected. Using this selection the purity is high. Similar studies have found impurities of 0.3%. [64, 69, 70, 77]. The lower pileup suggest that the impurities are even lower in this measurement.

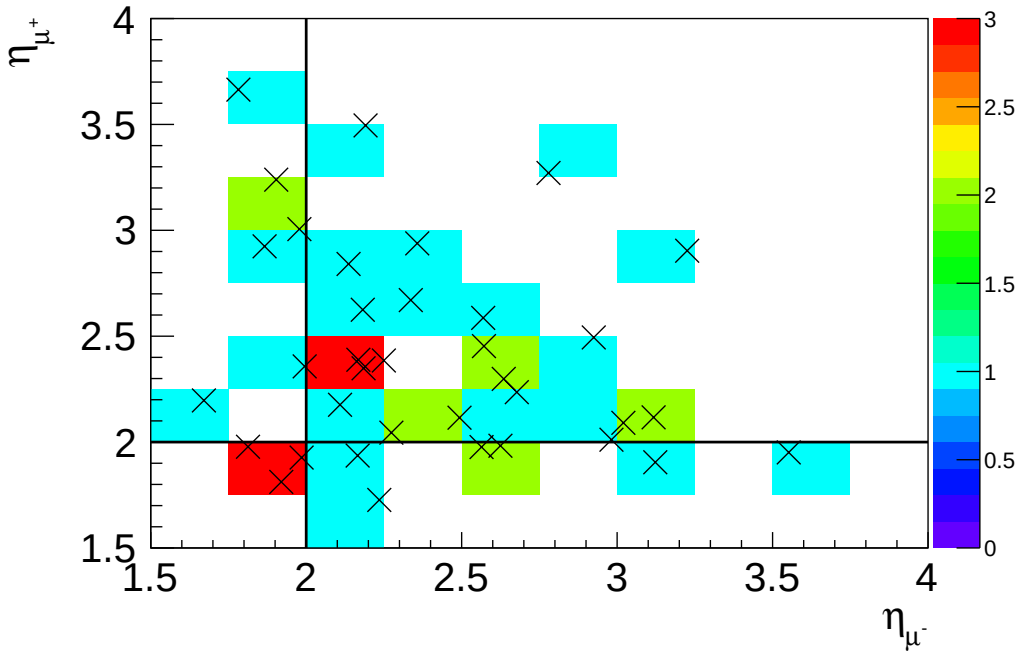

Figure 5.1: Pseudorapidity distribution of the muons from the Z candidates. The lines indicate the lower bound of the large statistics measurements. This analysis uses one additional bin down to $\eta_\mu > 1.75$. The upper boundaries of $\eta_\mu < 4.5$ don't reject any events. There are no Z candidates observed with muons outside the plotted region.

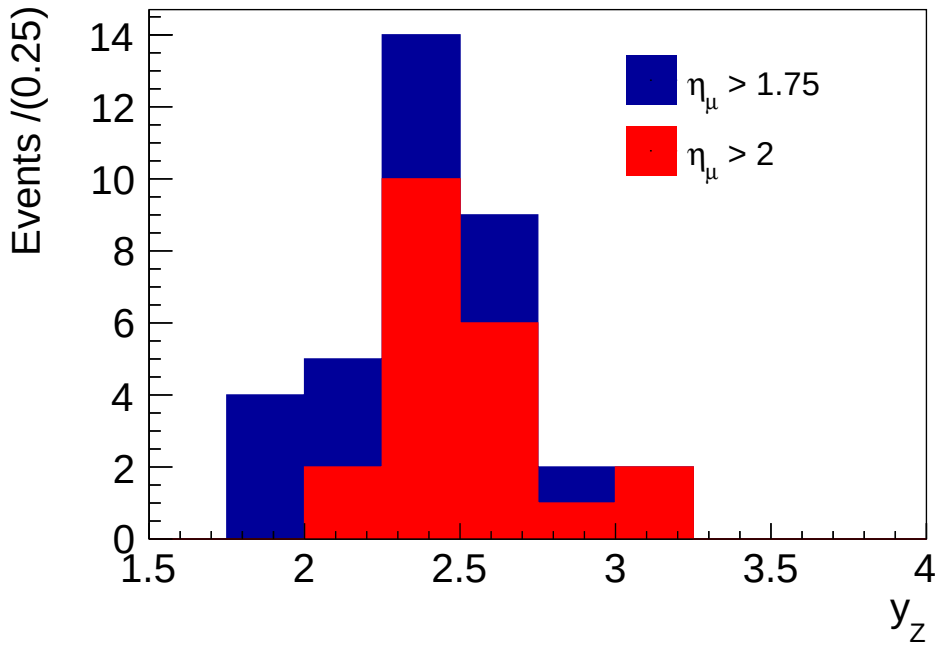

Figure 5.2: y_Z distribution of the Z candidates. The distributions are overlayed not stacked. This is possible since the events with $\eta_\mu > 2$ are a strict subset of those without that requirement. The cut off at two is a direct result of the $\eta_\mu > 2$ threshold.

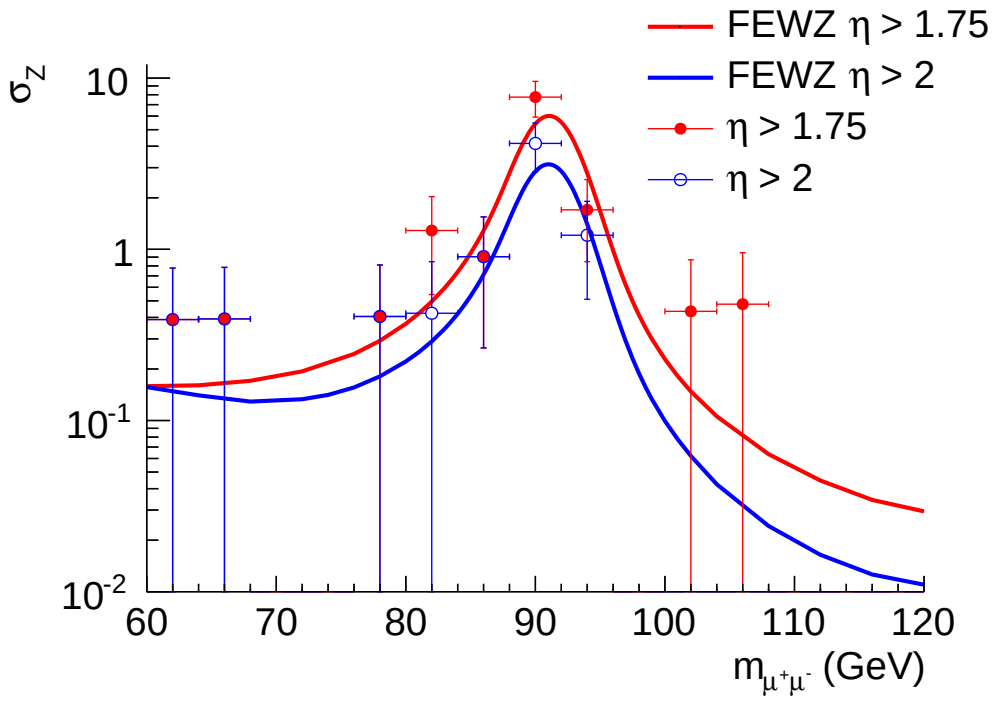

Figure 5.3: Inclusive Z production cross - section $\sigma_{\mathrm{Z}}(m_{\mathrm{Z}})$ as a function of the Z mass. The mass is not unfolded for resolution effects and compared to the prediction from FEWZ as described in Section 4.7.1.

However the lower energy suggests that the signal will decrease faster than the background does. The cross section of the main background ($\approx 0.2\%$) which is beauty production decreases by a factor of three [22] while the signal decreases by a factor of ten. This leads to a background estimate of $0.2\% * 10/3 + 0.1\% \approx 0.8\%$. Since the statistical uncertainties dominate and the small impurities are neglected in this measurement.

5.4 Uncertainties

5.4.1 Statistical Uncertainty

The statistical uncertainty dominates by far. The low number of events suggests that the statistical uncertainty should be asymmetric around the mean since the usual method of approximating the Poissonian distribution by a Gaussian distribution is not a valid approximation. However the individual weights of the events complicate the calculation of the confidence level. Several methods have been used to calculate this uncertainty. They are described in the following and summarised in Figure 5.5.

Gaussian

In the Gaussian approximation the variance is given by:

$$\sigma_{\text{stat}} = \sqrt{\sum_i w_i^2}. \tag{5.3}$$

Conservative Estimation with Poissonian

A conservative approximation can be obtained when Equation 5.2 is rewritten as:

$$\sigma = \frac{< w_i >}{\int \mathcal{L}} n \tag{5.4}$$

where $< w_i >$ denotes the mean of the w_i and n is the number of events which follows a Poissonian distribution. Now the lower bound of the confidence interval is restricted to be larger than the maximal n_{low} that satisfies:

$$\max(w_i) \sum_{i=n}^{\infty} P_{\text{Poisson}}(n_{\text{low}}, i) < \frac{1 - 68\%}{2}. \tag{5.5}$$

analogously the upper bound of the confidence interval n_{high} is smaller than the smallest that satisfies:

$$\min(w_i) \sum_{i=0}^{n} P_{\text{Poisson}}(n_{\text{high}}, i) < \frac{1 - 68\%}{2}. \tag{5.6}$$

Then a confidence interval that is expected to over cover the 68% confidence intervall is given by $[n_{\text{low}}, n_{\text{high}}]$. This is implemented by turning the inequalities into equations and numerically solving those using the cumulative density function (CDF) and a numeric solver as implemented in `SciPy`.

Bootstrap

In order to obtain a confidence interval that actually integrates to 68%, instead of only containing them, another method is utilised.

For each value of possible yields y_{test}, that is supposed to be tested in light of the data, the frequency of the obtained value from toy experiments exceeding the measured value is evaluated. The toy experiments are calculated by randomly drawing n weights from the pool of observed events where n is again sampled randomly from a Poissonian distribution of mean n_{test} which is approximated as to be:

$$n_{\text{test}} = \frac{y_{\text{test}}}{< w_i >}. \tag{5.7}$$

The possible values are scanned using a modified binary search. Instead of the two bins of a binary search, 500 equidistant bins are used. Then the search interval is subsequently reduced around the minimal distance to the target value of the frequency. The new search window is set around the minimal distance to the target value. It contains all bins that are closer to the target value than ten times the smallest distance and an additional margin of ten bins. In order to have a large number of toy MC close to the region of interest the number of toy experiments per bin is set to:

$$n_{\text{toy}} = \frac{10^5}{n_{\text{high}} - n_{\text{low}}}. \tag{5.8}$$

The result is accepted if the distance in frequency is lower than 10^{-5} and the length of the search interval is less than 0.1. Together with Equation 5.8 this ensures that at least 10^6 toy MC events were used to calculate the final value.

The scan is shown in Figure 5.4.

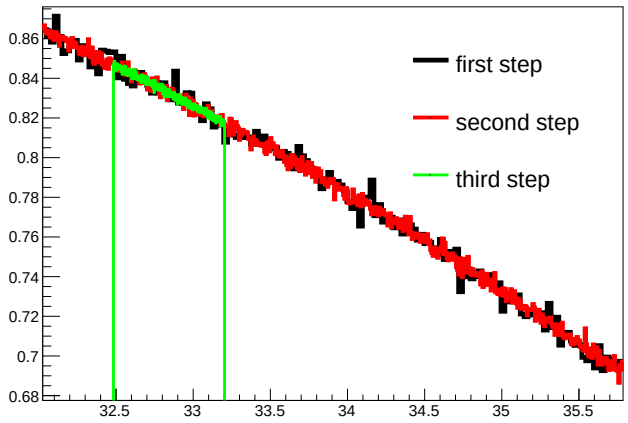

(a) Scan at lower boundary.

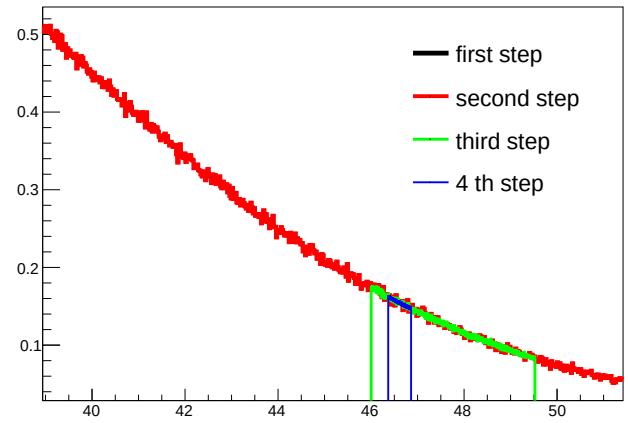

(b) Scan at upper boundary.

Figure 5.4: Estimation of the CDF using the bootstrap method evaluated using an MC integration. The precision is increased in the region of interest. This example uses the set of weights obtained for the $\eta_\mu > 1.75$ selection. Each histogram has 500 bins.

5.4.2 Systematic Uncertainties

Luminosity

The uncertainty on the luminosity is used as it is reported by the common LHCb luminosity tool. It is converted into a relative uncertainty and multiplied with the cross section to an absolute uncertainty on the cross section. Luminosity is the dominant systematic uncertainty for this measurement.

Efficiency

The uncertainty on the efficiencies is marginal. It's 0.44% for the lower boundary and 0.76% for the upper boundary. It is propagated by an MC integration method using the PDFs described in Section 2.8.1. The overall uncertainty arising from this source is less than one percent.

5.5 Results

The cross section for Z $\rightarrow \mu^+\mu^-$ at $\sqrt{s} = 2.76\,\text{TeV}$ is measured to be:

$$\begin{aligned}\sigma_{1.75} &= 13.43 \pm 6.89 \pm 0.06 \pm 0.67\,\text{pb}\\ \sigma_{2.00} &= 7.87 \pm 5.25 \pm 0.06 \pm 0.39\,\text{pb}\end{aligned}$$

where the uncertainties are statistical, systematic from efficiencies and systematic from luminosity. The index on σ denotes the minimal η_μ required for both muons. This compares to the NNLO prediction from FEWZ [96] of:

$$\begin{aligned}\sigma_{1.75,\text{FEWZ}} &= 11.745^{+0.341\ +0.12}_{-0.232\ -0.08}\,\text{pb}\\ \sigma_{2.00,\text{FEWZ}} &= 6.31^{+0.19}_{-0.13} \pm 0.05\,\text{pb}\end{aligned}$$

where the first uncertainty is PDF and the second is scale. The differential cross section is presented in Figure 5.5. There is agreement between the predicted values from FEWZ [96] and the measurements within the large statistical uncertainties of the measurements. The acceptance and thus the statistical uncertainty was improved with respect to the selection used in the large statistics measurements [69, 70]. The available integrated luminosity is $\mathcal{O}(10^{-3})$ of these measurements and thus their precision could not be achieved.

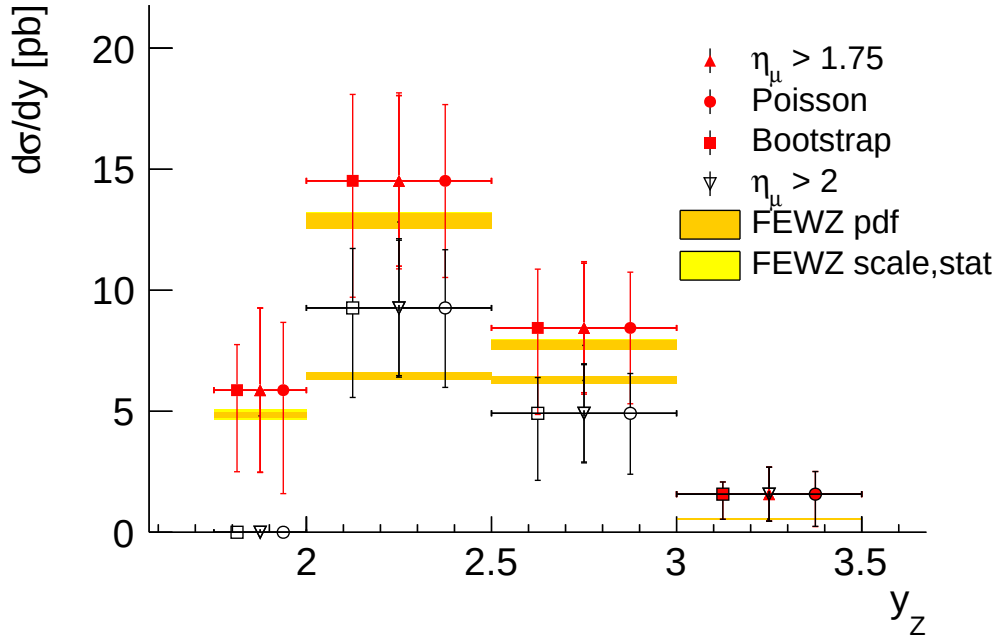

Figure 5.5: Differential cross section $\frac{\mathrm{d}\,\sigma}{\mathrm{d}\,y_Z}$. The inner error bars denote the statistical uncertainty while the outer error bars denote the systematic uncertainty which is dominated by the luminosity.

Conclusion

During my doctorate studies I contributed to many measurements involving Z bosons in the dimuon final state. Starting with the early paper [69] where the capability of the LHCb experiment of the reconstruction of gauge bosons was demonstrated. This measurement was already useful to constrain parton density functions. Continued with the established signal and afterwards the measurement of the associated production of Z bosons with jets. Again this measurement has sensitivity to parton density functions with a focus slightly shifted towards gq initial states. The measurement of the cross section of associated of Z bosons with D mesons suffers from large statistical uncertainties but demonstrated a significant signal which can be studied with the calibrated c/b tagged jets that became available in the meantime. The measurement of the associated production of Z bosons with b-jets is published in [**?**].

A continuation of these studies should include the $W^{\pm}$ bosons. $W^{\pm}$ bosons are much more frequent but they can not fully reconstructed in the $\mu\nu_{\mu}$ channel. The associated production of $W^{\pm}$ with charm is sensitive to the strange quark PDF in the proton. This was measured in [**?**]. When a $W^{\pm}$ is reconstructed in association with a beauty quark this is already the path to top quark reconstruction and thus to a wide range of measurements within and beyond the Standard Model.

Since the beginning of the data taking in 2010 the LHCb experiment keeps pushing it's limits. Designed as a dedicated flavour physics experiment that was supposed to veto events with multiple interactions at very low instantaneous luminosity it became a general purpose forward detector processing four times the collisions than it was designed for in each bunch crossing. All this without was achieved without damage to the flavour physics programme. The flavour physics programme actually benefits from the increased luminosity.

Acknowledgements

First of all I want to thank Ueli Straumann for giving me the opportunity to join his remarkable group and do my doctorate studies! The climate he keeps in the group allows individual freedom in research as well as close collaboration and guidance. I want to thank Katharina Müller for supervising my thesis. She always had an open ear for my questions and also provided a lot of help in solving the problems no matter if they where problems of physics understanding; collaboration politics or the presentation of the results. This thesis would be very different without her support. She calculated all the predictions from MCFM and FEWZ the measurements where compared to. I'm also indebted to the other members of the whole Zürich group especially Jonathan Anderson; Michel De Cian; Mark Tobin; Sandra Saornil; Peter Lowden; Christian Elsasser; Nicola Chiapolini; and Roland Bernet for the help in dealing with all the little problems that arise every day from PYTHIA; ROOT; python; Gaudi; LaTeX etc. as well as the physics discussions and detector operations.

The whole thesis was read by Katharina Müller and Annika Behrens. Peter Lowden and Alexandra Carvalho Antunes De Olivera provided very helpful comments to the theory section. Richard Jacobson to the sections concerning beam and datataking conditions. Jonathan Anderson provided help in for the sections concerning Z reconstruction at both 7 TeV and at 2.76 TeV. Victor Coco provided very helpful input to the jets section.

My thanks also goes to my collaborators in LHCb. Namely William James Barter and Victor Coco for their contributions to the measurements of associated production of Z bosons with jets and Vanya Belyaev for his contributions to the measurement of the associated production of Z bosons with D mesons as well as for creating the LoKi framework and his fast and helpful answers to the countless questions arising from it's use. A look to the LHCb mailing list archives shows there is hardly any analysis in the whole collaboration that did not benefit from that.

There is also a social part that made this thesis possible. All the friends that were there in the dark times. My thanks go to my girlfriend Annika Behrens who supported me throughout this project. I thank my friends Marco Giebeler; Alexandra Carvalho Antunes De Olivera; Aneta Koralevska; Annamária Wilde; Monika Jopkova; Yasime Sinno; Lucia Hosekova; Gabriela d' Hondt; and Elizabeth Castaneda Miranda for the beautiful time we shared in places like Rogoznica; Zuoz; Amazonia; Padova; Praha; Poznan; Zakopane; Lodz; Liptovský Mikuláš; Ocaña; Sevilla; Istanbul or even Kastellaun and CERN.

Thanks for the dance to Lea Krämer; Yasmine Sinno; Elisabeth Grimon; and Soledad Canterini and to Angela Baciu for teaching me how to dance.

Appendix A

Z+D

A.1 Tables with Fit Values

The meaning of the values is explained in Section 4.7 and [95] (Table E.1).

Table A.1: Baseline D^0 floating

	Initial Value		Fit Value			
n_{b_D,b_Z}	0.0	events	0.0	±	31.2	events
n_{b_D,s_Z}	0.0	events	0.0	±	69804.1	events
n_{s_D,s_Z}	87.0	events	154.7	±	92052.4	events
$\tau_{m_{hadron}}$	9.1	GeV^{-1}	9.6	±	29.2	GeV^{-1}
$\tau_{m_{hadron},\text{full combinatorial}}$	4.9	GeV^{-1}	6.9	±	28.4	GeV^{-1}
$\tau_{m_{\mu^+\mu^-},\text{full combinatorial}}$	0.0	GeV^{-1}	−0.0	±	28.5	GeV^{-1}

Table A.2: Baseline D^0 fixed parameters

	Fixed Value	
n_{s_D,b_Z}	0.0	events
$\alpha_{\text{Crystal Ball}}$	1.7572	
$\text{bias}_{\text{Crystal Ball}}$	−0.0873499	GeV
μ_{D^0}	1.86271	
$n_{\text{Crystal Ball}}$	1.30199	
ρ_{l,D^0}	−0.170619	
ρ_{r,D^0}	−0.289993	
$\sigma_{\text{Crystal Ball}}$	1.70988	GeV
σ_{D^0}	0.00729757	
$\tau_{m_{\mu^+\mu^-}}$	−1.0	GeV^{-1}
ξ_{D^0}	−0.00044	

Table A.3: Z background cross check D^0 floating

	Initial Value		Fit Value			
n_{b_D,b_Z}	0.0	events	0.0	±	0.6	events
n_{b_D,s_Z}	7.0	events	0.0	±	7.8	events
n_{s_D,b_Z}	1.0	events	0.0	±	184.3	events
n_{s_D,s_Z}	15.0	events	7.0	±	1.73	events
$\tau_{m_{\text{hadron}}}$	−2.2	GeV^{-1}	9.9	±	31.5	GeV^{-1}
$\tau_{m_{\mu^+\mu^-}}$	−1.0	GeV^{-1}	−0.0	±	29.2	GeV^{-1}
$\tau_{m_{\text{hadron}},\text{full combinatorial}}$	−5.6	GeV^{-1}	5.4	±	22.2	GeV^{-1}
$\tau_{m_{\mu^+\mu^-},\text{full combinatorial}}$	−0.0	GeV^{-1}	−0.0	±	29.9	GeV^{-1}

Table A.4: Z background cross check D^0 fixed parameters

	Fixed Value	
$\alpha_{\text{Crystal Ball}}$	1.7572	
$\text{bias}_{\text{Crystal Ball}}$	−0.0873499	GeV
μ_{D^0}	1.86271	
$n_{\text{Crystal Ball}}$	1.30199	
ρ_{l,D^0}	−0.170619	
ρ_{r,D^0}	−0.289993	
$\sigma_{\text{Crystal Ball}}$	1.70988	GeV
σ_{D^0}	0.00729757	
ξ_{D^0}	−0.00044	

Table A.5: Background only D^0 floating

	Initial Value		Fit Value			
$n_{b_{\text{D}},b_{\text{Z}}}$	0.0	events	0.0	±	0.0	events
$n_{b_{\text{D}},s_{\text{Z}}}$	0.0	events	0.2	±	61438.5	events
$\tau_{\text{m}_{\text{hadron}}}$	9.6	GeV^{-1}	−2.2	±	9.7	GeV^{-1}
$\tau_{\text{m}_{\text{hadron}},\text{full combinatorial}}$	6.9	GeV^{-1}	−7.5	±	14.7	GeV^{-1}
$\tau_{\text{m}_{\mu^+\mu^-},\text{full combinatorial}}$	−0.0	GeV^{-1}	−0.0	±	12.9	GeV^{-1}

Table A.6: Background only D^0 fixed parameters

	Fixed Value	
n_{s_D,b_Z}	0.0	events
n_{s_D,s_Z}	0.0	events
$\alpha_{\text{Crystal Ball}}$	1.7572	
$\text{bias}_{\text{Crystal Ball}}$	−0.0873499	GeV
μ_{D^0}	1.86271	
$n_{\text{Crystal Ball}}$	1.30199	
ρ_{l,D^0}	−0.170619	
ρ_{r,D^0}	−0.289993	
$\sigma_{\text{Crystal Ball}}$	1.70988	GeV
σ_{D^0}	0.00729757	
$\tau_{m_{\mu^+\mu^-}}$	−1.0	GeV^{-1}
ξ_{D^0}	−0.00044	

Table A.7: Baseline D^+ floating

	Initial Value		Fit Value			
n_{b_D,b_Z}	0.0	events	0.0	±	0.1	events
n_{b_D,s_Z}	0.0	events	0.0	±	248.2	events
n_{s_D,s_Z}	17.7	events	6.8	±	99292.4	events
$\tau_{m_{\text{hadron}}}$	−0.0	GeV^{-1}	−0.0	±	12.6	GeV^{-1}
$\tau_{m_{\mu^+\mu^-}}$	−9.6	GeV^{-1}	−5.3	±	2.6	GeV^{-1}
$\tau_{m_{\text{hadron}},\text{full combinatorial}}$	−0.0	GeV^{-1}	−0.0	±	12.5	GeV^{-1}
$\tau_{m_{\mu^+\mu^-},\text{full combinatorial}}$	−0.0	GeV^{-1}	−0.0	±	25.6	GeV^{-1}

Table A.8: Baseline D^+ fixed parameters

	Fixed Value	
n_{s_D,b_Z}	0.0	events
$\alpha_{\text{Crystal Ball}}$	1.7572	
$\text{bias}_{\text{Crystal Ball}}$	−0.0873499	GeV
μ_{D^+}	1.86862	
$n_{\text{Crystal Ball}}$	1.30199	
ρ_{l,D^+}	−0.107796	
ρ_{r,D^+}	−0.284132	
$\sigma_{\text{Crystal Ball}}$	1.70988	GeV
σ_{D^+}	0.00693069	
ξ_{D^+}	−0.000244474	

Table A.9: Z background cross check D^+ floating

	Initial Value		Fit Value			
n_{b_D,b_Z}	0.0	events	0.0	±	154.0	events
n_{b_D,s_Z}	6299.0	events	0.0	±	1439.9	events
n_{s_D,b_Z}	1.0	events	0.0	±	350.1	events
n_{s_D,s_Z}	15.0	events	27.6	±	51886.1	events
$\tau_{m_{\text{hadron}}}$	−0.0	GeV^{-1}	−0.0	±	19.0	GeV^{-1}
$\tau_{m_{\mu^+\mu^-}}$	−1.1	GeV^{-1}	−1.1	±	19.5	GeV^{-1}
$\tau_{m_{\text{hadron}},\text{full combinatorial}}$	−0.0	GeV^{-1}	−0.0	±	19.9	GeV^{-1}
$\tau_{m_{\mu^+\mu^-},\text{full combinatorial}}$	−0.0	GeV^{-1}	−0.0	±	27.2	GeV^{-1}

Table A.10: Z background cross check D^+ fixed parameters

	Fixed Value	
$\alpha_{\text{Crystal Ball}}$	1.7572	
$\text{bias}_{\text{Crystal Ball}}$	−0.0873499	GeV
μ_{D^+}	1.86862	
$n_{\text{Crystal Ball}}$	1.30199	
ρ_{l,D^+}	−0.107796	
ρ_{r,D^+}	−0.284132	
$\sigma_{\text{Crystal Ball}}$	1.70988	GeV
σ_{D^+}	0.00693069	
ξ_{D^+}	−0.000244474	

Table A.11: Background only D^+ floating

	Initial Value		Fit Value			
n_{b_D,b_Z}	0.0	events	0.0	±	0.0	events
n_{b_D,s_Z}	0.0	events	6299.0	±	94222.3	events
$\tau_{\text{m}_{\text{hadron}}}$	−0.0	GeV^{-1}	−0.0	±	20.6	GeV^{-1}
$\tau_{\text{m}_{\mu^+\mu^-}}$	−5.3	GeV^{-1}	−1.1	±	13.7	GeV^{-1}
$\tau_{\text{m}_{\text{hadron}},\text{full combinatorial}}$	−0.0	GeV^{-1}	−0.0	±	5.7	GeV^{-1}
$\tau_{\text{m}_{\mu^+\mu^-}},\text{full combinatorial}$	−0.0	GeV^{-1}	−0.0	±	13.3	GeV^{-1}

Table A.12: Background only D^+ fixed parameters

	Fixed Value	
n_{s_D,b_Z}	0.0	events
n_{s_D,s_Z}	0.0	events
$\alpha_{\text{Crystal Ball}}$	1.7572	
$\text{bias}_{\text{Crystal Ball}}$	−0.0873499	GeV
μ_{D^+}	1.86862	
$n_{\text{Crystal Ball}}$	1.30199	
ρ_{l,D^+}	−0.107796	
ρ_{r,D^+}	−0.284132	
$\sigma_{\text{Crystal Ball}}$	1.70988	GeV
σ_{D^+}	0.00693069	
ξ_{D^+}	−0.000244474	

Table A.13: Flat background model D^+ floating

	Initial Value		Fit Value			
n_{b_D,b_Z}	0.0	events	0.0	±	726.9	events
n_{b_D,s_Z}	0.0	events	0.0	±	1096.7	events
n_{s_D,s_Z}	15.0	events	26.8	±	92473.8	events

Table A.14: Flat background model D^+ fixed parameters

	Fixed Value	
n_{s_D,b_Z}	0.0	events
$\alpha_{\text{Crystal Ball}}$	1.7572	
$\text{bias}_{\text{Crystal Ball}}$	−0.0873499	GeV
μ_{D^+}	1.86862	
$n_{\text{Crystal Ball}}$	1.30199	
ρ_{l,D^+}	−0.107796	
ρ_{r,D^+}	−0.284132	
$\sigma_{\text{Crystal Ball}}$	1.70988	GeV
σ_{D^+}	0.00693069	
$\tau_{m_{\text{hadron}}}$	0.0	GeV^{-1}
$\tau_{m_{\mu^+\mu^-}}$	0.0	GeV^{-1}
$\tau_{m_{\text{hadron}},\text{full combinatorial}}$	0.0	GeV^{-1}
$\tau_{m_{\mu^+\mu^-},\text{full combinatorial}}$	0.0	GeV^{-1}
ξ_{D^+}	−0.000244474	

Table A.15: Flat background model D^0 floating

	Initial Value		Fit Value			
n_{b_D,b_Z}	0.0	events	0.0	±	0.5	events
n_{b_D,s_Z}	0.0	events	0.0	±	4.6	events
n_{s_D,s_Z}	15.0	events	5.8	±	61169.9	events

Table A.16: Flat background model D^0 fixed parameters

	Fixed Value	
n_{s_D,b_Z}	0.0	events
$\alpha_{\text{Crystal Ball}}$	1.7572	
$\text{bias}_{\text{Crystal Ball}}$	−0.0873499	GeV
μ_{D^0}	1.86271	
$n_{\text{Crystal Ball}}$	1.30199	
ρ_{l,D^0}	−0.170619	
ρ_{r,D^0}	−0.289993	
$\sigma_{\text{Crystal Ball}}$	1.70988	GeV
σ_{D^0}	0.00729757	
$\tau_{m_{\text{hadron}}}$	0.0	GeV^{-1}
$\tau_{m_{\mu^+\mu^-}}$	0.0	GeV^{-1}
$\tau_{m_{\text{hadron}},\text{full combinatorial}}$	0.0	GeV^{-1}
$\tau_{m_{\mu^+\mu^-},\text{full combinatorial}}$	0.0	GeV^{-1}
ξ_{D^0}	−0.00044	

A.2 Extrapolation of the Inclusive Charm Cross Section to the Fiducial Volume

In order to have a inclusive charm cross section for the fiducial volume used in this analysis the numbers from [92] were used. In that paper the cross sections were measured double differentially in η and p_T for $0 < p_T < 8$ GeV. Not all bins have been measured due to limited statistics and kinematic acceptance. To get a number to compare to, the cross section in the available bins with $p_T > 2$ GeV was added up. In the bins where no measurements where available the cross section was extrapolated assuming an exponential p_T dependence of the cross section. In order to have the uncertainty properly represented in the fit the uncertainties have been added quadratically in each measured bin. The distributions are shown in Figs. A.1 and A.2. The cross section numbers calculated this way are summarised in table 4.2. Unlike the other cross section numbers in the note these numbers are quoted irrespective of the D decay following the conventions of [92]. The squared sum of the up and downward shifted exponential was used as estimator of the extrapolation uncertainty. The integrated values for the fiducial of this analysis are given in Table. A.17

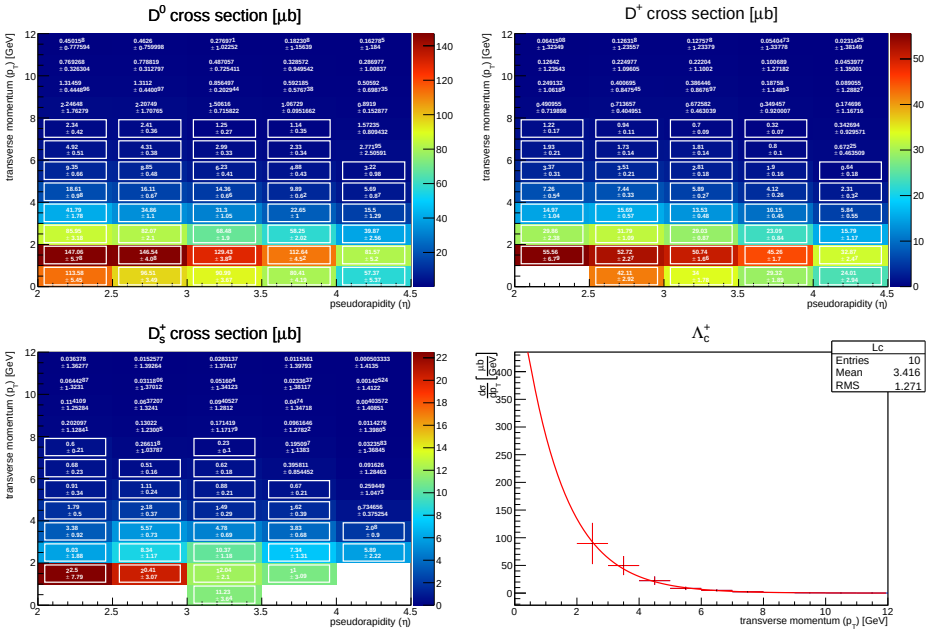

Figure A.1: Extrapolated and measured inclusive charm cross sections. The measured values are taken from [92] and marked by a white box. In the case of Λ_c^+ which was only measured single differentially the measured values are printed in red while the extrapolated values are given in blue.

	before		after extrapolation
Λ_c^+	177.70 ± 41.79 μb	Λ_c^+	179.59 ± 41.83 μb
D^+	238.44 ± 3.58 μb	D^+	244.28 ± 6.20 μb
D^0	599.60 ± 6.56 μb	D^0	620.63 ± 8.09 μb
D_s^+	70.90 ± 4.14 μb	D_s^+	74.07 ± 7.78 μb

Table A.17: Summed and extrapolated cross sections.

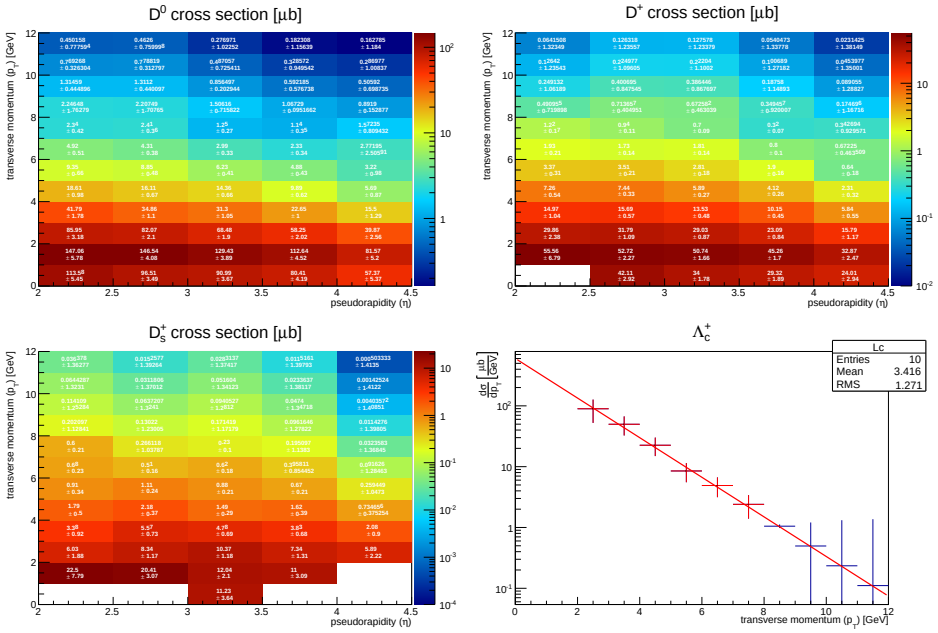

Figure A.2: Extrapolated and measured inclusive charm cross sections on a logarithmic scale. The measured values are taken from [92] and printed in two digit precision. The white rectangles don't work in log mode but the measured bins are equal to those in Fig. A.1. In the case of Λ_c^+ which was only measured single differentially the measured values are printed in red while the extrapolated values are given in blue.

Bibliography

[1] S. Farry, *A measurement of high-p_T muon reconstruction efficiencies in 2011 and 2012 data.*, .

[2] J. M. Campbell and R. Ellis, *MCFM for the Tevatron and the LHC*, Nucl. Phys. Proc. Suppl. **205-206** (2010) 10, arXiv:1007.3492.

[3] R. Gavin, Y. Li, F. Petriello, and S. Quackenbush, *FEWZ 2.0: A code for hadronic Z production at next-to-next-to-leading order*, Comput. Phys. Commun. **182** (2011) 2388, arXiv:1011.3540.

[4] V. Coco, *Reconstruction et identification de jets beaux dans l'expérience LHCb en vue d'étudier sa sensibilité à un boson de Higgs standard se désintégrant en paires $b\bar{b}$*, PhD thesis, U. de Savoie Annecy, Annecy, 2008, Presented on 29 Sep 2008.

[5] M. De Cian, U. Straumann, O. Steinkamp, and N. Serra, *Track Reconstruction Efficiency and Analysis of $B^0 \to K^{*0}\mu^+\mu^-$ at the LHCb Experiment*, , Presented 14 Mar 2013.

[6] J. Horejsi, *Fundamentals of electroweak theory*, Charles University in Prague, the Karolinum Press, Prague, Czech, 2002.

[7] M. Peskin, *An introduction to quantum field theory*, Addison-Wesley, Reading, Mass, 1995.

[8] S. Weinberg, *The quantum theory of fields*, Cambridge University Press, Cambridge, 2005.

[9] D. Bourilkov, *Search for tev strings and new phenomena in bhabha scattering at cern lep2*, Phys. Rev. D **62** (2000) 076005.

[10] Particle Data Group, J. Beringer *et al.*, *Review of particle physics*, Phys. Rev. **D86** (2012) 010001.

[11] P. J. Mohr, B. N. Taylor, and D. B. Newell, *CODATA recommended values of the fundamental physical constants: 2010*, Reviews of Modern Physics **84** (2012) 1527, arXiv:1203.5425.

[12] The ALEPH, DELPHI, L3 and OPAL Collaborations and the LEP Electroweak Working Group, *Electroweak measurements in electron-positron collisions at w-boson-pair energies at lep*, Phys. Rept. **532** (2013) 119, arXiv:1302.3415.

[13] Particle Data Group, K. A. Olive *et al.*, *Review of particle physics*, Chin. Phys. **C38** (2014) 090001.

[14] UA1 Collaboration, G. Arnison *et al.*, *Experimental Observation of Isolated Large Transverse Energy Electrons with Associated Missing Energy at s**(1/2) = 540-GeV*, Phys. Lett. **B122** (1983) 103.

[15] UA2 Collaboration, M. Banner *et al.*, *Observation of Single Isolated Electrons of High Transverse Momentum in Events with Missing Transverse Energy at the CERN anti-p p Collider*, Phys. Lett. **B122** (1983) 476.

[16] UA1 Collaboration, G. Arnison *et al.*, *Experimental Observation of Lepton Pairs of Invariant Mass Around 95-GeV/c**2 at the CERN SPS Collider*, Phys. Lett. **B126** (1983) 398.

[17] UA2 Collaboration, P. Bagnaia *et al.*, *Evidence for Z0 →; e+ e- at the CERN anti-p p Collider*, Phys. Lett. **B129** (1983) 130.

[18] ATLAS Collaboration, G. Aad *et al.*, *Observation of a new particle in the search for the Standard Model Higgs boson with the ATLAS detector at the LHC*, Phys. Lett. **B716** (2012) 1, arXiv:1207.7214.

[19] CMS Collaboration, S. Chatrchyan *et al.*, *Observation of a new boson at a mass of 125 GeV with the CMS experiment at the LHC*, Phys. Lett. **B716** (2012) 30, arXiv:1207.7235.

[20] D. J. Gross and F. Wilczek, *Ultraviolet Behavior of Nonabelian Gauge Theories*, Phys. Rev. Lett. **30** (1973) 1343.

[21] H. D. Politzer, *Reliable Perturbative Results for Strong Interactions?*, Phys. Rev. Lett. **30** (1973) 1346.

[22] T. Sjöstrand, S. Mrenna, and P. Skands, *PYTHIA 6.4 physics and manual*, JHEP **05** (2006) 026, arXiv:hep-ph/0603175.

[23] LHCb collaboration, R. Aaij *et al.*, *Observation of excited Λ_b^0 baryons*, Phys. Rev. Lett. **109** (2012) 172003, arXiv:1205.3452.

[24] LHCb collaboration, R. Aaij *et al.*, *Evidence for the decay $X(3872) \to \psi(2S)\gamma$*, arXiv:1404.0275, to appear in Nucl. Phys. B.

[25] LHCb collaboration, R. Aaij *et al.*, *Determination of the $X(3872)$ meson quantum numbers*, Phys. Rev. Lett. **110** (2013) 222001, arXiv:1302.6269.

[26] LHCb collaboration, R. Aaij *et al.*, *Observation of $X(3872)$ production in pp collisions at $\sqrt{s} = 7$ TeV*, Eur. Phys. J. **C72** (2011) 1972, arXiv:1112.5310.

[27] LHCb collaboration, R. Aaij *et al.*, *Observation of the resonant character of the $Z(4430)^-$ state*, Phys. Rev. Lett. **112** (2014) 222002, arXiv:1404.1903.

[28] LHCb collaboration, R. Aaij *et al.*, *Search for the $X(4140)$ state in $B^+ \to J/\psi\phi K^+$ decays*, Phys. Rev. **D85** (2012) 091103(R), arXiv:1202.5087.

[29] CDF Collaboration, T. Aaltonen *et al.*, *Observation of the $Y(4140)$ structure in the $J/\psi\,\phi$ Mass Spectrum in $B^\pm \to J/\psi\,\phi K$ decays*, arXiv:1101.6058.

[30] S. Brodsky, P. Hoyer, C. Peterson, and N. Sakai, *The intrinsic charm of the proton*, Phys. Lett. **B93** (1980) 451.

[31] Y. Kats and M. D. Schwartz, *Annihilation decays of bound states at the LHC*, JHEP **1004** (2010) 016, arXiv:0912.0526.

[32] LHCb collaboration, R. Aaij *et al.*, *Measurement of form-factor-independent observables in the decay $B^0 \to K^{*0}\mu^+\mu^-$*, Phys. Rev. Lett. **111** (2013) 191801, arXiv:1308.1707.

[33] J. Aguilar-Saavedra, *Top flavor-changing neutral interactions: Theoretical expectations and experimental detection*, Acta Phys. Polon. **B35** (2004) 2695, arXiv:hep-ph/0409342.

[34] J. C. Collins, D. E. Soper, and G. F. Sterman, *Factorization of Hard Processes in QCD*, Adv. Ser. Direct. High Energy Phys. **5** (1988) 1, arXiv:hep-ph/0409313.

[35] H. D. Politzer, *Power corrections at short distances*, Nuclear Physics B **172** (1980), no. 0 349 .

[36] N. Paver and D. Treleani, *Multiquark scattering and large-p t jet production in hadronic collisions*, Il Nuovo Cimento A **70** (1982), no. 3 215.

[37] J. R. Gaunt, C.-H. Kom, A. Kulesza, and W. Stirling, *Same-sign W pair production as a probe of double-parton scattering at the LHC*, The European Physical Journal C **69** (2010), no. 1-2 53.

[38] M. Rinaldi, S. Scopetta, and V. Vento, *Double parton correlations in constituent quark models*, Phys. Rev. **D87** (2013), no. 11 114021, arXiv:1302.6462.

[39] M. H. Seymour and A. Siódmok, *Constraining MPI models using* σ_{eff} *and recent Tevatron and LHC Underlying Event data*, JHEP **10** (2013) 113, arXiv:1307.5015.

[40] LHCb collaboration, R. Aaij *et al.*, *Observation of double charm production involving open charm in pp collisions at* $\sqrt{s} = 7$ *TeV*, JHEP **06** (2012) 141 Addendum ibid. **03** (2014) 108, arXiv:1205.0975.

[41] M. H. Seymour and A. Siodmok, *Extracting sigma effective from the LHCb double-charm measurement*, arXiv:1308.6749.

[42] P. Hagler, *Hadron structure from lattice quantum chromodynamics*, Phys. Rept. **490** (2010) 49, arXiv:0912.5483.

[43] J. Collins, *Foundations of perturbative QCD*, Cambridge monographs on particle physics, nuclear physics, and cosmology, Cambridge Univ. Press, New York, NY, 2011.

[44] G. Sterman and S. Weinberg, *Jets from quantum chromodynamics*, Phys. Rev. Lett. **39** (1977) 1436.

[45] S. D. Ellis and D. E. Soper, *Successive combination jet algorithm for hadron collisions*, Phys. Rev. **D48** (1993) 3160, arXiv:hep-ph/9305266.

[46] M. Cacciari and G. P. Salam, *Dispelling the* N^3 *myth for the* k_t *jet-finder*, Phys. Lett. **B641** (2006) 57, arXiv:hep-ph/0512210.

[47] F. Aurenhammer, *Voronoi diagrams—a survey of a fundamental geometric data structure*, ACM Comput. Surv. **23** (1991) 345.

[48] M. Cacciari, G. P. Salam, and G. Soyez, *The Anti-k(t) jet clustering algorithm*, JHEP **0804** (2008) 063, arXiv:0802.1189.

[49] G. P. Salam and G. Soyez, *A Practical Seedless Infrared-Safe Cone jet algorithm*, JHEP **0705** (2007) 086, arXiv:0704.0292.

[50] LHCb collaboration, A. A. Alves Jr. *et al.*, *The LHCb detector at the LHC*, JINST **3** (2008) S08005.

[51] LHCb collaboration, R. Aaij *et al.*, *Updated measurements of exclusive J/ψ and $\psi(2S)$ production cross-sections in pp collisions at $\sqrt{s} = 7$ TeV*, J. Phys. **G40** (2014) 055002, arXiv:1401.3288.

[52] LHCb Collaboration, R. Antunes-Nobrega *et al.*, *LHCb trigger system: Technical Design Report*, Technical Design Report LHCb, CERN, Geneva, 2003. revised version number 1 submitted on 2003-09-24 12:12:22.

[53] LHCb collaboration, R. Aaij *et al.*, *Production of J/ψ and Υ mesons in pp collisions at $\sqrt{s} = 8$ TeV*, JHEP **06** (2013) 064, arXiv:1304.6977.

[54] M. Adinolfi *et al.*, *Performance of the LHCb RICH detector at the LHC*, arXiv:1211.6759, submitted to Eur. Phys. J. C.

[55] LHCb collaboration, R. Aaij *et al.*, *Measurement of the cross-section for $Z \to e^+e^-$ production in pp collisions at $\sqrt{s} = 7$ TeV*, JHEP **02** (2013) 106, arXiv:1212.4620.

[56] R. Jacobsson, *Performance of the LHCb Detector During the LHC Proton Runs 2010 - 2012*, .

[57] P. Lebrun, *Interim Summary Report on the Analysis of the 19 September 2008 Incident at the LHC*, CERN EDMS **973073** (2008), CERN EDMS 973073.

[58] M. Ferro-Luzzi, *LHC Operation - as viewed from the Experiments*, .

[59] J. Jimenez *et al.*, *Vacuum and Cryogenics observations for different bunch spacing*, .

[60] J. M. Jowett *et al.*, *Heavy Ions in 2012 and the Programme up to 2022*, .

[61] A. Verweij, *Probability of burn-through of defective 13 kA splices at increased energy levels*, .

[62] LHCb collaboration, *First look at the pPb pilot run*, LHCb-CONF-2012-034.

[63] LHCb collaboration, R. Aaij *et al.*, *Measurement of V^0 production ratios in pp collisions at $\sqrt{s} = 0.9$ and 7 TeV*, JHEP **08** (2011) 034, arXiv:1107.0882.

[64] LHCb collaboration, R. Aaij *et al.*, *Observation of Z production in proton-lead collisions at LHCb*, arXiv:1406.2885, submitted to JHEP.

[65] R. Aaij *et al.*, *The LHCb trigger and its performance*, arXiv:1211.3055, to appear in JINST.

[66] LHCb collaboration, R. Aaij *et al.*, *Measurement of the forward energy flow in pp collisions at $\sqrt{s} = 7$ TeV*, Eur. Phys. J. **C73** (2013) 2421, arXiv:1212.4755.

[67] LHCb collaboration, R. Aaij *et al.*, *Measurement of charged particle multiplicities and densities in pp collisions at $\sqrt{s} = 7$ TeV in the forward region*, Eur. Phys. J. **C74** (2014) 2888, arXiv:1402.4430.

[68] LHCb collaboration, R. Aaij *et al.*, *Measurement of charged particle multiplicities in pp collisions at $\sqrt{s} = 7$ TeV in the forward region*, Eur. Phys. J. **C72** (2012) 1947, arXiv:1112.4592.

[69] LHCb collaboration, R. Aaij *et al.*, *Inclusive W and Z production in the forward region at $\sqrt{s} = 7$ TeV*, JHEP **06** (2012) 058, arXiv:1204.1620.

[70] LHCb collaboration, *Measurement of the cross section for $Z \to \mu^+\mu^-$ production with $1.0\,fb^{-1}$ of pp collisions at $\sqrt{s} = 7$ TeV*, LHCb-CONF-2013-007.

[71] LHCb collaboration, R. Aaij *et al.*, *Measurement of J/ψ production in pp collisions at $\sqrt{s} = 2.76$ TeV*, JHEP **02** (2013) 041, arXiv:1212.1045.

[72] J. Carvajal, R. Schwemmer, and N. Neufeld, *Optimising the hlt farm at the lhcb experiment*, in *Real Time Conference (RT), 2010 17th IEEE-NPSS*, pp. 1–4, May, 2010. doi: 10.1109/RTC.2010.5750378.

[73] G. Liu, N. Neufeld, and R. Schwemmer, *Off-site computing farm for the lhcb high level trigger*, Nuclear Science, IEEE Transactions on **60** (2013) 3725.

[74] A. L. Kagan, J. F. Kamenik, G. Perez, and S. Stone, *Top LHCb Physics*, Phys. Rev. Lett. **107** (2011) 082003, arXiv:1103.3747.

[75] R. Gauld, *Measuring top quark production asymmetries at LHCb*, Tech. Rep. LHCb-PUB-2013-009. CERN-LHCb-PUB-2013-009, CERN, Geneva, Jun, 2013.

[76] M. Ferro-Luzzi, *Review of 2011 LHC run from the experiments perspective*, .

[77] LHCb collaboration, R. Aaij *et al.*, *Study of forward Z+jet production in pp collisions at* $\sqrt{s} = 7$ *TeV*, JHEP **01** (2014) 033, arXiv:1310.8197.

[78] LHCb collaboration, R. Aaij *et al.*, *Observation of associated production of a Z boson with a D meson in the forward region*, JHEP **04** (2014) 091, arXiv:1401.3245.

[79] LHCb collaboration, R. Aaij *et al.*, *A study of the Z production cross-section in pp collisions at* $\sqrt{s} = 7$ *TeV using tau final states*, JHEP **01** (2013) 111, arXiv:1210.6289.

[80] LHCb collaboration, R. Aaij *et al.*, *Limits on neutral Higgs boson production in the forward region in pp collisions at* $\sqrt{s} = 7$ *TeV*, JHEP **05** (2013) 132, arXiv:1304.2591.

[81] J. Anderson *et al.*, *Measurement of the cross section for* $Z \to \mu^+\mu^-$ *production in pp collisions at* $\sqrt{s} = 7$ *TeV with the 2011 data*, .

[82] A. Bursche, *Forward production of w/z bosons in pp collisions*, , CERN-Poster-2011-206.

[83] C. J. Clopper and E. S. Pearson, *The use of confidence or fiducial limits illustrated in the case of the binomial*, Biometrika **26** (1934), no. 4 pp. 404.

[84] И. С. Градштейн and И. М. Рыжик, *Таблцы интегалов, сумм, рядов и произведений*, .

[85] W. Barter, A. Bursche, and D. Ward, *Study of forward Z+jet production in pp collisions at* $\sqrt{s} = 7$ *TeV*, .

[86] C. H. Kom, A. Kulesza, and W. J. Stirling, *Pair production of* J/ψ *as a probe of double parton scattering at LHCb*, Phys. Rev. Lett. **107** (2011) 082002, arXiv:1105.4186.

[87] S. P. Baranov, A. M. Snigirev, and N. P. Zotov, *Double heavy meson production through double parton scattering in hadronic collisions*, Phys. Lett. **B705** (2011) 116, arXiv:1105.6276.

[88] A. Novoselov, *Double parton scattering as a source of quarkonia pairs in LHCb*, arXiv:1106.2184.

[89] M. Luszczak, R. Maciula, and A. Szczurek, *Production of two* $c\bar{c}$ *pairs in double-parton scattering*, arXiv:1111.3255.

[90] J. M. Campbell, R. K. Ellis, and D. L. Rainwater, *Next-to-leading order QCD predictions for W + 2 jet and Z + 2 jet production at the CERN LHC*, Phys. Rev. **D68** (2003) 094021, arXiv:hep-ph/0308195.

[91] J. M. Campbell, R. K. Ellis, F. Maltoni, and S. Willenbrock, *Associated production of a Z Boson and a single heavy quark jet*, Phys. Rev. **D69** (2004) 074021, arXiv:hep-ph/0312024.

[92] LHCb collaboration, R. Aaij *et al.*, *Prompt charm production in pp collisions at* $\sqrt{s} = 7$ *TeV*, Nucl. Phys. **B871** (2013) 1, arXiv:1302.2864.

[93] A. Martin, W. Stirling, R. Thorne, and G. Watt, *Parton distributions for the LHC*, Eur. Phys. J. **C63** (2009) 189, arXiv:0901.0002.

[94] CDF collaboration, F. Abe *et al.*, *Double parton scattering in* $\bar{p}p$ *collisions at* $\sqrt{s} = 1.8$ TeV, Phys. Rev. **D56** (1997) 3811.

[95] A. Artamonov *et al.*, *Observation of* J/ψ *and open charm, and double open charm production at* $\sqrt{s} = 7$ *TeV*, .

[96] Li, Ye and Petriello, Frank, *Combining QCD and electroweak corrections to dilepton production in the framework of the FEWZ simulation code*, Phys. Rev. D **86** (2012) 094034, arXiv:1208.5967.

[97] W. D. Hulsbergen, *Decay chain fitting with a Kalman filter*, Nucl. Instrum. Meth. **A552** (2005) 566, arXiv:physics/0503191.

[98] The TOTEM Collaboration, G. Antchev *et al.*, *Luminosity-independent measurements of total, elastic and inelastic cross-sections at* $\sqrt{s} = 7$ *TeV*, EPL (Europhysics Letters) **101** (2013), no. 2 21004.

[99] LHCb collaboration, *Measurement of jet production in* $Z^0/\gamma^* \to \mu^+\mu^-$ *events at LHCb in* $\sqrt{s} = 7$ *TeV pp collisions*, LHCb-CONF-2012-016.

[100] T. Skwarnicki, *A study of the radiative cascade transitions between the Upsilon-prime and Upsilon resonances*, PhD thesis, Institute of Nuclear Physics, Krakow, 1986, DESY-F31-86-02.

[101] BaBar collaboration, J.-P. Lees *et al.*, *Branching fraction measurements of the color-suppressed decays* $\bar{\mathrm{B}}^0 \to \mathrm{D}^{(*)0}\pi^0$, $\mathrm{D}^{(*)0}\eta$, $\mathrm{D}^{(*)0}\omega$, *and* $\mathrm{D}^{(*)0}\eta'$ *and measurement of the polarization in the decay* $\bar{\mathrm{B}}^0 \to \mathrm{D}^{*0}\omega$, Phys. Rev. **D84** (2011) 112007, `arXiv:1107.5751`.

[102] P. M. Nadolsky *et al.*, *Implications of CTEQ global analysis for collider observables*, Phys. Rev. **D78** (2008) 013004, `arXiv:0802.0007`.

[103] I. S. Gradshteyn and I. M. Ryzhik, *Table of Integrals, Series, and Products, Fifth Edition*, Academic Press, 4th ed., 1965.